Summer 2018

Magnetic field effect and other spectroscopies of organic semiconductor and hybrid organic-inorganic perovskite devices

Kevser Sahin Tiras
University of Iowa

MAGNETIC FIELD EFFECT AND OTHER SPECTROSCOPIES OF ORGANIC SEMICONDUCTOR AND HYBRID ORGANIC-INORGANIC PEROVSKITE DEVICES

by

Kevser Sahin Tiras

A thesis submitted in partial fulfillment of the
requirements for the Doctor of Philosophy
degree in Physics
in the Graduate College of
The University of Iowa

August 2018

Thesis Supervisor: Professor Markus Wohlgenannt

Graduate College
The University of Iowa
Iowa City, Iowa

CERTIFICATE OF APPROVAL

PH.D. THESIS

This is to certify that the Ph.D. thesis of

Kevser Sahin Tiras

has been approved by the Examining Committee for the thesis requirement for the Doctor of Philosophy degree in Physics at the August 2018 graduation.

Thesis committee: _____
Markus Wohlgenannt, Thesis Supervisor

_____
Robert L. Merlino

_____
David Andersen

_____
Fatima Toor

_____
James Rybicki

To my family, Osman Kerem, Yusuf Erdem, Meryem Sena and Emrah.....

ACKNOWLEDGEMENTS

First and foremost, I would like to express my deepest gratitude to my advisor, Prof. Markus Wohlgenannt for his guidance, encouragement, and advice he has provided throughout my Ph.D. years. Without his support, this thesis could not have been completed.

I would like to thank Asst. Prof. James Rybicki from the University of Wisconsin, Eau Claire, who has served on my dissertation committee. His advice and help throughout my Ph.D. years have been invaluable.

I also would like to thank the other thesis committee members, Prof. Robert L. Merlino, Prof. David Andersen and Asst. Prof. Fatima Toor from the University of Iowa (UI).

Further, I would like to thank my present and former lab colleagues Dr. Fujian Wang, Dr. Ran Lin, and Yifei Wang for their contributions and suggestions to my research work.

In addition, I thank all the professors, and administrative and technical staff of the Department of Physics and Astronomy at UI for their kindness and support.

Finally, I would like to express my deepest love and gratitude to my parents and my husband Emrah for their endless support and encouragement. I also thank my wonderful children Osman Kerem, Yusuf Erdem and Meryem Sena for always making me smile and unending inspiration.

ABSTRACT

This thesis consists of three main studies: magnetic field effects in thermally activated delayed fluorescent (TADF) organic light emitting diodes (OLEDs), magnetic field effects in bipolar and unipolar polythiophene (P3HT) devices and a study of hybrid organic-inorganic perovskite devices.

Spin-dependent transport and recombination processes of spin-pair species have been detected by magnetic field effect (MFE) technique in carbon-based semiconductor devices. Magneto-electroluminescence (MEL) and magneto-conductivity have been measured as a function of the applied magnetic field, B, in light emitting diodes. TADF materials have been used instead of simple fluorescent materials in OLEDs. We have observed very large magnetic response with TADF materials.

The second study is magnetic field effects of regio-regular P3HT based OLED devices. P3HT is a well known semiconducting polymer, and its electrical properties such as magneto-conductance can be affected by an applied magnetic field. P3HT was chosen because it exhibits a sign change in magnetoresistance (MR) as the bias is increased. Unipolar and bipolar devices have been fabricated with different electrode materials to understand which model can be best to explain organic magnetoresistance effect, possibly depending on the operating regime of the device. Transport and luminescence spectroscopies were studied to isolate the different mechanisms and identify their fingerprints.

The third study is on hybrid organic-inorganic perovskite devices. With the

potential of achieving very high efficiencies and the very low production costs, perovskite solar cells have become commercially attractive. Scanning electron microscopy (SEM) images and absorption spectrum of the films were compared in single-step solution, two-step solution and solution-assisted vapor deposition techniques. Grain size, morphology and thickness parameters of perovskite films were studied within these techniques. Perovskite solar cells were fabricated and their efficiencies were measured.

PUBLIC ABSTRACT

This dissertation consists of experimental studies of organic light emitting diodes (OLEDs) and hybrid organic-inorganic solar cells. Light emitting diodes (LEDs) have been used in the generation and control of light both for general lighting and electronic displays. An electron's energy is converted into light by plastic LEDs used in most electronic displays, but the magnetic character of the electron prevents some electrons from efficiently producing light. In the first part of the thesis, we have showed that a small magnetic field will manipulate the magnetic character of the electron in special blends of plastic, generating light more efficiently and providing a new way to integrate magnetic memory and storage with electronic displays.

The second part of the thesis concentrates on how a magnetic field alters the electrical conduction in plastic semiconductors. There are well-known models to explain the change in the conductance, called magnetoresistance effect. Different device structures with different electrode materials were studied to understand the detailed scientific mechanism behind the effect.

Generating electrical power from other forms of energy has been accomplished by several different ways. Solar cells, the conversion of solar radiation into electrical current, is particularly promising. Perovskite solar cells have gained great attention because of their high efficiencies and low production costs. Here, we have fabricated perovskite solar cells by using different deposition techniques and measured their efficiencies.

TABLE OF CONTENTS

LIST OF TABLES

Table

LIST OF FIGURES

CHAPTER 1
INTRODUCTION

1.1 π-conjugated Organic Semiconductors

A conjugated system consists of alternating single and double carbon-carbon bonds. There are two groups of π-conjugated organic semiconductors depending on their molecular weight: polymers and small molecules. Polymers have a molecular weight that is higher than 1000 g/mol, thus it is easy to dissolve and deposit them. On the other hand, small molecules have smaller molecular weight ($<$ 1000 g/mol) and thermal evaporation is used in order to deposit them. When two carbon atoms are bonded in a conjugated system, three electrons (for each carbon atom) form planar σ-bonds with the neighboring carbon and hydrogen atoms (this electronic configuration is called sp^2), and one electron (for each carbon atom) builds a π-bond, as shown in Figure 1.1.

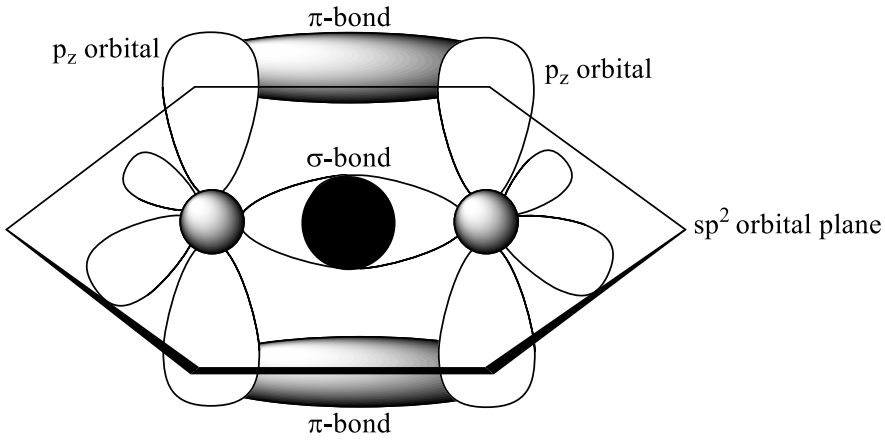

Figure 1.1: Schematic diagram of sp^2 and p_z orbitals for two carbon atoms.

The π-bond is perpendicular to the sp^2 orbital plane. Delocalization of π-electrons over the entire molecular chain results in semiconducting electronic behavior [1]. More specifically, the unhybridized p_z orbitals overlap and form filled bonding π-orbitals and unoccupied anti-bonding π^*-orbitals. The bonding orbital highest in energy is called the highest occupied molecular orbital (HOMO), and the anti-bonding orbital lowest in energy is called the lowest unoccupied molecular orbital (LUMO). The energy gap between HOMO and LUMO is generally in the range 1.5-3eV for organic semiconductors, which makes them ideal for applications in optoelectronics, because this is roughly the range of energy for visible photons.

1.2 Excitations in Organic Semiconductors

We now describe excited states in organic semiconductors that are important to understanding their optoelectronic properties. Polarons (charged) and excitons (neutral) are the primary excitations that are dominant in organic semiconductor materials. Neutral spinless excitations are photogenerated upon photoexcitation, whereas charged excitations result from charge injected from electrodes upon electrical excitation. Singlet excitons (SE), which are neutral spinless excitations may either relax into charged excitations or other neutral excitations (i.e. triplet excitations), although the quantum efficiencies for these processes are usually not very high, most SE relax directly back to the groundstate either by photoluminescence or heat emission. The fraction of SE that result in photoluminescence is called the (internal) photoluminescence quantum efficiency.

1.2.1 Polarons and Bipolarons

The intermolecular Van der Walls forces in organic solids are much weaker than ionic and covalent bonds of inorganic materials, and consequently the organic materials are soft. In other words, the lattice is more rigid in an inorganic material than an organic material, therefore adding a charge onto a site does not substantially affect the surroundings in inorganic materials. However, as a charge carrier propagates in an organic material it will carry with it a distortion of the charge's surroundings, and a polaron is formed. A polaron is either negatively or positively charged, and possesses spin 1/2. It has two symmetrical, localized states in the energy gap. In a polaron, P_1 and P_2 are two allowed below-gap optical transitions as shown in Figure 1.2. Polarons are the carriers of electrical current in organic solids. They move from site to site by hopping. In organic solids, therefore, the charge carrier mobilities are many orders of magnitudes lower than in an inorganic crystal, where band transport is often dominant.

A Coulombically bound pair of negative and positive polarons residing on neighboring molecules forms a polaron pair (PP) as shown in Figure 1.3. PPs are the intermediate step between an exciton and free polarons and importantly factor in the device efficiency of organic light-emitting diodes (OLEDs) and photovoltaic (OPV) devices. Depending on the spin arrangement of the two polaron spins, PPs may either occur as spin-0 singlets or spin-1 triplets.

A bipolaron is formed by two polarons with equal charge and opposite spins (i.e. total spin-0) on the same site, and its energy may be lower than that of two

individual polarons because of electron-phonon interactions. This electron-phonon interaction can be understood as one polaron constituting the bipolaron taking advantage of the distortion field already created by its partner. Often, however, this is offset by their Coloumb repulsion. A bipolaron has two in-gap electronic states with only one allowed optical transition, and it can either be doubly positive (BP^{++}) or doubly negative (BP^{--}) [2].

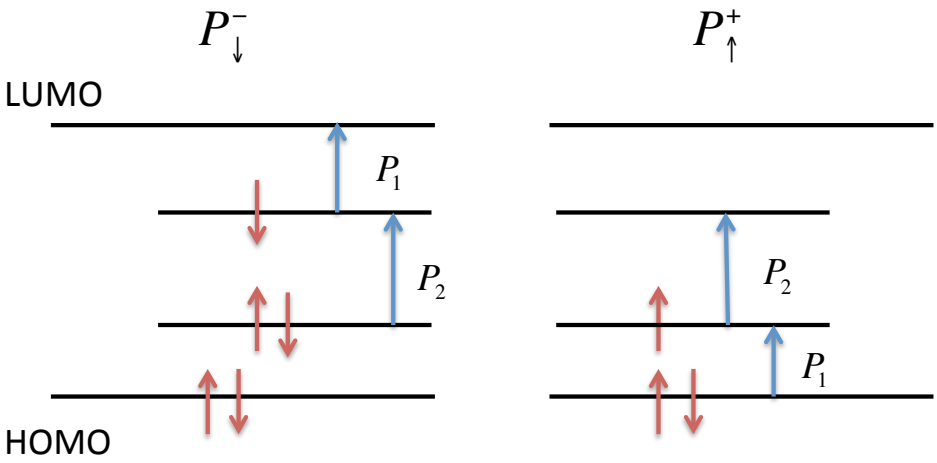

Figure 1.2: Two allowed below-gap optical transitions in a negative (left) and a positive (right) polaron.

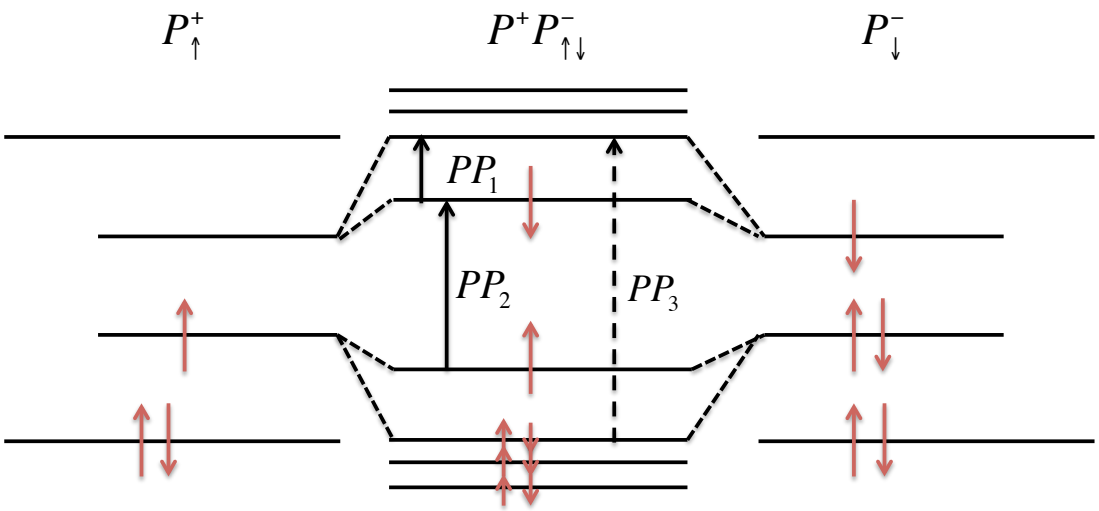

Figure 1.3: Possible optical transitions in polaron-pairs.

1.2.2 Excitons and Exciplexes

An electron can be excited from the HOMO to the LUMO in a π-conjugated semiconductor by the absorption of a photon, and this forms a Coulombically-bond state, known as excitons. Their binding energy is substantial, usually about 0.5 eV. A photo-generated exciton may recombine radiatively by light emission in the form of photoluminescence (PL) or nonradiatively by emitting phonons (heat). It may also convert into a long-lived triplet exciton via intersystem crossing, or separate into a polaron pair. Singlet excitons have zero net spin vectors, whereas triplet excitons have nonzero net spin vector (spin-1). According to quantum mechanics, only one spin-state is formed for the singlet exciton and three different spin-projection states for the triplet exciton. The lifetime for radiative recombination of excited singlet states is in the range of nanoseconds in organic semiconductors. Within that time singlet excitons

can diffuse through the organic film, and the diffusion length of singlet excitons is around 10 nm. Optical transitions from a triplet state to the (singlet) ground state is spin-"forbidden" (strongly suppressed) because of spin-conservation, however a slow radiative transition, called phosphorescence (PH), may be possible if a spin flip of one of the electrons occurs due to spin-orbit coupling. Triplets have a long lifetime of the order of milliseconds [3]. The probability of this spin-flip may be strongly enhanced in organic compounds that contain heavy elements (typically Iridium or Platinum), as the spin-orbit coupling strength scales roughly with the fourth power of the atomic weight ("heavy atom effect").

An exciplex is basically an exciton located at the interface of two organic materials, a "guest" and a "host" material, also called electron acceptors and donors. The exciplex experiences a different environment compared to excitons because of the acceptor-donor interface, and their Coulomb binding energy is usually much smaller than for excitons, and the exchange splitting between singlet and tiplet states can be as small as the thermal energy at room temperature. The Photoluminescence is red shifted compared to excitonic emission. Exciplex-based OLEDs have recently risen to prominence, as they may show larger efficiency compared to single component excitonic OLEDs. This is so because of the small energy difference, triplets can be upconverted to emissive singlets requiring only the thermal energy available at room temperature. This process is called thermally activated delayed fluorescence, and we will have much more to say about it later on.

1.3 Organic Light Emitting Diodes (OLEDs)

Organic semiconductor devices have been widely used in organic light emitting diodes (OLEDs) for lighting and display applications because of their flexibility, low-cost fabrication, and efficient light output. A general structure of an OLED consists of an active layer of an organic compound in the form of a thin film ($\approx$ 100 nm) with metallic electrodes at the top and bottom surface, as shown in Figure 1.4. Organic semiconductors often have a relatively poor carrier mobility, typically orders of magnitudes less than 1 cm^2/Vs. Therefore, in order to have a reasonably conductive active layer, its thickness has to be thin enough to transport the charge carrier through the layer. A typical thickness is approximately is 0.1μm. At the same time, a relatively large voltage on the order of volts is applied across the thin film, resulting in large electric fields (up to 10^6 V/m). In this way, in spite of the low carrier mobility, significant currents can be achieved. OLEDs often use intrinsic/undoped organic semiconductors which have almost no intrinsic carrier density and conductivity. However, when a voltage is applied, electrons and holes are injected from the anode and cathode, respectively, by overcoming the injection energy barriers at the electrodes. These barriers can be made small enough by choosing cathode materials that have a low work function, and anodes with a large workfunction. Ca and Au, respectively, fit that bill. In an OLED, light has to be able to leave the device, therefore one of the two electrodes must be transparent. Therefore Indium-Tin-Oxide (ITO) is used instead of a noble metal anode. The injected charges travel through the film to the opposite electrode. When they meet oppositely charged carriers coming

from the other electrode, the two charges first form a loosely-bound polaron-pair and finally a tightly bound exciton. As we already mentioned above, because both the electron and the hole carry spin 1/2, excitons can occur as spin singlets (total spin 0) or triplets (total spin 1). Emission of photons occurs as singlet excitons return to the ground state, and this is called electroluminescence or electrofluorescence. The fraction of injected polarons that result in electroluminescence is called the (internal) electroluminescence quantum efficiency. Electrophosphoresence is also possible, if heavy-atom-containing organic compounds are used.

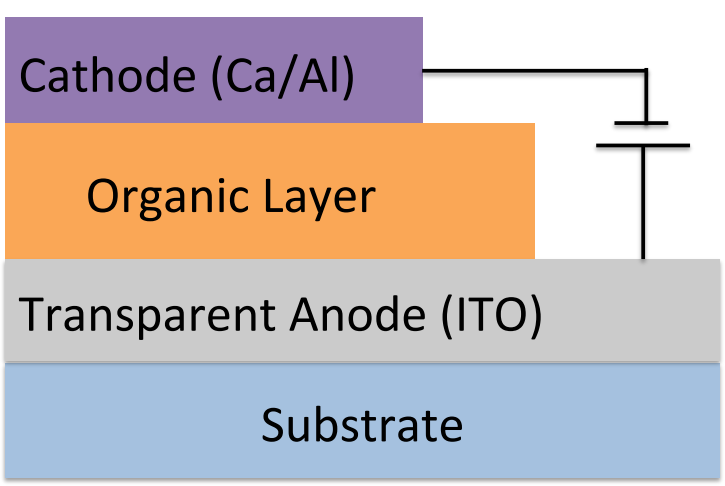

Figure 1.4: OLED structure.

Based on spin degeneracy, the ratio between singlet and triplet excitons formed is 1:3 (see Figure 1.5). The internal electroluminescence quantum efficiency (IQE) of fluorescent-based OLEDs is limited to 25% because only singlet excitons contribute to electroluminescence [4]. Recently, thermally activated delayed fluorescent materials

have been used in OLEDs to overcome this limitation [5,6]. These are based on two-component exciplex systems where the exchange energy difference between singlet and triplet exciplexes can be as low as the thermal energy, and intersystem crossing readily occurs.

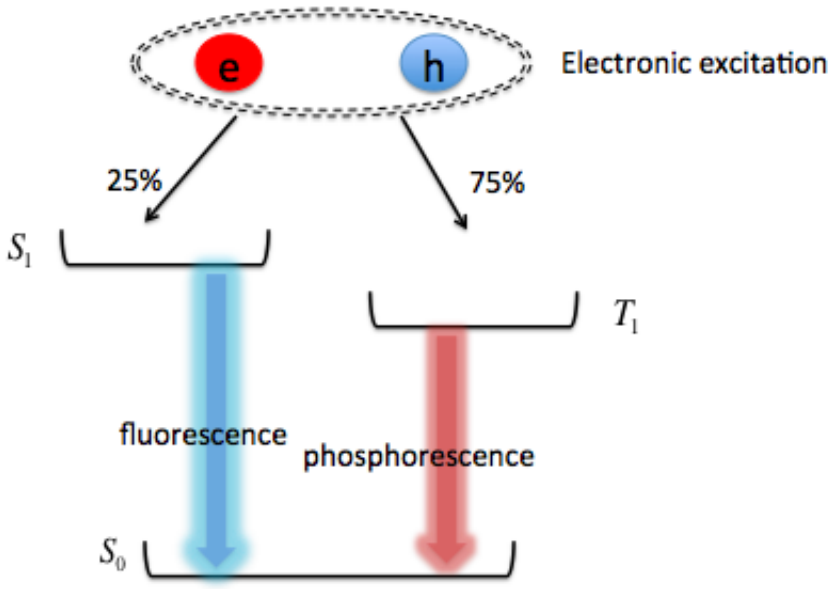

Figure 1.5: Exciton production under electrical excitation.

1.4 Organic Magnetoresistance (OMAR)

A device which consists of two ferromagnetic electrodes separated by a non-magnetic spacer layer is called spin-valve in the field of spintronics. Spintronics deals with utilizing the electron's spin degree of freedom. When a magnetic field is applied to the electrodes, they can switch between parallel and antiparallel magnetization configuration. The resistance changes as the configuration switches between

the two configurations. The difference in resistance is called Giant Magnetoresistance (GMR) [7,8]. GMR typically has a metallic spacer layer, and the spin-polarized current passes through this layer. If the spacer layer is a thin layer of an insulator, the Tunneling Magnetoresistance (TMR) effect occurs [9–11]. In TMR devices, the spin-polarized current tunnels through the spacer layer. Beginning in 2004, it has been found that organic semiconductors layers can be used to construct GMR and TMR devices. In particular, the small molecule Tris-(8-hydroxyquinoline) aluminum (Alq_3) was used in organic spin-valve devices [12] and in electroluminescence enhancement studies in OLEDs [13]. In 2004, a novel magnetoresistance effect was discovered in polyfluorene sandwich devices with nonmagnetic electrodes at room temperature and relatively small applied magnetic fields (some mT) [14]. Since these devices contain no ferromagnetic spin-polarizing layers, the physical mechanism behind this organic magnetoresistive (OMAR) effect is entirely different from that of spin-valves. It is believed that the hyperfine field of hydrogen atom plays an important role in various magnetic field effects on conductivity, electroluminescence and photoconductivity that have been reported by many groups. However, the exact underlying mechanism behind OMAR is still debated, and various theories have been proposed.

1.5 Possible Mechanisms for OMAR

1.5.1 Hyperfine Field Interaction-Based Mechanisms

Magnetic field effects have been seen in both current and electroluminescence (EL) measurements. This gives us a clue that they might share a similar origin.

Since EL depends on the population of the singlet and triplet excitons, the origin of OMAR is related to interactions and transitions between different spin states. OMAR is observed in organic semiconductors that have hydrogen atoms in their molecular structure [15]. This suggests that hyperfine interaction causes the OMAR effect. The hyperfine field mechanism is a major source of spin dynamics in organic spintronics, and the effective hyperfine field strength is on the order of mT [16,17]. The hyperfine field is due to the magnetic moment of the hydrogen nuclei (Figure 1.6). The paramagnetic (electronic) spin of the polarons making up a paramagnetic pair will precess about this hyperfine field. The hyperfine field direction varies from site to site and therefore causes spin-mixing in paramagnetic pairs on neighboring molecules. The spin-mixing is suppressed if an applied magnetic field exceeds the hyperfine strength. This changes the reaction rate between the paramagnetic entities. We will now discuss more specific models involving certain paramagnetic entities. There are three different models based on spin-dynamics induced by hyperfine interaction: the bipolaron mechanism, the electron-hole pair (EHP) model and the triplet-exciton polaron quenching (TEQ) model. It is interesting to study the sign changes of magnetoconductance (MC) for each model since the applied magnetic field can either increase the current (positive magnetoconductance, +MC) or decrease the current (negative magnetoconductance, -MC).

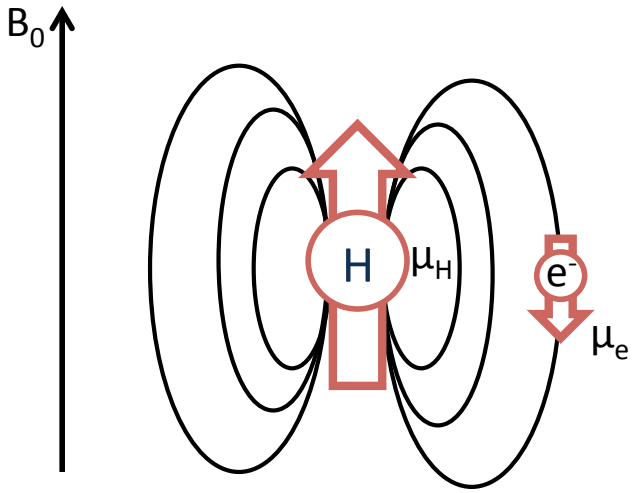

Figure 1.6: A single electron system the electron with its own magnetic moment moves within the magnetic dipole field of the nucleus in the presence of an applied magnetic field, B_0.

1.5.1.1 Bipolaron Mechanism

The bipolaron mechanism relies on MFE on bipolaron formation [18] (which occurs between equal charges). In the absence of an applied magnetic field (Figure 1.7 a) the polarons' spins precess around the local (hyperfine) magnetic field. This local field is randomly oriented from site to site. When an external magnetic field is applied, the net local fields become more and more aligned (Figure 1.7 b). With greater applied magnetic field, polarons' spins precess along similar orientations. This makes the bipolaron formation and hopping more unlikely. This is because bipolarons are only formed in singlet states, and the applied magnetic field suppresses hyperfine induced triplet to singlet transitions. The bipolaron model can have both +MC and -MC in the presence of hyperfine fields and an externally applied magnetic field. However, in the simplest case of the bipolaron model the MC is expected to be negative and due to spin-blocking [18]. In short, spin-blocking occurs because the Pauli exclusion principle forbids the occupation (of a single orbital) of a molecule with two parallel spins. This constitutes a restriction on the conduction paths, and increases the resistance of the device. Hyperfine-induced spin-dynamics may remove this restriction, whereas an applied magnetic field will reinforce this restriction.

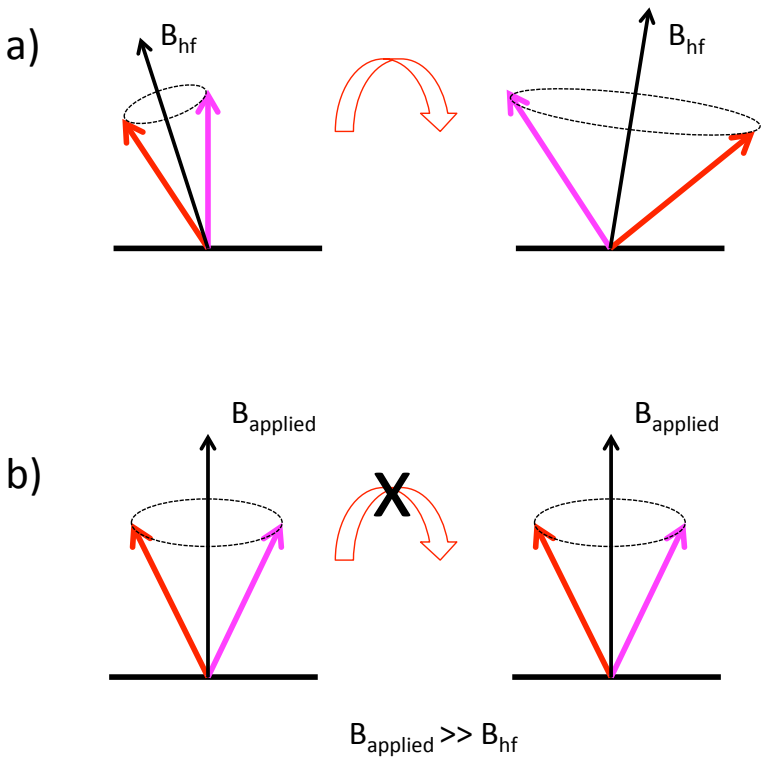

Figure 1.7: a) Precession of a polaron's spin about randomly oriented hyperfine fields (B_{hf}), allowing for bipolaron formation. b) Application of a large external magnetic field aligns the local fields, leading to spin blocking of a triplet pair.

1.5.1.2 Electron-Hole Pair Model

In EHP model (Figure 1.8), the OMAR effect is explained based on spin-dependent exciton formation, where the exciton is formed by the recombination of oppositely charged polarons (i.e. electrons and holes) [19–23]. The basic premise of the EHP model is that singlet excitons form from singlet polaron pairs with a rate k_S that is different from the rate k_T with which triplet excitons form from triplet polaron pairs. The difference between k_S and k_T is presumably caused by the large exchange energy difference (on the order of 1 eV) in excitons [24].

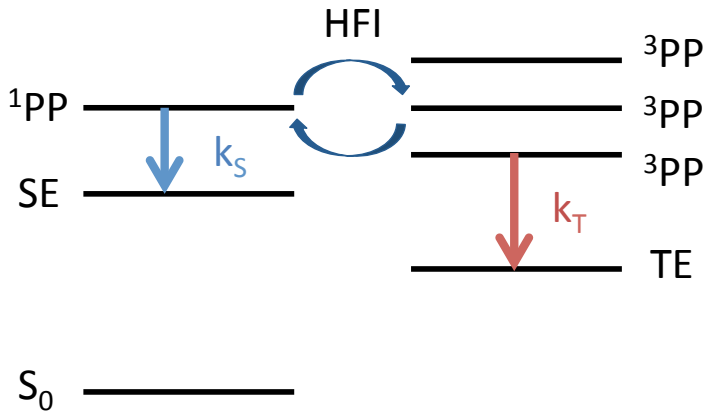

Figure 1.8: Energy levels for polaron pairs and excitons. The hyperfine field (HF) mixes triplet and singlet polaron pairs with each other. Singlet polaron pairs (^1PP) form singlet excitons (SE) with a rate k_S whereas triplet polaron pairs (^3PP) form triplet excitons (TE) with a rate k_T. The ground state S_0 is also shown.

1.5.1.3 Triplet-Exciton Polaron Quenching Model

The TPQ model is based on spin-dependent reactions between a triplet exciton and a polaron [25]. EHP and TPQ models rely on magnetic field effects (MFE) on excitons (and require both positive and negative charges to be present). The triplet exciton density via the intersystem crossing process can be affected by an applied magnetic field. Therefore, this changes density [26] and mobility [25] of the mobile polarons. Desai et al. showed that a competition between +MC (triplet-exciton quenching) and -MC (triplet-exciton dissociation) causes a sign change in the OMAR effect [25].

1.5.2 Δg Mechanism

Another mechanism to explain the OMAR effect is the Δg mechanism which has recently been purposed in organic and hybrid perovskite systems [27–29]. Different proportionalities of the spin precession to the magnetic field (Landé g factor) on neighboring molecules leads to a varying spin-precession frequency in paramagnetic pairs, and therefore to spin-mixing (Figure 1.9). Because of material dependent interactions i.e. spin-orbit coupling, the g factor differs from the free electron value, and the Δg-mechanism is expected to be significant primarily in mixed component films.

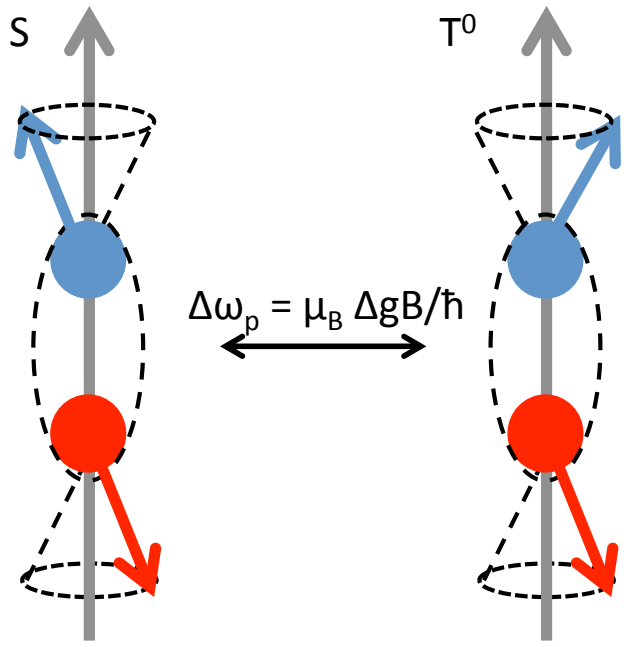

Figure 1.9: Δg spin-mixing mechanism within an electron-hole spin-pair that shows the intersystem crossing between the spin singlet, S, and triplet, T_0, Electron and hole have different precession frequencies around a finite applied field, B in the z direction.

Independent of the detailed mechanism, OMAR traces were found to obey empirical laws given by either the non-Lorentzian line shape $\Delta I(B)/I \propto B^2/(|B| + B_0)^2$ or a Lorentzian $\Delta I(B)/I \propto B^2/(|B|^2 + B_0^2)$, where B_0 determines the width of the lineshape, and is generally of a magnitude similar to the hyperfine scale, i.e. several mTs [30]. $I(B)$ is the device current measured for an applied magnetic field B, whereas $I(0)$ is the corresponding value for zero applied field. Similar quantities can also be formed for other device parameters that can vary with an applied magnetic field, e.g. the electroluminescence output.

CHAPTER 2
MAGNETIC FIELD EFFECTS IN EXCIPLEX LIGHT EMITTING DIODES DUE TO CORRELATED SPIN-CHARGE DYNAMICS

OLEDs have been used in lighting and flat panel displays due to their desirable properties such as flexibility, efficient light emission and low operating temperatures. To avoid the limitation on the internal electroluminescence quantum efficiency, η due to the singlet-triplet spin-considerations we described above, phosphorescent-based OLEDs have been studied for several years now [31]. Phosphorescence in organic compounds requires the incorporation of heavy metals, typically Pt or Ir, and this makes these materials quite expensive [5]. Therefore alternative ways to improve η are being sought. Recently, a value of nearly 100% for η has been obtained by using thermally activated delayed fluorescent (TADF) materials in OLEDs [5, 6, 32]. Δ_{ST}, the exchange splitting between the singlet and triplet states, in excitons is much larger than the thermal energy (25 meV at room temperature). In TADF, intermolecular excitations or exciplexes are the emitting species. Because of the larger electron-hole separation in exciplexes compared to excitons, Δ_{ST} can be comparable to the thermal energy, and non-emissive triplets can get upconverted to emissive singlet exciplexes. Another approach to increase the EL efficiency is to use magnetic field sensitive spin effects on EL in organic semiconductors [16, 19, 27, 33–38]. However, until now, these MFE-enhancement of the EL are relatively small. Our idea now is that these MFE should be much larger in TADF materials, as, because of the small Δ_{ST} in TADF blends, the spin dynamics of recombination could be changed

by a small magnetic field. This can improve the OLED efficiency and result in very large OMAR effects. Our study used well-known TADF materials that have a large internal quantum efficiency. Immense resistance and electroluminesecence responses were obtained in the organic blend. Temperature dependence, efficiency improvement, magneto-conductance and -luminescence versus applied magnetic field will be presented. To compare magnetic field effects in previously known excitonic devices to our exciplex devices, polymer-based, MEH-PPV (a typical excitonic material) and TADF-based OLEDs have been studied. In the excitonic system, spin mixing may occur via the hyperfine field or the Δg mechanisms. This spin-mixing causes transitions between singlet and triplet polaron pairs, which are the precursors to exciton formation. After formation of excitons, further spin mixing is forbidden because of the large Δ_{ST}. The singlet exciton formation rate is different from the triplet exciton formation rate, i.e. $k_S \neq k_T$, but both the formation of singlet excitons from singlets polaron pairs as well as the formation of triplet excitons from triplet polaron pairs are spin-allowed exothermic reactions. In contrast, Δ_{ST} is of the order of the thermal energy in TADF exciplex materials. Therefore, transitions from singlet to triplet state exciplexes (not just their precursor states) occur upon thermal activation. Singlet exciplexes decay radiatively directly to the singlet ground state, whereas triplet exciplexes cannot unless a spin-flip occurs. Therefore the singlet channel is spin-allowed, whereas the triplet channel is now spin-"forbidden". Therefore $k_S \gg k_T$, and this can give rise to very large MFEs.

2.1 Device Composition and Fabrication

The device structure consists of TADF materials deposited in several layers sandwiched between anode (indium-tin-oxide (ITO)) and cathode (Ca/Al) electrodes, and it is shown in Figure 2.2 a). We use well-known TADF materials that have large internal quantum efficiency [5]: 4,4,4-tris[3-methylphenyl(phenyl)amino] triphenylamine (m-MTDATA) as the donor and tris-[3-(3-pyridyl)mesityl]borane (3TPYMB) as acceptor. The chemical structures of 3TPYMB and m-MTDATA with LUMO and HOMO levels are shown in Figure 2.1. m-MTDATA (> 99% pure) was purchased from Sigma-Aldrich and two batches with different purities of 3TPYMB (> 99.2% pure, used for data in Figure 2.8 and 2.10 and > 99.8% pure, used in all other figures) were purchased from Lumtec (Luminescence Technology Corp.). ITO/glass substrates were carefully cleaned in solvents and plasma treated, and thermal evaporation was used for the deposition of the organic layers under high vacuum at 10^{-7} mbar. The structure of the devices was ITO/m-MTDATA (15 nm)/25 wt%-m-MTDATA: 3TPYMB (180nm)/3TPYMB (15 nm)/Ca (30 nm)/Al (60 nm). During the co-evaporation of the 25 wt%-m-MTDATA:3TPYMB, m-MTDATA was deposited at a rate of 0.1 nm/s and 3TPYMB at 0.3 nm/s. A cathode layer consisting of calcium covered by a layer of aluminum to avoid oxidization was deposited by thermal evaporation in most devices, but e-beam evaporation was used for some devices. The active device area was about $1mm^2$. The spectrum of the electroluminescence in our devices (Fig. 2.2b) shows that exciplexes are responsible for EL in our device, since its emission spectrum is entirely different from the emission from excitons (also shown in the figure) [5].

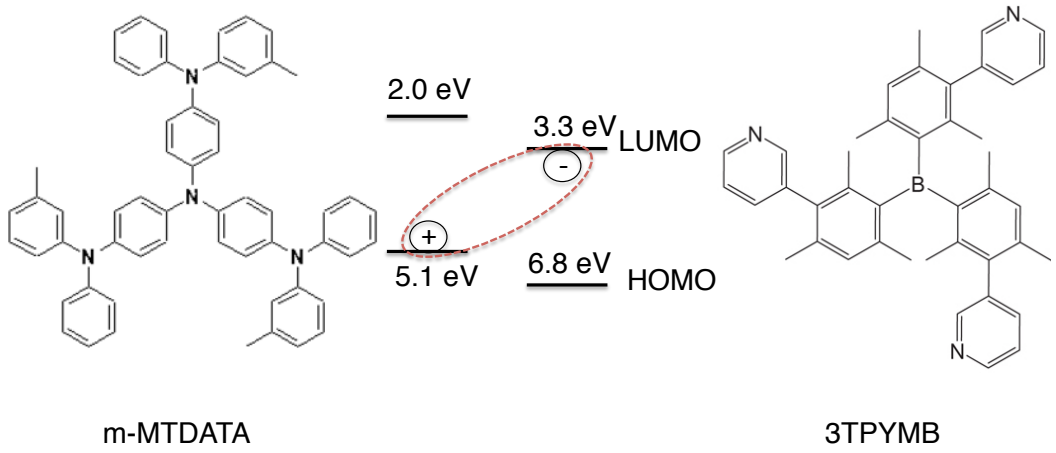

Figure 2.1: Chemical structures for both m-MTDATA as the donor and 3TPYMB as the acceptor, and exciplex residing at interface between HOMO of donor and LUMO of acceptor.

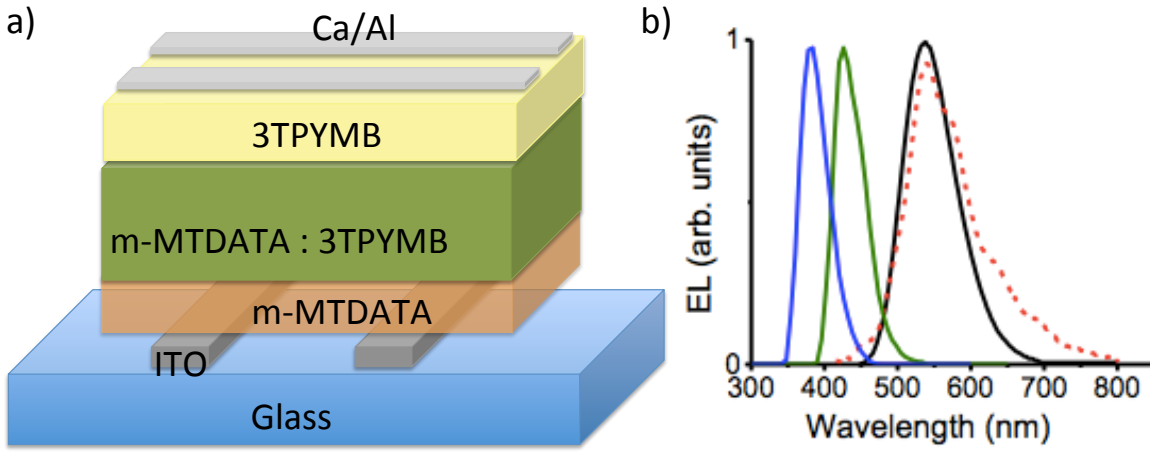

Figure 2.2: a) Exciplex device structure. b) Electroluminescence spectrum for our device (red dashed line), compared with exciplex emission (solid black line) and exciton emission spectra taken from the literature (solid blue and green lines) [5].

2.2 Magnetic Field Effect Measurements

The devices were mounted in a closed-cycle He cryostat placed between two poles of an electromagnet for the measurement of the magnetic field effects. Experimental setup for magnetoresistance measurement is shown in Figure 2.3. All reported data are for room-temperature, unless otherwise stated. The devices were driven at either a constant voltage V or a constant current I using a Keithley 2400 Source Meter. The particular current and voltage bias levels were chosen in pairs such that they corresponded to similar driving conditions. The electroluminescence intensity was measured using a photomultiplier tube which was shielded from the magnetic field during sweeps. Figure 2.4 shows the experimental setup for magnetoelectroluminescence measurements. The MFE can be detected either by measuring I as a function of B, or, alternatively by measuring the electroluminescence (EL) as a function of B. These two measurements are performed simultaneously when either the applied device voltage is kept constant (measuring a change $\Delta I(B)$ and $\Delta EL(B)$), or when the device current is kept constant (measuring a change in applied voltage $\Delta V(B)$ and $\Delta EL(B)$). The MFE, $\Delta x/x$, in all these quantities is defined as $[x(B) - x(0)]/x(0)$.

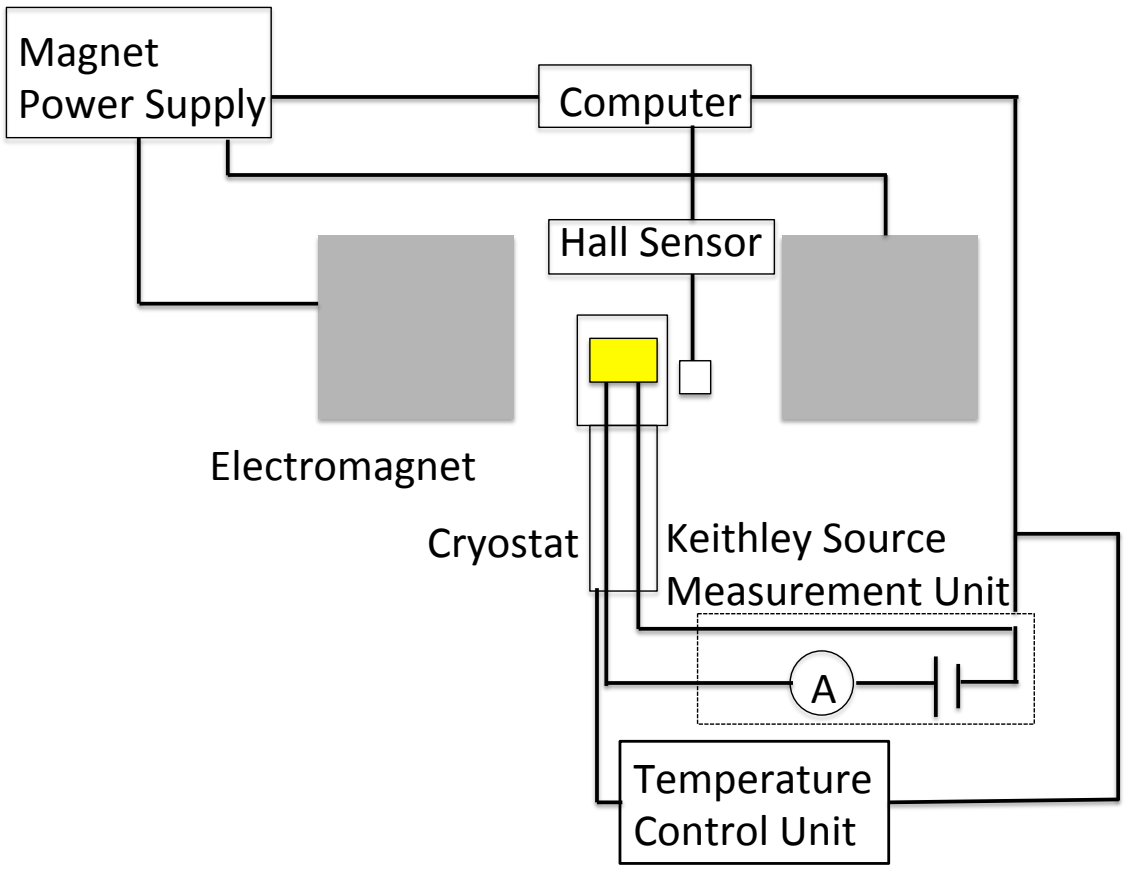

Figure 2.3: Experimental set-up for magnetoresistance measurement.

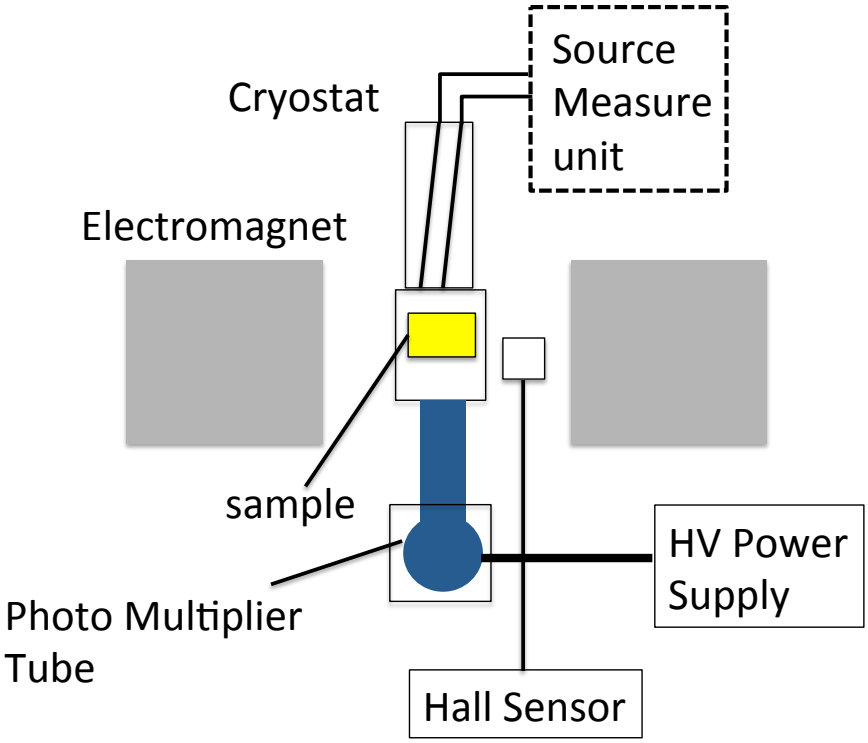

Figure 2.4: Experimental set-up for magnetoelectroluminescence measurement.

2.2.1 Conductivity and Electroluminescence Measurements at Constant Current and Constant Voltage

Figure 2.5 shows measurements of MFE in our devices for both constant voltage and constant current measurements. Figure 2.5a) and b) shows that these devices exhibit magnetoconductance (MC) and magnetoelectroluminescence (MEL) effects of up to 30% and 60%, respectively, for constant voltage measurements, whereas the effects for constant current measurements are smaller. The data in Fig. 2.5 is well-fit by the non-Lorentzian expression. The sign of the effect allows us to make a conclusion regarding the source of the spin-dynamics that underlies the observed MFE. In

our regime for exciplexes, i.e. $k_S \gg k_T$, the hyperfine mechanism predicts an MEL $\sim -50\%$, however we report a positive 60% MEL for our exciplex devices. This is consistent with the Δg-mechanism: the larger the applied magnetic field, the larger will be the difference between precession frequencies and the more pronounced is the MFE. At the same time we expect a significant Δg between electron and hole, because they reside on different molecules in our two-component blend TADF devices.

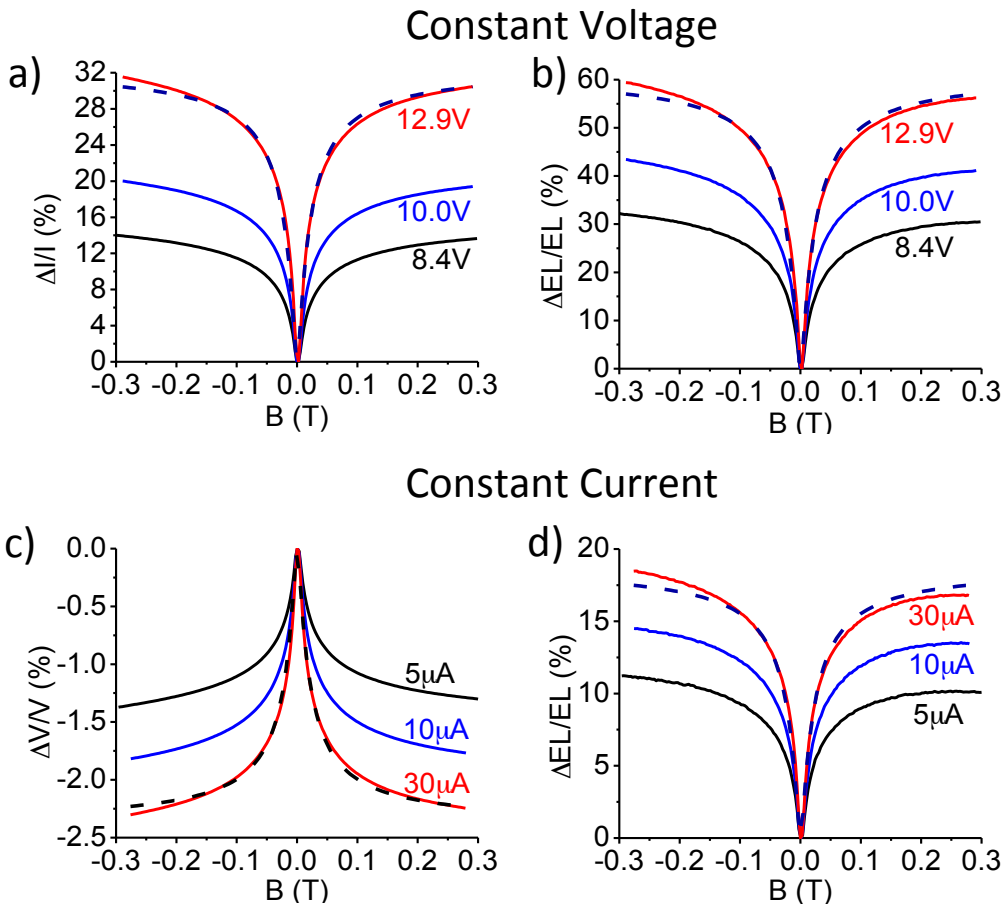

Figure 2.5: a) Magnetoconductance (MC) and b) magnetoelectroluminescence (MEL) for three representative constant voltages. c) Magnetovoltage and d) magnetoelectroluminescence for three representative constant currents. The same color is used throughout the figure to designate measurements with a comparable current-density. Thick dashed lines are non-Lorentzian (as defined in text) fits to the largest displayed curve in each panel.

Δg-mechanism arises in situations where there are large magnetic field gradients present, leading to variation of the precession frequency. This difference in precession frequency is due to different proportionalities of the spin precession to the magnetic field on neighboring molecules, as shown in Figure 2.6. As a result of material-dependent interactions including spin-orbit coupling, the g factor differs

from the free-electron value.

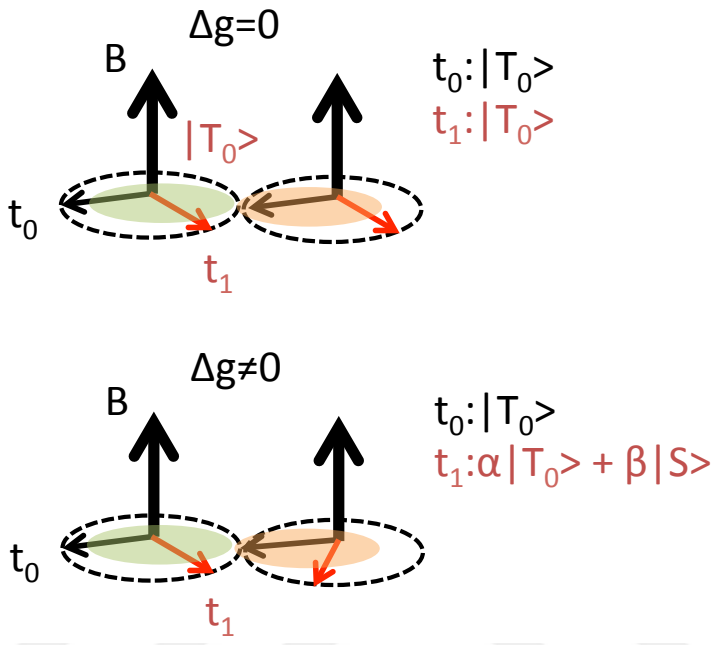

Figure 2.6: Δg spin mixing between the electron and hole spins which are initiated at time t_0 in the $|T_0\rangle$ spin configuration. The electron (hole) wave function is schematically represented by orange (green) oval. With $\Delta g = 0$, the spins remain in their initial configuration. With nonzero Δg, the spinor picks up singlet ($|S\rangle$) character over time t_1.

2.2.2 The Electroluminescence Power Efficiency Enhancement

The MEL effect is larger than the MC effect in our devices, and this implies that the device's electroluminescence power efficiency was improved by an applied magnetic field. The efficiency is given by the light output divided by the electrical input power and is therefore proportional to $EL(B)/I(B)$. Figure 2.5 b) shows a 60% increase in EL, whereas only 30% more current is drawn from the voltage source. We plot the MFE on electroluminescence quantum efficiency η vs. magnetic field B in

Figure 2.7. This figure is for an unconditioned device. Device conditioning refers to a procedure where the device is electrically stressed. We found that such a procedure can strongly enhance the MFE magnitude, but at the same time reduces the device's electroluminescence efficiency. Many of the figures below are for a conditioned device where the MFE magnitude has been optimized. Device conditioning forms an integral part of Yifei Wang's thesis, and additional details can be found there.

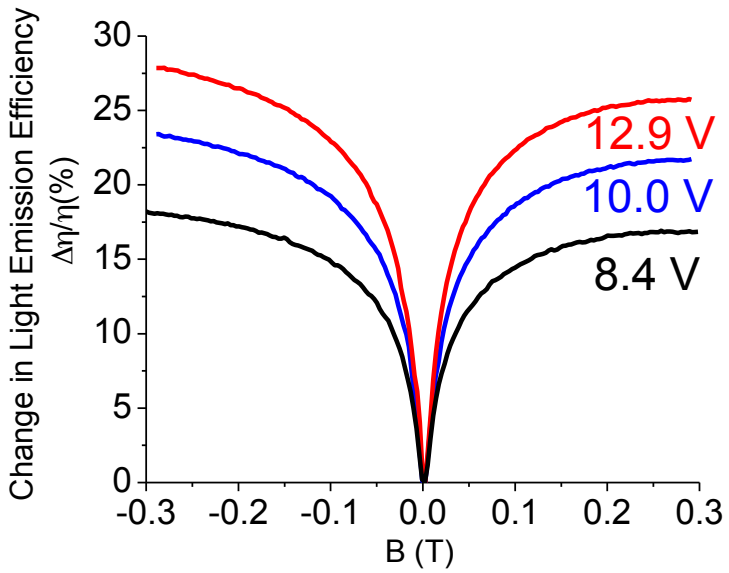

Figure 2.7: Magnetoefficiency in pristine device for three representative constant voltages.

2.2.3 Temperature Dependence of Magnetic Field Effects

Figure 2.8 a-b show magnetic field effects in conductance and electroluminescence as a function of temperature in electrically conditioned devices. The width, B_0, increases to up to $\approx$ 50 mT upon conditioning. This is much larger than the

expected hyperfine strength, B_{0hf}. Conversion to singlet exciplexes can occur only from triplet exciplexes that have been activated to near the singlet level. Therefore, the rate at which suitable triplets are formed (G_T) is less than that of singlet exciplex formation G_S. In general, therefore, $G_T < G_S$ except at high temperatures where $G_T \approx G_S$. Due to the increase in G_T, MFEs should increase with increasing temperature (contrary to many other kinds of magnetoresistance effects that often decrease with increasing temperature). As seen Fig. 2.8 c-d, the experimental data follows a simple Boltzmann law at temperatures above 200K with an activation energy $\Delta_{ST} \approx 60 - 80meV$. This agrees favorably with Δ_{ST} values found for a similar materials system in the literature [5].

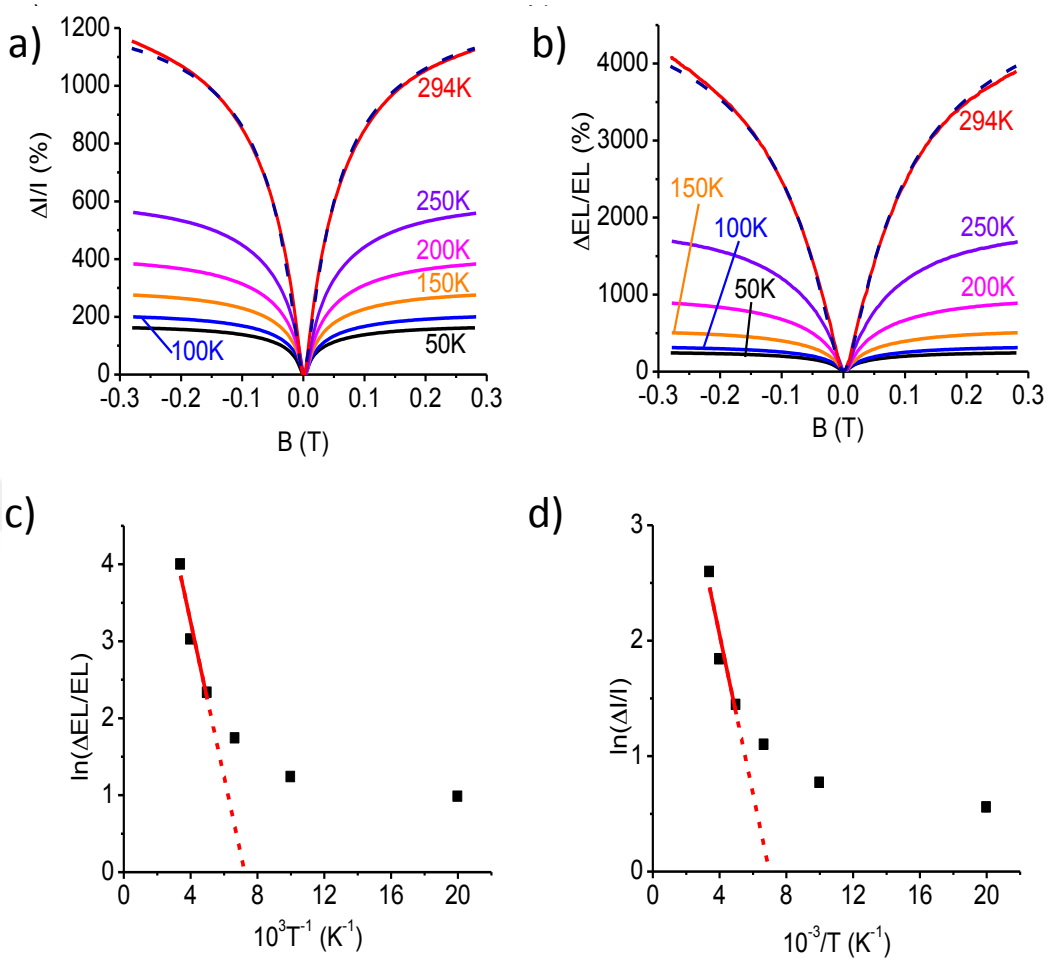

Figure 2.8: a) and b) Temperature dependence of magnetic-field-effects in optimally conditioned device. Dashed lines are non-Lorentzian (as defined in text) fits. c) and d) Arrhenius plot of the saturation magnetic field effect extracted from the data in a) and b), respectively. Solid lines are fits to an activated Boltzmann law indicating the range of data points used in the fit, whereas the dashed lines are extrapolations to lower temperatures.

2.2.4 Comparison of the Devices Fabricated with E-Beam and Thermal Evaporation

We compared MFEs in the devices that were fabricated using e-beam evaporation and thermal evaporation for the deposition of top metal electrode. These

two coating systems are schematically shown in Figure 2.9. It was found in earlier OMAR studies [39] that organic spintronic devices whose metallic top electrode was fabricated using e-beam evaporation show larger magnetoresistance than devices with a thermally evaporated top electrode. It was concluded that this is because traps are generated inside the organic layer resulting from X-ray bremsstrahlung exposure during the e-beam evaporation process. Traps affect magnetoresistance, the electroluminescence quantum efficiency and current-voltage characteristics [40, 41]. In general, traps are expected to enhance MFEs because the carriers will move more slowly through the organic film, thereby allowing a greater time for the spin-dynamics to act. We also investigate whether this effect might influence MFE of our exciplex devices. For this purpose, we have fabricated devices using e-beam and thermal evaporation for the deposition of top electrode/cathode. Figure 2.10a) and b) show MC and MEL measurements for the maximally conditioned thermally fabricated device as a function of temperature. We now compare these data for the thermally conditioned device to analogous data in an e-beam fabricated device (Fig. 2.10c) and d)). We find that the MFE in e-beam fabricated devices is smaller compared to devices fabricated by thermal evaporation that have been electrically conditioned. This implies that the traps formed by electrical conditioning are more efficient in enhancing OMAR than are the traps cause by X-ray exposure. We note that the e-beam devices are not susceptible to further electrical conditioning any more.

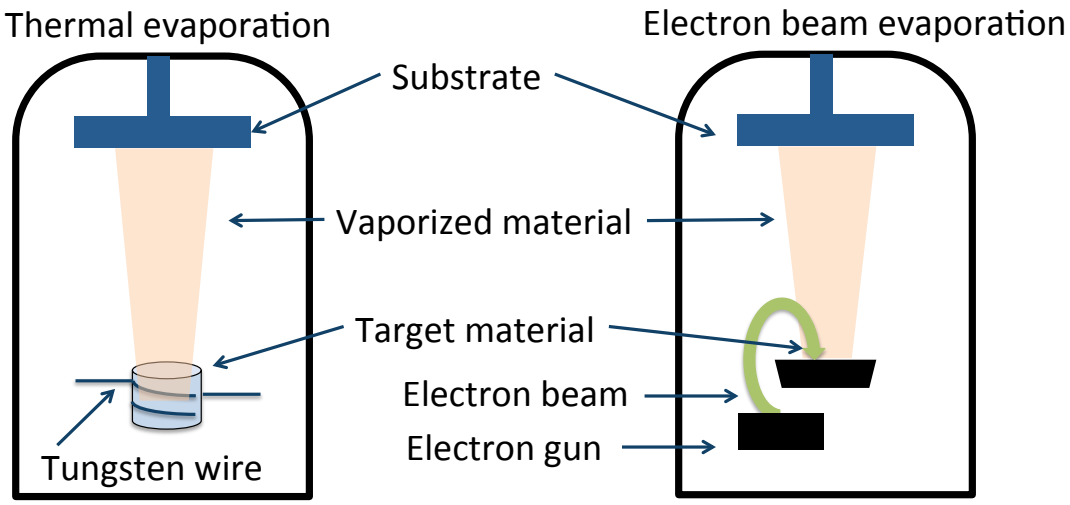

Figure 2.9: Types of evaporation processes: thermal evaporation process (left) and e-beam evaporation process (right).

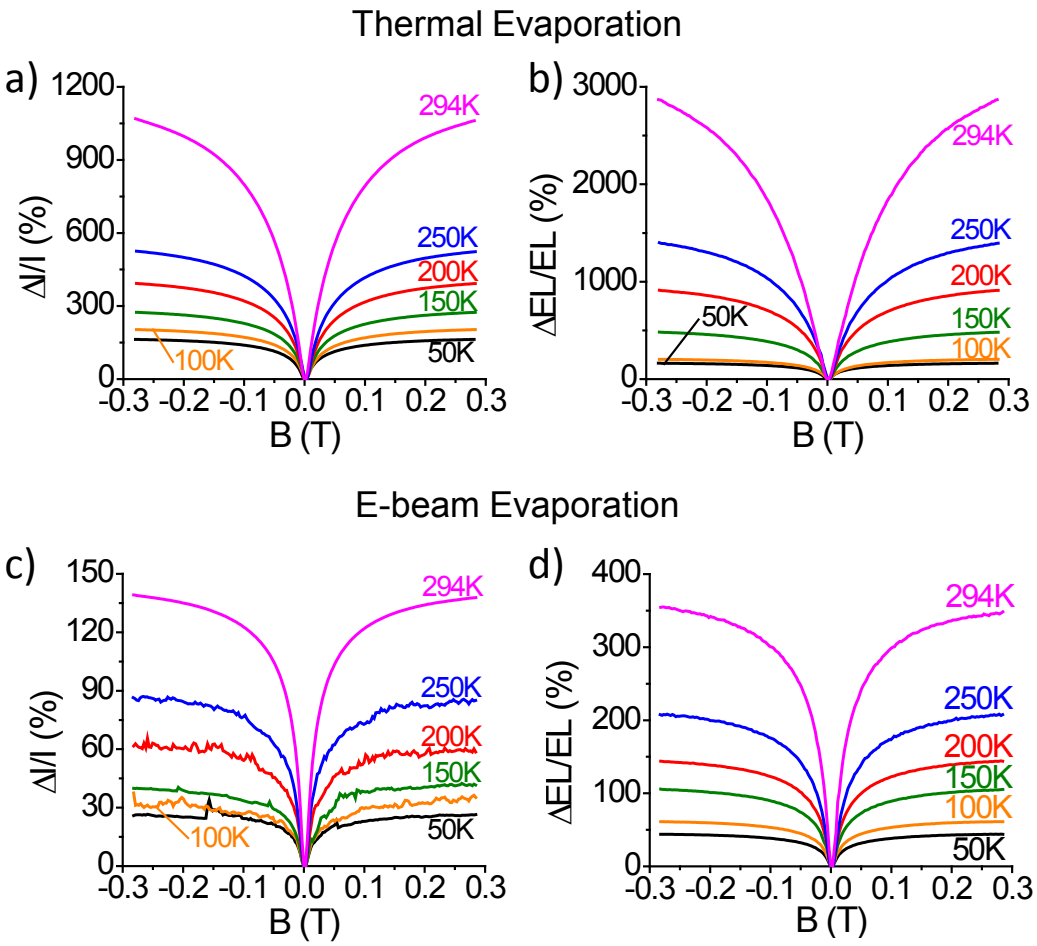

Figure 2.10: Magnetoconductance and magnetoelectroluminescence in TADF exciplex based devices that differ in the fabrication procedure used to deposite the top metal electrode. a), b) Devices whose top electrode was fabricated by thermal evaporation. c), d) Devices whose top electrode was fabricated by e-beam evaporation.

2.2.5 Comparison of Magnetic Field Effects in Exciplex Devices to Excitonic Devices

In this section we compare MFE in our exciplex system to the previously known excitonic MFE. The excitonic devices, with an organic luminescent or resistive layers of Poly[2-methoxy-5-(2-ethylhexyloxy)-1,4-phenylenevinylene] (MEH-PPV), con-

sist of a thin film of the organic semiconductor sandwiched between a top and bottom electrode. The indium tin oxide (ITO, 40 nm) coated glass substrates were obtained from Delta Technologies. The substrates were cleaned in an ultrasonic bath using acetone, methanol and isopropanol followed by oxygen plasma cleaning. The conducting polymer poly(3,4-ethylenedioxythiophene)-poly(styrenesulfonate) (PEDOT), purchased from Ossila Ltd., was spin coated at 4000 revolutions per minute (rpm) on top of the ITO to provide an efficient hole injecting electrode. All other manufacturing steps were carried out in a nitrogen glove box. The MEH-PPV (used as purchased from Sigma Aldrich) films were spin-coated from a toluene solution with concentration 5 mg/mL. The organic semiconductor layer thickness was $\approx$ 150 nm. The cathode layer consisting of calcium and aluminum was deposited by thermal evaporation or e-beam evaporation at a base pressure of 10^{-7} mbar on top of the organic semiconductor layer. The active device area was roughly $1mm^2$. Figure 2.11 shows the magnetic field effects in excitonic devices and exciplex devices.

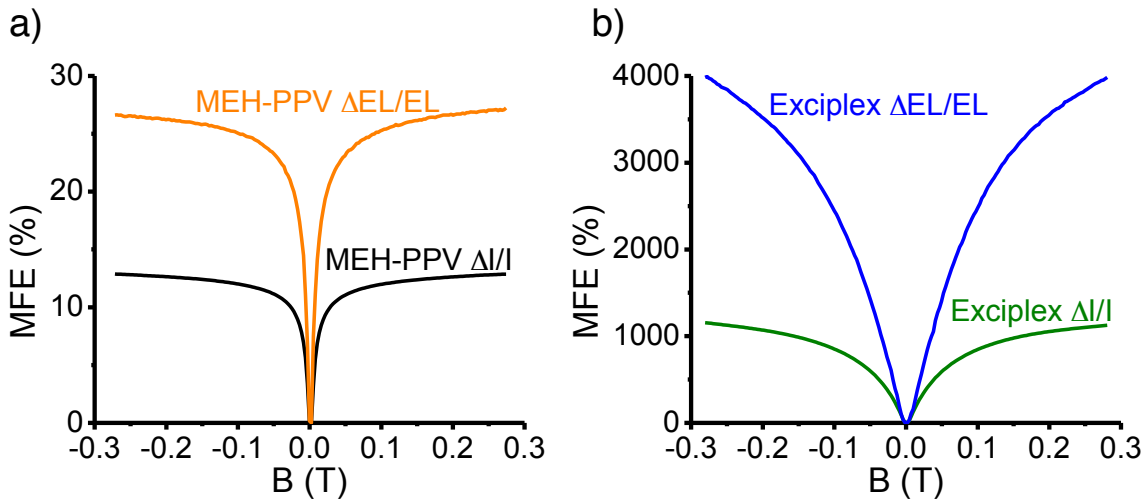

Figure 2.11: a) and b) Magneto-transport and magneto-luminescence in excitonic and exciplex devices, respectively.

For typical MFEs the dependence of conductivity (or luminescence) on magnetic field is commonly either Lorentzian, $\Delta I(B)/I \propto B^2/(B^2 + B_0^2)$, or follows a specific non-Lorentzian form, $\Delta I(B)/I \propto B^2/(|B| + B_0)^2$, for the change in the current I where $B_0 \approx 5$ mT [33]. We find that the data in Figure 2.11 can be accurately fitted by the non-Lorentzian expression. The exciplex MFE is much larger in magnitude than the corresponding effect in the excitonic device, validating our picture that the spin-physics in exciplex devices occurs in the exciplexes itself, rather than in the exciton precursor state (polaron pairs). The width of the traces is much bigger in exciplex devices than in excitonic devices, validating our picture that the spin-dynamics is not caused by hyperfine precession any more in exciplexes, but is rather due to the Δg mechanism.

CHAPTER 3
MAGNETIC FIELD EFFECTS IN BIPOLAR AND UNIPOLAR REGIOREGULAR POLY (3-HEXYLTHIOPHENE) (P3HT) DEVICES

Spintronics is the field of science and technology that uses both the electron's charge and its spin to store, manipulate, and transport information [42, 43]. The spin valve is the most basic spintronic device, and consists of two ferromagnetic electrodes and a non-ferromagnetic layer between them. If the two ferromagnetic electrodes are engineered to switch their magnetization at different applied magnetic field values, a magnetic field applied to the electrodes switches the devices between an parallel and antiparallel magnetization configuration. The resistance of the device changes as the configuration switches between the two configurations, a phenomenon referred to as Giant Magnetoresistance (GMR) [7, 8]. As the name implies this effect can be relatively large, typically a greater than 10% change in resistance. With few exception such large effects require using magnetic materials. However, in this chapter, we study a large, low-field, room-temperature magnetoresistive effect (OMAR) in organic semiconductor devices (organic magnetoresistance, OMAR) [44–49]. that occurs in devices without magnetic electrodes [19, 22, 34], and its magnitude typically still 1-10%. It has experimentally shown that OMAR is related to spin dynamics involving spin dependent interactions between pairs of paramagnetic species [30, 46]. Understanding the mechanism that causes the OMAR effect can lead to further understanding of spin and charge transport in organic semiconductors and spintronics in general. The OMAR effect is generally only observed when the organic semicon-

ductor's molecular structure contains hydrogen atoms [50]. Furthermore, the crucial property imparted by these hydrogen atoms is the hyperfine interaction, i.e. the interaction between the electron spin and nuclear spins. This fact was shown in OLEDs made with deuterated π-conjugated polymers [51]. As the nuclear dipole moment of the deuterium is smaller than ordinary hydrogen, it causes a weaker hyperfine interaction, and this difference was successfully detected. This clearly suggests that OMAR is caused by hyperfine coupling. For completeness we note however, that it is not always the hyperfine interaction that is dominant, in some materials systems it may be spin-orbit coupling, i.e. the interaction between the electron's spin with its orbital momentum. It is found that the delta-g mechanism (related to spin-orbit coupling) produces the most significant contribution to OMAR in some materials [29,49,52,53]. However in this chapter, we show that the hyperfine interaction is dominant for the materials we used here [30].

Although there is an agreement that spin coupling is involved in the OMAR effect, there is an ongoing debate about which specific paramagnetic species are actually involved. Electrons and holes, triplet excitons, or bipolarons are some of the different species that are held responsible for OMAR depending on experimental conditions and device structure [54]. In earlier studies, the individual contributions due to these paramagnetic species have usually been isolated by introducing additional layers to the device structure or by blending several materials. [29, 55, 56], but this often complicates the analysis. Moreover, polythiophene:poly-polystyrene sulfonate (PEDOT:PSS) is often used as a hole injection layer in the device structure, and it

has been shown that it has its own magnetoconductance (MC). Therefore, this creates problems in devices with MC effects of only a few percent [57]. In this chapter we will present OMAR effect studies in single layer devices made from regioregular poly (3-hexylthiophene) (RR-P3HT) with different electrode materials to understand which model can best to explain the effect, possibly depending on the operating regime of the device. RR-P3HT is a commonly used polymeric semiconductor with superior film forming properties and high carrier mobility. For those reasons, it is often used in transistors. We used transport and luminescence spectroscopies to isolate the different mechanisms and identify their fingerprints.

3.1 Models for OMAR

There are three models that have been proposed to explain OMAR effect: bipolaron model, electron-hole pair model, and triplet-polaron quenching model.

3.1.1 Bipolaron Model

Charge carriers (polarons) hop from molecular site to molecular site [18]. On each site, their spin precesses around the local magnetic field in the absence of an applied magnetic field (Figure3.1 a). The sum of the nuclear hyperfine fields of the hydrogen nuclei in the molecular structure forms the local field for each molecular site. As a result, the local magnetic field is randomly oriented from site to site [58]. If a polaron encounters a singly occupied site along its hopping path, it may possibly move to this site and form a bipolaron (a doubly charged molecule). The relative spin orientation of the two polarons plays an important role in bipolaron formation. If the

two spins are in a triplet configuration, for example if they are parallel, spin blocking occurs. This is because according to the Pauli Exclusion Principle, two parallel spins cannot occupy the same site unless one is in a higher orbital, but this is energetically unfavorable. To make the bipolaron-forming hop possible, the parallel orientation of polarons' spins will have evolve over time to acquire a singlet amplitude. This can happen since they precess about the random localized hyperfine fields of their respective site, where the local magnetic fields point in different directions. In contrast, the net local fields become more and more aligned when an external magnetic field is applied (Figure 3.1 b). The formation of a bipolaron and hopping becomes more unlikely as the polarons' spins precess over increasingly similar orientations with a greater applied magnetic field. Because all paths including an already occupied site in a triplet configuration with the moving carrier are no longer available for conduction, Pauli blocking increases the device resistance. Therefore, given this simple description of the bipolaron model it is expected to result in a negative MC with applied magnetic field. This bipolaron model has been studied in detail by Bobbert et al. [59].

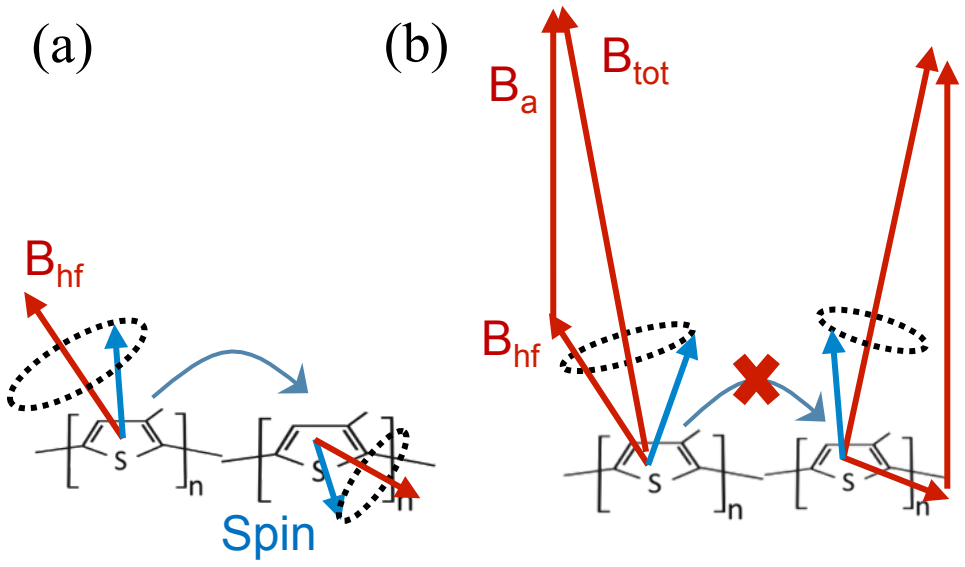

Figure 3.1: a) Precession of a polaron's spin about randomly oriented hyperfine fields (B_{hf}), allowing for bipolaron formation. b) Application of a large external magnetic field aligns the local fields, leading to spin blocking of a triplet pair.

3.1.2 Electron-Hole Pair Model

The electron-hole pair model (Figure 3.2) considers the effect that an applied magnetic field has on the recombination of two carriers to form an exciton. The exchange energy of an electron-hole pair (where the two carriers sit on neighboring molecules) is small compared to the exciton exchange energy (on the order of 1eV, here both carriers are located on the same molecule) [60]. The triplet exciton's wave function is much more localized than the singlet exciton, which lies at a higher energy. The formation rate for triplet excitons, k_T, differs from the formation rate for singlet excitons, k_S because of this difference. This model predicts a positive magnetic field effect on electroluminescence (EL), or magnetoluminesce (MEL), for a k_T that is

larger than k_S and negative if k_T is smaller than k_S. This follows from a detailed treatment of the competition between spin dynamics and exciton formation [61]. Experimentally a positive MEL is found [30, 44, 45], which implies that k_S is smaller than k_T. Th model generally predicts a positive MC, independent of the relative size of k_S and k_T. This is because an applied magnetic field suppresses the overall recombination rate regardless of the relative values of k_T and k_S, and this leads to a greater number of charge carriers available for conduction. More specifically, because of the decreased recombination efficiency there is a larger overlap of the positive and negative charge carrier populations within the device because carriers can move deeper into the device before recombining. Therefore device's space charge is reduced, creating more current [62].

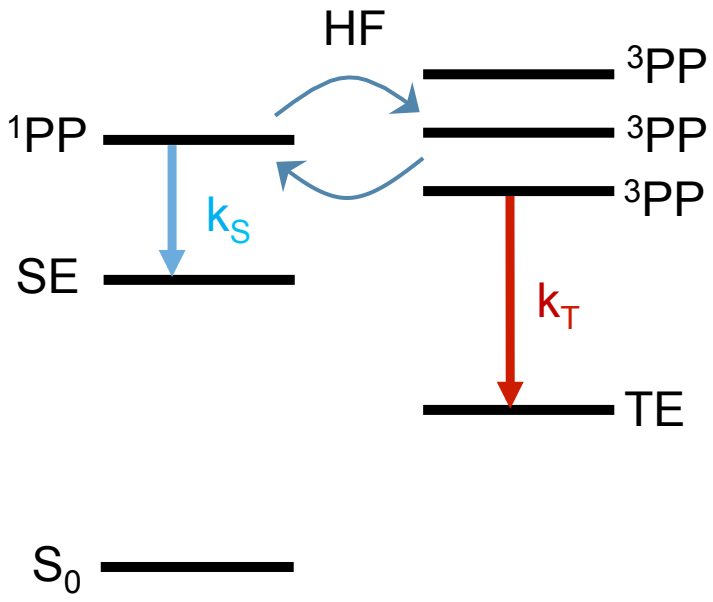

Figure 3.2: Energy levels for polaron pairs and excitons. The hyperfine field (HF) mixes triplet and singlet polaron pairs with each other. Singlet polaron pairs (^1PP) form singlet excitons (SE) with a rate k_S whereas triplet polaron pairs (^3PP) form triplet excitons (TE) with a rate k_T. The ground state S_0 is also shown.

3.1.3 Triplet-Polaron Quenching Model

The triplet-polaron quenching model is based on spin-dependent reactions between a triplet exciton and a polaron [25]. TPQ model relies on the presence of excitons (and therefore requires positive and negative charges to be present). Desai et al. showed [25] that a competition between triplet-exciton quenching and triplet-exciton dissociation causes a sign change in the OMAR effect. But as we will show later in this chapter, we do not believe it makes a significant contribution to OMAR in our devices, therefore we will not discuss this model in more detail.

3.2 Fabrication and Measurement

To study the importance of bipolarons and electron-hole pairs in the OMAR mechanism, we fabricated three sets of devices[1], each with the general structure of an organic layer sandwiched between anode and cathode (Figure 3.3 a). For the organic layer, we selected RR-P3HT, a commonly used polymer for solar cells [64] and organic thin film field effect transistors [65]. The anode and cathode materials were selected based upon the desired charge carrier injection [66, 67]. Figure 3.3 b-d shows the energy level diagrams for each. The bipolar device (Figure 3.3 b) uses indium tin oxide (ITO) as the anode which aligns well with the highest occupied molecular orbital (HOMO) of RR-P3HT, allowing for efficient injection of holes into the organic layer. In the bipolar device, the injection of electrons and holes is fairly balanced. We compared this device to one in which either electron or hole injection was disproportionately large. We will refer to these devices as unipolar electron-only devices and unipolar hole-only devices for the purposes of identification. However, it should be recognized that a small population of the second charge carrier type was still injected. For the cathode, calcium was used. The unipolar (electron-only) device (Figure 3.3 c) keeps the calcium cathode but replaces ITO with magnesium for the anode. With a work function of -3.7 eV, magnesium makes injection of holes into the HOMO (-5.2 eV) difficult. Finally, the unipolar (hole-only) device (Figure 3.3 d) was fabricated with gold as the anode and ITO as the cathode. With a work function of

[1]The results of this study were published as a journal article [63]. Some parts of this chapter were included from this publication.

-4.7 eV, ITO is inefficient for injecting electrons into the HOMO (-3.0 eV).

For the bipolar and hole-only devices we started with glass substrates pre-coated with an ITO layer of 40 nm purchased from Delta Technologies. These, along with the glass substrates for electron-only devices were cleaned in an ultrasonic bath with acetone, detergent, deionized water, and isopropanol followed by oxygen plasma cleaning. A bottom layer of magnesium was evaporated by electron beam for the electron-only devices at a base pressure of 10^{-7} mbar. All other manufacturing steps were carried out in a nitrogen glove box. RR-P3HT (purchased from Sigma Aldrich) was deposited by spin-coating from a chlorobenzene solution with a concentration of 25 mg/mL. The organic semiconductor layer thickness was $\approx$ 70 nm. Top electrodes were deposited by thermal evaporation. The active device area was roughly 0.6×0.6 mm^2.

Devices were operated in the dynamic vacuum of a closed-cycle He cryostat. However, all measurements were taken at room temperature. The cryostat was placed between the poles of an electromagnet. Constant voltage (V) and constant current (I) measurements of MC and MEL were performed using a Keithley 2400 Source Meter. We used a photomultiplier tube to measure the electroluminescence intensity.

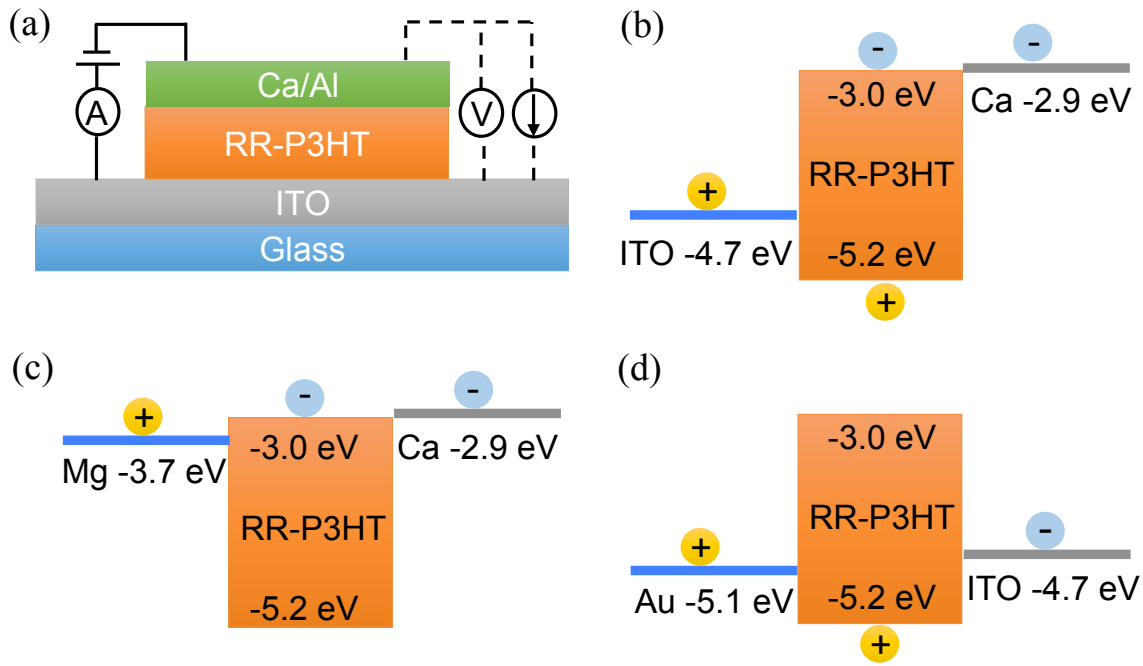

Figure 3.3: P3HT device structure and energy levels. a) Schematic device structure showing two measurement techniques: constant current (dashed) and constant voltage (solid). b) Energy level diagram for the bipolar device. c) Energy level diagram for the unipolar "electron-only" device. d) Energy level diagram for the unipolar "hole-only" device.

3.3 Experimental Results

The electron-hole pair model requires the injection of both types of charge carriers while the bipolaron model relies only on one. Therefore, if OMAR were measured in unipolar devices, it would not be the result of the electron-hole pair model. The effect of an external magnetic field on the current for unipolar electron-only devices is shown in Figure 3.4. MC, defined as

$$MC(\%) = \frac{I(B) - I(0)}{I(0)} \cdot 100\% \tag{3.1}$$

is plotted versus applied magnetic field, B. The measured MC is negative at

all voltages. These findings are consistent with the spin blocking predicted by the bipolaron model. We note that negative MC in unipolar devices has been observed before in the context of ultra small field effects in a different organic material [68], but it was not further analyzed. All MC traces were fit using the empirical function

$$MC(\infty)\left[\frac{B}{(|B|+B_0)}\right]^2 \tag{3.2}$$

that is commonly used to fit MC curves and is referred to as the weakly saturating (or non-Lorentzian) function in MC literature [30, 54]. B_0 is a fitting parameter and is equal to the width of the OMAR curve at quarter-saturation whereas $MC(\infty)$ refers to the value of MC at infinite B. The traces were fit with values of B_0 on the order of mT as shown in Table 3.1. We note that the values we find of B_0 are typical of the hyperfine field [30]. At its maximum, the effect reaches nearly - 4%. In contrast, measurements for unipolar hole-only devices showed only a minuscule effect. For comparison, one of these traces is included as the dashed line near zero in Figure 3.4. It is often found that the hole's mobility is greater than that of electrons in RR-P3HT [69, 70]. This difference can explain the disparity in MC for the two sets of devices. With a lower mobility, charge carriers will occupy sites longer (slow hopping regime). This provides more time for the spin to precess around the local hyperfine field and increase its singlet configuration with other charge carriers [18]. As the mobility increases, the ratio of the charge's hopping frequency to the hyperfine precession frequency becomes larger making the formation of a bipolaron unlikely.

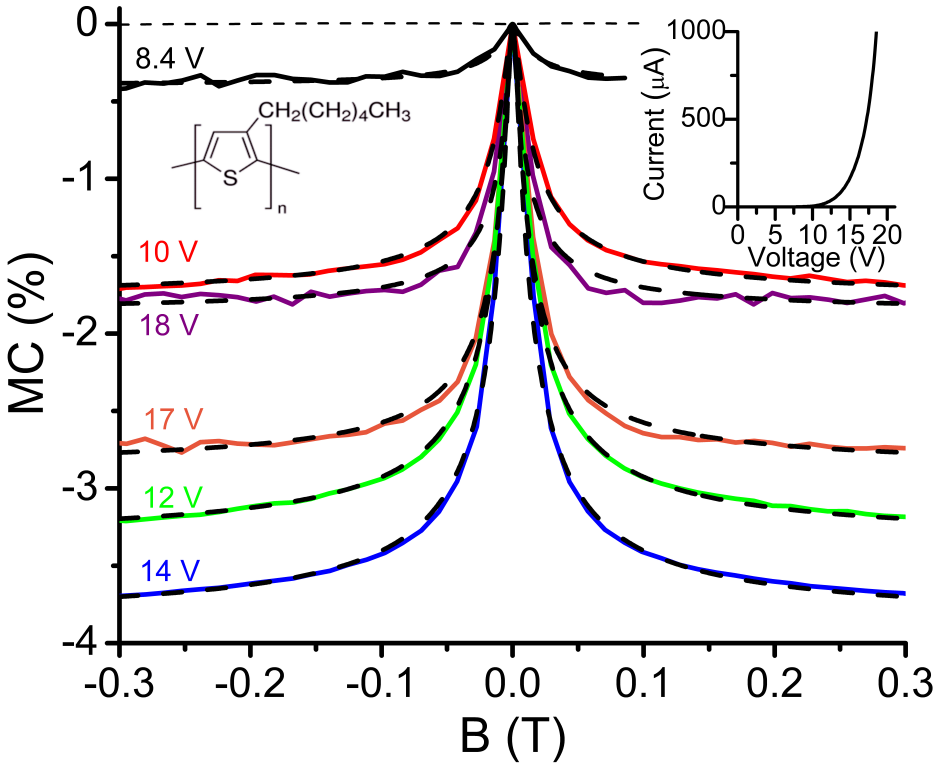

Figure 3.4: Solid curves: Magnetoconductance (MC) measured for RR-P3HT devices (molecular structure shown) at constant voltages for unipolar electron-only devices. The dashed black lines are fit to the non-Lorentzian line shape. The dashed line near the top of the graph corresponds to the much smaller effect measured for unipolar hole-only devices. Inset: Current versus voltage for electron only devices.

Next, MC for a bipolar device was measured to determine if it would show similar OMAR traces to those of unipolar devices (Figure 3.5). While the measured MC is negative at low voltage, just as in unipolar devices, it deviates from unipolar devices at higher voltages. It decreases in magnitude, eventually crossing over to a positive effect, and then increases in magnitude. Of particular note are the measurements taken at 4.0 V, which show a small but positive OMAR for small magnetic

field crossing over to a negative effect for larger applied fields. This crossing was seen for all bipolar devices measured. With the exception of the 4.0 V curve, all the OMAR traces were fit using the same weakly saturating function used for the unipolar devices. See Table 3.2 for the values of the fitting parameters. The fit for the 4.0 V trace was achieved using a superposition of two weakly saturated functions, one negative and one positive, with values of $MC(\infty)$ close to the values for the nearest traces (3.6 V and 4.2 V) and values of B_0 on the order of mT for the hyperfine field. This supports our assertion that the OMAR effect can be modeled as being produced by two competing effects, one positive and one negative. At low voltage, the device is in the unipolar domain. The difference between the work function of calcium and the LUMO is less than the difference between the work function of ITO and the HOMO. Consequently, electrons inject first because their injection barrier is smaller. This means that at low voltage a negative OMAR is measured in agreement with our results in the electron-only device (see Figure 3.4). Comparing tables, we see that in the low voltage regime values of B_0 for both devices are around 5 to 7 mT. This indicates that in both cases the same mechanism is at work for the negative MC. As the voltage is increased, and holes begin to be injected into the organic layer, electron-hole pair recombination dependence on magnetic field becomes a factor. Now two mechanisms are at work, one increasing, the other decreasing the current. In Table 3.2, we see that in the high voltage regime the values of B_0 are significantly smaller than those seen in the unipolar device, lending additional support to the notion that the positive MC comes from a different mechanism.

Table 3.1: Summary of parameters used to fit the data curves in Figure 3.4 (electron-only devices)

Voltage (V)	B_0 (mT)	$MC(\infty)$
8.4	7.1	0.40
10	7.6	-1.8
12	6.9	-3.4
14	6.6	-3.9
17	5.6	-2.9
18	4.7	-1.9

Table 3.2: Summary of parameters used to fit the data curves in Figure 3.5 (bipolar devices)

Voltage (V)	B_0 (mT)	$MC(\infty)$
3.4	5.3	-1.079
3.6	6.8	-0.658
4.0	20	-0.394
4.0	6.5	0.23
4.2	2.4	0.476
4.4	2.9	0.972
5.4	3.5	1.786

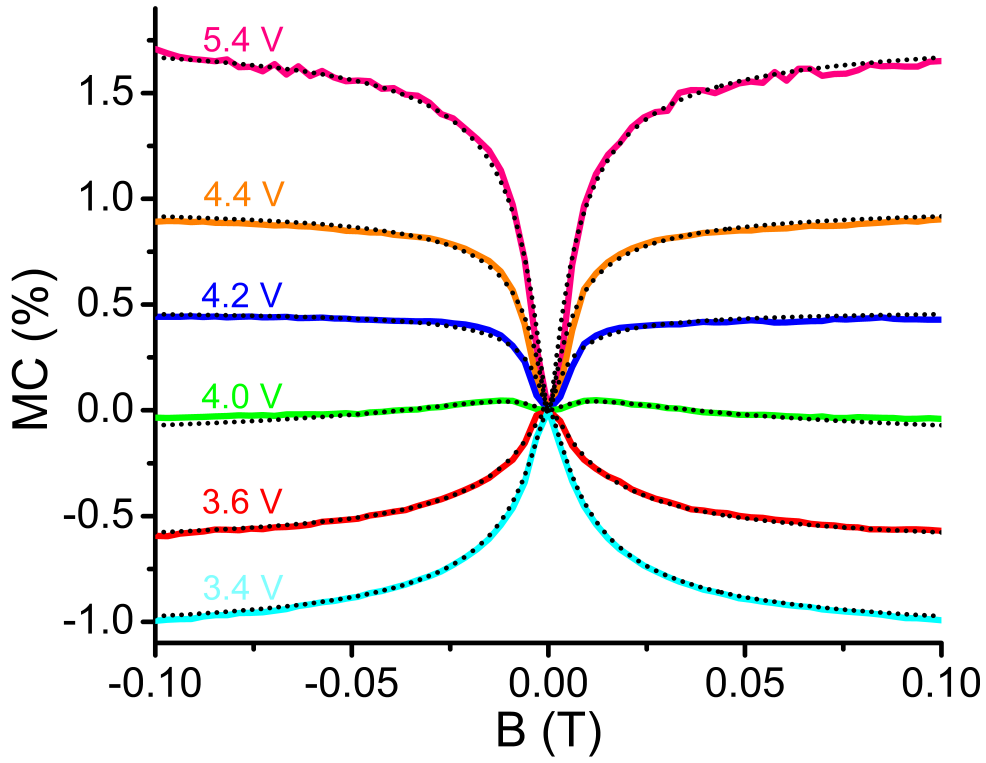

Figure 3.5: Solid curves: Magnetoconductance (MC) for bipolar RR-P3HT device structure measured at constant voltages. The dotted black lines are fit to the non-Lorentzian line shape with the exception of 4.0 V which was fit using two non-Lorentzian functions.

The effect first becomes positive at 4.0 V. We have already established that the MC effect in unipolar devices is negative, which can be explained by the bipolaron model. We propose that the positive effect in the bipolar devices is due to the electron-hole pair mechanism. As described in the introduction, the electron-hole pair mechanism is primarily an effect on EL efficiency. Therefore to confirm this connection between the positive MC and electron-hole pairs, the EL of the devices

were measured. Figure 3.6 a inset shows the EL as a function of the device current as a log-log plot. It is seen that the EL of the unipolar device for all currents is at least two orders of magnitude smaller than for that of the bipolar device. This demonstrates that the hole current is much smaller than that of the electron current in the unipolar device, confirming our assertion that the device is nearly electron-only. We note that the EL for the unipolar and bipolar devices can be compared because they both had the same active area. While the EL for the bipolar device was measured through its transparent ITO electrode, the EL for the unipolar device was measured through a semitransparent bottom electrode. To correct for this, the transmission spectrum of the unipolar device's bottom electrode was measured and the EL accordingly adjusted.

Figure 3.6 b shows the magnetic field effect on quantum efficiency, η. η is defined as the ratio of photons exiting the device to charge carriers flowing into the device (current). The EL measured by the photomultiplier tube is proportional to the photon flux. The quantity plotted in Figure 3.6 b inset, EL/I, is proportional to η whereas $\Delta(EL)/(EL)$ measured at constant current is equal to $\Delta\eta/\eta$ since the proportionality factors in the denominator and numerator cancel. Figure 3.6 b inset shows that the device is operating in the bipolar regime above 4.0 V, where there is efficient EL. In agreement with our assertion the positive contribution of the MC is due to electron-hole pairs, Figure 3.6 b shows that there is a sizable magnetic field effect on η when operated above 4.0 V where there is also a positive MC. In contrast, when the device is operated in the unipolar regime (3.3 V and below) the effects on

η are essentially absent and the MC is negative.

In addition to the electron-hole pair model, there is another mechanism that has been proposed that operates in the bipolaron regime. This mechanism has been called the triplet exciton-polaron quenching mechanism and is based on the spin dependent and magnetic field dependent interactions between triplet excitons and polarons [71]. However, because the triplet exciton-polaron mechanism does not involve singlet excitons directly there is no reason to expect that this mechanism would lead to a significant change in η. This follows from the fact that EL only originates from the recombination of singlet excitons whereas triplet excitons do not make a significant contribution to the photons emitted. In principle, there could be a secondary effect on EL due to the triplet exciton-polaron mechanism. However, with $\Delta\eta/\eta$ reaching 6% and a MC of only 1.5% the effect on η is the primary effect implying that the mechanism at work involves singlets directly. For these reasons, we do not believe that the triplet exciton-polaron mechanism produces a significant contribution to the magnetic field effects in our devices for the operating regime in which they were studied.

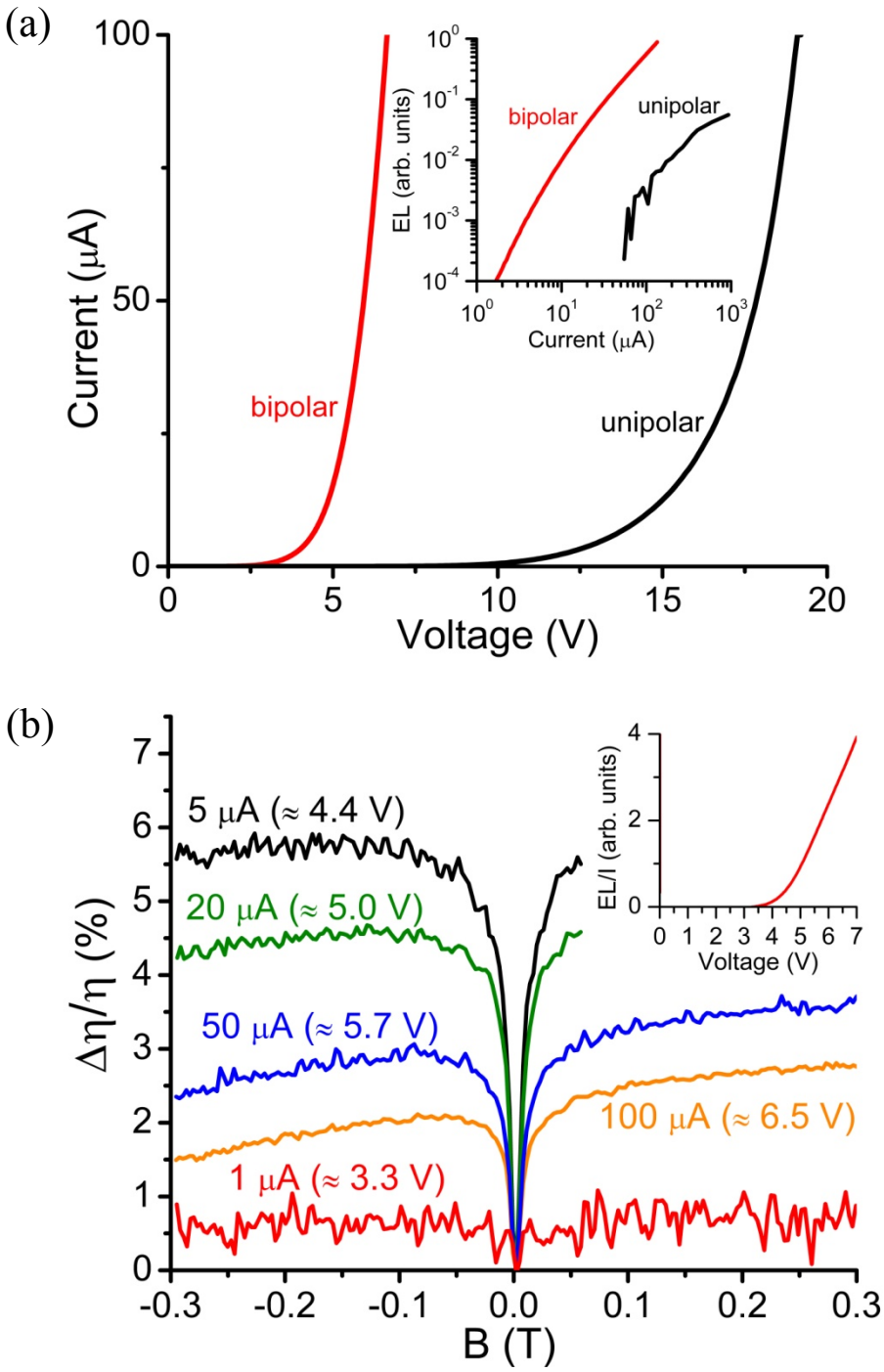

Figure 3.6: a) Current-voltage plot for bipolar and unipolar devices. Inset: log-log plot of EL as a function of current for both devices. b) Magnetic field effect on the electroluminescence efficiency as a function of magnetic field measured at a constant device current in the bipolar device. Also included are the approximate bias voltages required for each current. Inset: Electroluminescence efficiency in arbitrary units plotted versus device voltage.

3.4 Conclusions

In conclusion, we studied organic diodes of regioregular polythiophenes (RR-P3HT) fabricated with various anode and cathode materials to determine the importance of bipolarons and electron-hole pairs for magnetoconductance (MC). Near-unipolar, electron-only, devices (Mg/RR-P3HT/Ca) displayed negative MC at all voltages. This was attributed to the bipolaron mechanism which produces spin blocking and only requires a single type of charge carrier. Near-unipolar, hole-only, devices (Au/RR-P3HT/ITO) showed no MC due to the holes' high mobility which does not allow sufficient time for the spin precession needed for the efficient formation of bipolarons. Both a negative (low voltage) and positive (high voltage) MC were measured in bipolar devices. An analysis of the electroluminescence efficiency, η, versus voltage showed that at low voltages the device operated in a unipolar regime. Therefore, as in the electron-only devices, the negative MC could be attributed to the bipolaron mechanism. Above 4.0 V, where the device operates in a bipolar regime and a positive MC was measured, a sizable magnetic effect on η was measured as well. Therefore, the positive MC was attributed to the electron-hole pair model, which primarily affects η and produces a corollary effect on conductance.

CHAPTER 4
HYBRID ORGANIC-INORGANIC PEROVSKITE SOLAR CELLS

Although single-junction solar cells made from crystalline materials have been reported to achieve nearly 30% power conversion efficiencies (PCEs) [72], they have high manufacturing cost when used at large scales. Over the past several years, organic-inorganic hybrid perovskites have been extensively studied because of their direct band gap, large absorption coefficient, and long carrier diffusion length. Hybrid organic-inorganic perovskites, named after the Russian mineralogist L.A. Perovski, are materials described by the formula ABX_3, where A is an organic cation (e.g. $CH_3NH_3^+$), B is a metal cation (Pb^{2+} or Sn^{2+}), and X is usually a monovalent halide anion (I^-, Br^- or Cl^-). Figure 4.1 shows the crystal structure of such perovskites.

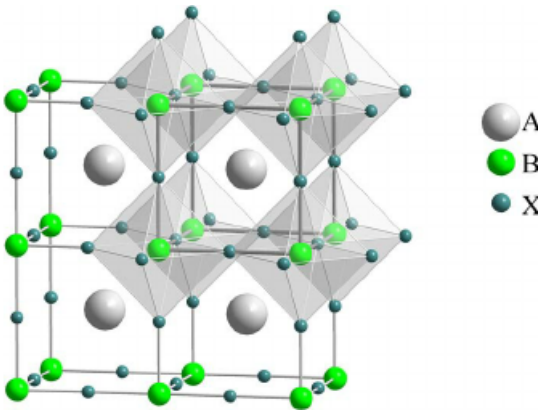

Figure 4.1: The basic structure of perovskite. [73]

In 1994, Mitzi et al. reported layered organometal halide perovskites and

showed a semiconductor-to-metal transition [74]. They observed a dimensionality increase from 2D to 3D, and the band gap decreased as a result of this increase. Miyasaka and co-workers [75] used the 3D perovskite $CH_3NH_3PbX_3$ (X=Br, I) and achieved a power conversion efficiency of 3.1% for X=Br and 3.8% for X=I in dye sensitized solar cells. Park et al. [76] fabricated 6.5% efficient perovskite quantum-dot-sensitized solar cells. There is a stability problem when organolead halide perovskite is used in liquid electrolyte-based sensitized solar cells. Kim et al. [77] solved this problem by using a solid hole conductor instead of the liquid electrolyte. Snaith et al. [78] reported solution-processable 10.9% efficient hybrid solar cells by replacing mesoporous n-type TiO_2 with insulating Al_2O_3. Continuous progress has been made since then, and Shin et al. [79] showed a steady-state power conversion efficiency of 21.2% with photoelectrode materials Lanthanum (La) doped $BaSnO_3$ (LBSO) for photostable perovskite solar cells.

4.1 The Physics of Solar Cells

A solar cell is a semiconductor PN junction diode, and its structure is shown in Figure 4.2. In a solar cell, the sunlight absorbed by a semiconductor generates a hole/electron pair or an exciton. This occurs when the band-gap energy of the semiconductor is lower than the energy of the photon. Generated holes and electrons are separated by the built in electric field of the junction, and they head toward the respective electrodes. When the cell is illuminated, a current flows in an external load caused by the energy from the light.

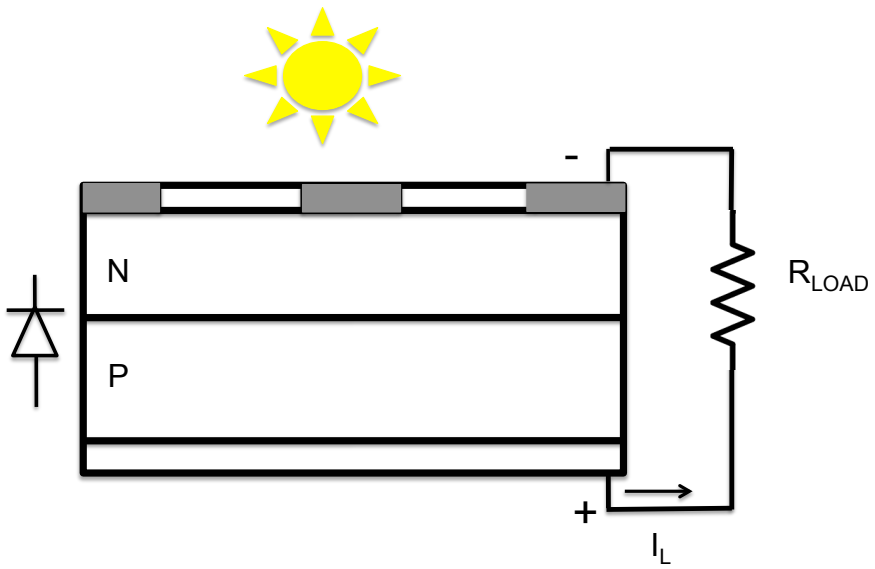

Figure 4.2: The basic structure of a solar cell.

There is no current flow through the cell when there is no illumination. With incident sunlight, the cell develops a photovoltage. In Figure 4.3, a typical current vs. voltage characteristics for a diode with and without illumination is shown in red line and in black line, respectively. The open circuit voltage (V_{OC}) develops between the isolated terminals when the external load resistance is very large or infinite. In contrast when the external load resistance is zero, the maximum current in the solar cell is called short circuit current (I_{SC}).

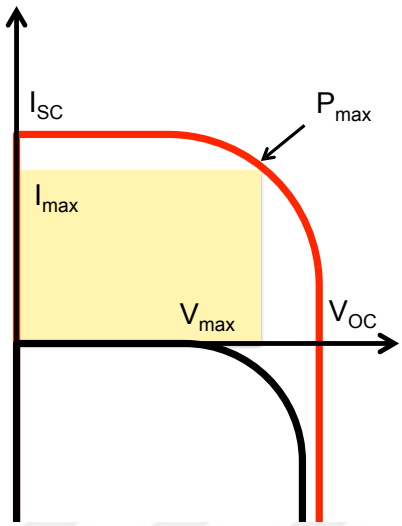

Figure 4.3: Typical current vs. voltage curve for a PN diode with (red line) and without (black line) illumination.

Obviously for open circuit and short circuit conditions the power delivered to the load is zero, and the maximum power, P_{max}, is delivered at a specific load resistance value. The fill factor (FF) is a common parameter of a solar cell, and it is defined as P_{max} divided by the rectangular area formed by I_{SC} and V_{OC}

$$FF = \frac{P_{max}}{I_{SC}V_{OC}} \tag{4.1}$$

The power efficiency of a solar cell is the ratio of the power delivered at the maximum power point, to the incident light power:

$$\eta = \frac{P_{max}}{P_{in}} = \frac{I_{SC}V_{OC}FF}{P_{in}} \tag{4.2}$$

P_{in} is the incident power, and the power density from sunlight on the surface of the earth is 1000 W/m^2 (AM 1.5).

Figure 4.4 shows the equivalent circuit of a solar cell. In the dark, the solar

cell behaves like a diode, and under an applied voltage the current is called the dark current, $I_{dark}(V)$. When the cell is illuminated the diode current (I_D) flows opposite direction to the photocurrent (I_I), and it reduces the net current. Equation 4.3 gives an ideal solar cell under illumination in the approximation that the diode current is equal to the dark current,

$$I = I_I - I_D = I_I - I_{dark}(V) = I_I - I_o(e^{\frac{eV}{kT}-1}) \tag{4.3}$$

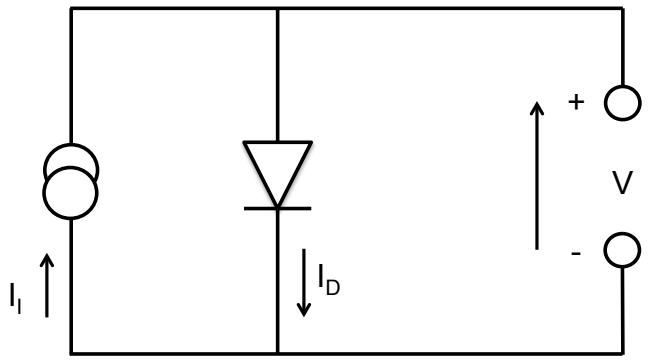

Figure 4.4: Equivalent circuit of a solar cell.

As the power dissipates through contact resistance and current leakage, a solar cell generally cannot reach its theoretical best performance. The shunt resistance (R_{sh}) and the series resistance (R_s) are parasitic resistances. R_{sh} is due to current leakage , and R_s is due to the solar cell material and the contacts. Now equation 4.3 becomes

$$I = I_I - I_o(e^{\frac{e(V+IR_s)}{nkT}} - 1) - \frac{(V + IR_s)}{R_{sh}} \tag{4.4}$$

where n is the diode ideality factor. The equivalent circuit in Figure 4.4 becomes

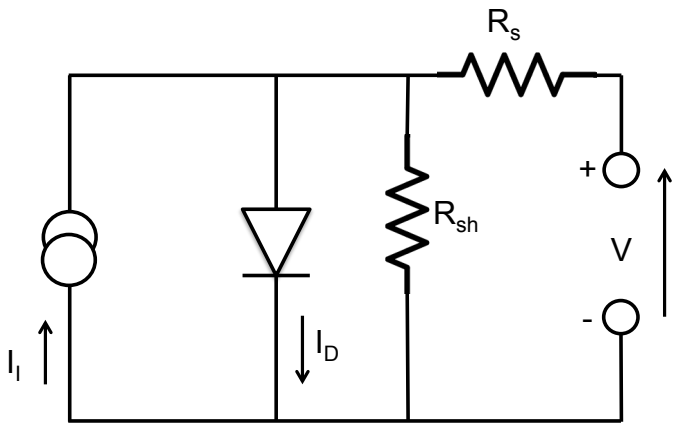

Figure 4.5: Equivalent circuit of a solar cell with series and shunt resistance.

For an ideal solar cell, R_s should be zero and R_{sh} should be infinity.

4.2 The Structure of Perovskite Solar Cells

The first use of organo-metal halide perovskites in photovoltaics were as direct replacements for dye sensitizers in the dye sensitized solar cells (DSSCs) [75,76]. There is a several-micron thick porous TiO_2 layer, coated and penetrated with an absorber dye material, in a typical DSSCs. A liquid electrolyte that contains a redox couple is in contact with the electrode assembly [80]. TiO_2 collects and transports the electrons, whereas the electrolyte conducts the holes in these devices. Originally perovskite materials were simply replacements for the dye using this same structure [77, 78]. In

a mesoscopic device structure (Figure 4.6 a) a solid-state hole conductor was used instead of the liquid electrode [77, 78], and this advance made a great impact in solar cell community. In a planar perovskite solar cell structure, the light absorber is sandwiched between electron and hole transporting materials. These planar structures can be categorized as either the conventional n-i-p structures (Figure 4.6 b) or the inverted p-i-n (Figure 4.7 a), depending on the transport material that the light encounters first. A mesoscopic p-i-n structure (Figure 4.7 b) has also been developed by several groups [81, 82]. Different device structures require different processing and fabrication processes, and this determines which electron transport materials (ETM), hole transport materials (HTM), anode materials, and cathode materials are used.

4.2.1 Conventional n-i-p Structure

High-performance devices have been fabricated using the mesoscopic n-i-p structure. As can be seen from the structure (Figure 4.6a), the device consists of a transparent conducting oxides (TCO) cathode, (50-70 nm thick TiO_2) as an ETM, a mesoporous metal oxide (150-300 nm thick mp-TiO_2) filled with perovskites, perovskite capping layer (300 nm), a hole conductor layer (150-200 nm thick 2,2',7,7'-Tetrakis[N,N-di(4-methoxyphenyl)amino]-9,9'-spirobifluorene (spiro-MeOTAD)), and a metal anode (50-100 nm thick Au or Ag).

When a mesoscopic layer is used the carrier transport distance is decreased, and this enhances the charge collection while also increasing photon absorption due to light scattering, and preventing direct current between the two contacts. [77, 83].

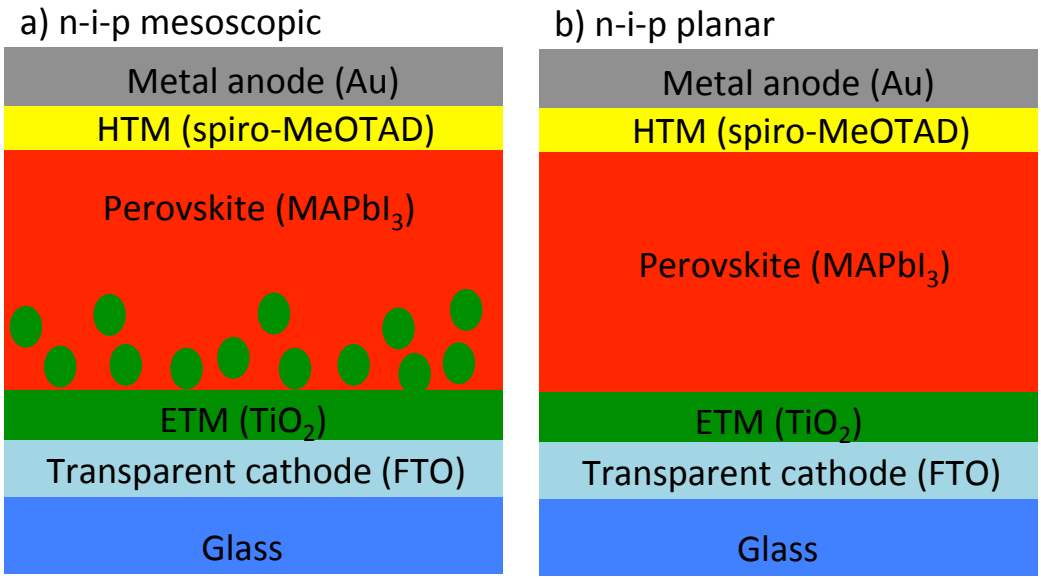

Figure 4.6: Schematic diagrams of perovskite solar cells in the a) n-i-p mesoscopic, b) n-i-p planar structures.

Since there is a significant amount of the material existing in amorphous and disordered phases [84], the open-circuit voltage (V_{OC}) and especially the short-circuit current density (J_{SC}) become relatively low [85]. To improve the device efficiency, the mesoporous layer needs to be thinner (150 to 200 nm) to enhance the crystallinity in the perovskite absorber. The thickness of mesoporous layer determines the pore filling fraction and morphology of the perovskites [86, 87]. The charge transport rates and collection efficiencies at the TiO_2 interface are dependent upon complete pore filling. Consequently, meso n-i-p structure became a very popular structure in the literature. $FAPbI_3$-based perovskite solar cells with power conversion efficiency exceeding 20% were fabricated using the mesoscopic structure [88].

The planar n-i-p structure is shown in Figure 4.6 b. To have high-efficiency

perovskite devices, mesoporous ETM was thought to be critical due to more efficient hole extraction at HTM interfaces than electron extraction at ETM interfaces [89]. However, if the formation of the perovskite absorber, the interfaces, carrier transport layers, and electrodes are well-controlled, there is no need to use a mesoporous layer to have high efficiencies [90]. With the optimization of the electron selective indium tin oxide (ITO)/TiO_2 interfaces, a 19.3% efficiency was achieved in n-i-p device [90]. V_{OC} and J_{SC} are enhanced in the planar n-i-p perovskite solar cell when compared with the mesoscopic device, but the planar device often suffers from severe J-V hysteresis. J-V hysteresis is observed when the direction and the rate of the voltage sweep are varied, and it is one of the major problems that sets back the device performance.

4.2.2 Inverted p-i-n Structure

In the inverted p-i-n structure, the HTM layer is deposited first and the order of the deposition is changed relative to the n-i-p structure. As shown in Figure 4.7 a the device structure consists of p-type conducting polymer (50-80 nm thick poly(3,4-ethylenedioxythiophene) poly(styrene-sulfonate) (PEDOT:PSS) spin-coated onto ITO-coated substrates. The next layers are as follows: perovskite thin film (300 nm), an organic hole blocking layer (10-60 nm thick [6,6]-phenyl C_{61}-butyric acid methyl ester (PCBM)) and a metal cathode layer (Al of Au). Mixed halide perovskite films were fabricated by using multi-cycle interdiffusion method in the planar p-i-n structure with 18.9% efficiency [91].

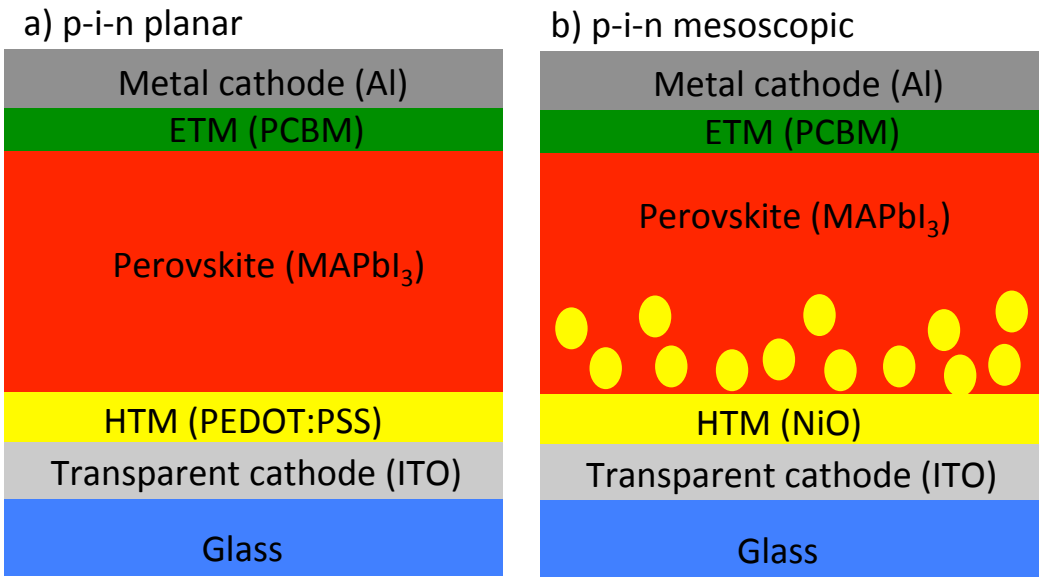

Figure 4.7: Schematic diagrams of perovskite solar cells in the a) p-i-n planar, b) p-i-n mesoscopic structures.

There have been further developments of the p-i-n device structure using different options for the contact from organic to inorganic materials. For example, ZnO/TiO_2 was used as the electron selective contact and NiO was used as the hole selective contact [92, 93]. NiMgLiO and $TiNbO_2$ have been used as inorganic charge extraction layers to fabricate 1 cm^2 and 15% efficient perovskite cells [92]. The construction of the mesoscopic p-i-n device structure became easier with the use of oxide hole transport materials (Figure 4.7 b) such as nanostructured NiO films [94].

4.3 Preparation Methods

It is known that the device performance depends to a large degree on the quality of the active material. The quality of the perovskite film can be achieved by

controlling crystallinity, morphology, uniformity, and phase purity. There are several critical issues that affect the quality and the crystallization of the film, such as the preparation processes, deposition technique, and processing conditions of the perovskite films. The preparation processes that have been studied in this chapter can be listed as follows: single-step solution deposition [78], two-step solution deposition [95], solution-assisted vapor deposition [96], and thermal vapor deposition [97]. Deposition methods for perovskite thin films are given in Figure 4.8.

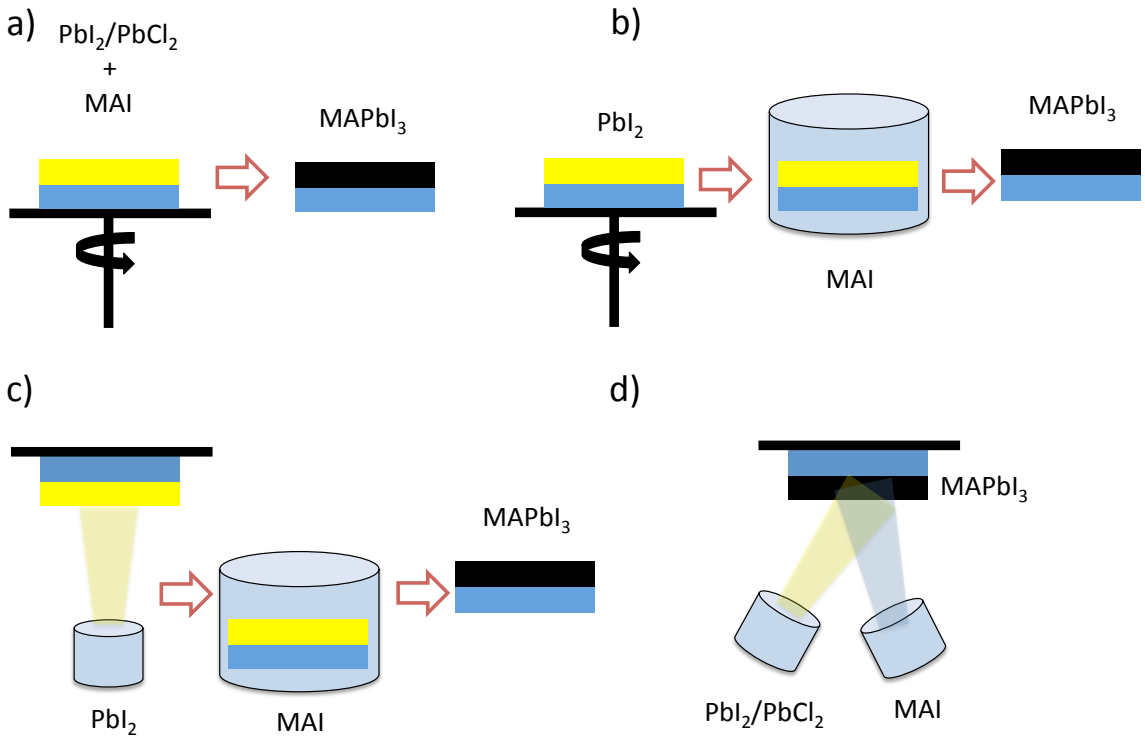

Figure 4.8: Deposition methods for perovskite thin films , including a) single-step solution deposition, b) two-step solution deposition, c) two-step hybrid deposition, and d) thermal vapor deposition.

4.3.1 Substrate Preparation

We started with glass substrates pre-coated with an ITO layer of 40 nm purchased from Delta Technologies. These, along with the glass substrates were cleaned in an ultrasonic bath with acetone, detergent, deionized water, and isopropanol followed by oxygen plasma cleaning. The conducting polymer poly(3,4-ethylenedioxythiophene)-poly(styrenesulfonate) (PEDOT:PSS), purchased from Ossila Ltd., and was spin coated at 4000 revolutions per minute (rpm) for 30 s on top of the ITO to provide an efficient hole injecting electrode. After spin coating the PEDOT:PSS layer the films were annealed on a hot plate at 120°C for 1 hour.

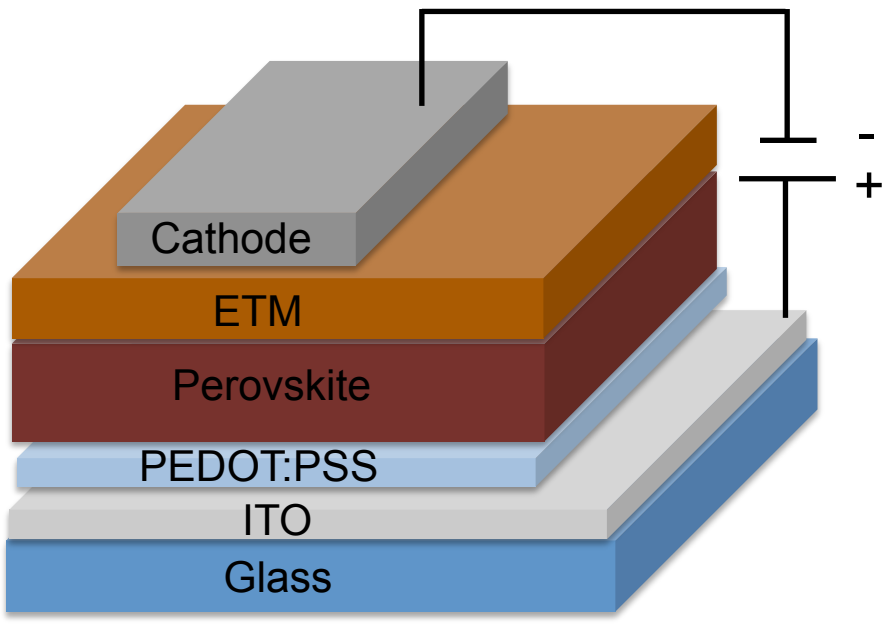

Figure 4.9: Simple device structure of a complete perovskite solar cell.

We used these coated substrates to prepare the perovskite films and perovskite solar cells with different deposition techniques, such as single-step and two- step solution deposition, and solution-assisted vapor deposition. Our basic device structure is shown in Figure 4.9.

4.3.2 Single-Step Solution Deposition

It is common to use single-step deposition [Figure 4.8 a)] for the ease of production and low fabrication cost. To prepare the precursor solution organic halides and lead halides are dissolved in gamma-butyrolactone (GBL), dimethylformamide (DMF), or dimethyl sulfoxide (DMSO). Organic halides are organic compounds and they contain a halogen atom bonded to a carbon atom. Common organic halides are methylammonium (MA, $CH_3NH_3^+$) iodide or formamidinium [FA = $CH(NH_2)_2$, CH_3NH_3] iodide, and lead halides are in the form of PBX_2, X=I, Br, or Cl.

It is known that perovskites can tolerate different composition rates of organic and inorganic materials [98]. Other groups fabricated high-efficiency devices using different ratios of MAI and PbI_2 to make MAI-poor (1:2) [99] or MAI-rich (3:1) [90] precursors. However, crystallinity, phase, and morphology of the films critically depend on the processing temperatures and times [87, 98, 100]. Other parameters that can affect the device performance can be listed as: oxygen and humidity levels, substrate material, and deposition techniques. In 2014, 9.7% efficient perovskite device in the form of the first solid-state device was prepared by using the single-step solution process [101].

We used precursor ink I101 $CH_3NH_3PbI_{3-x}Cl_x$ (a mixture of methyl ammonium iodide (MAI) and lead chloride (PbCl) dissolved in dimethyl formamide (DMF)) purchased from Ossila Ltd. and spin-coated the ink directly onto the PEDOT:PSS coated substrates. The ink is kept at 70^{o}C for 1-hour before spin-coating while the PEDOT:PSS coated films are kept at 90^{o}C. Different spin rates correspond to different thicknesses of perovskite films. The thickness of the perovskite layer spin-coated at the rate of 3000 r.p.m. was measured to be 150 nm. The spin coating is followed by annealing at 90^{o}C for 1-hour.

Figure 4.10 shows an SEM image of a film made with single-step solution deposition, and shows that the film has large pin holes. For a successful device fabrication we need to have pin-hole free films because otherwise after deposition of the top electrode shortcircuits will occur with the bottom electrode.

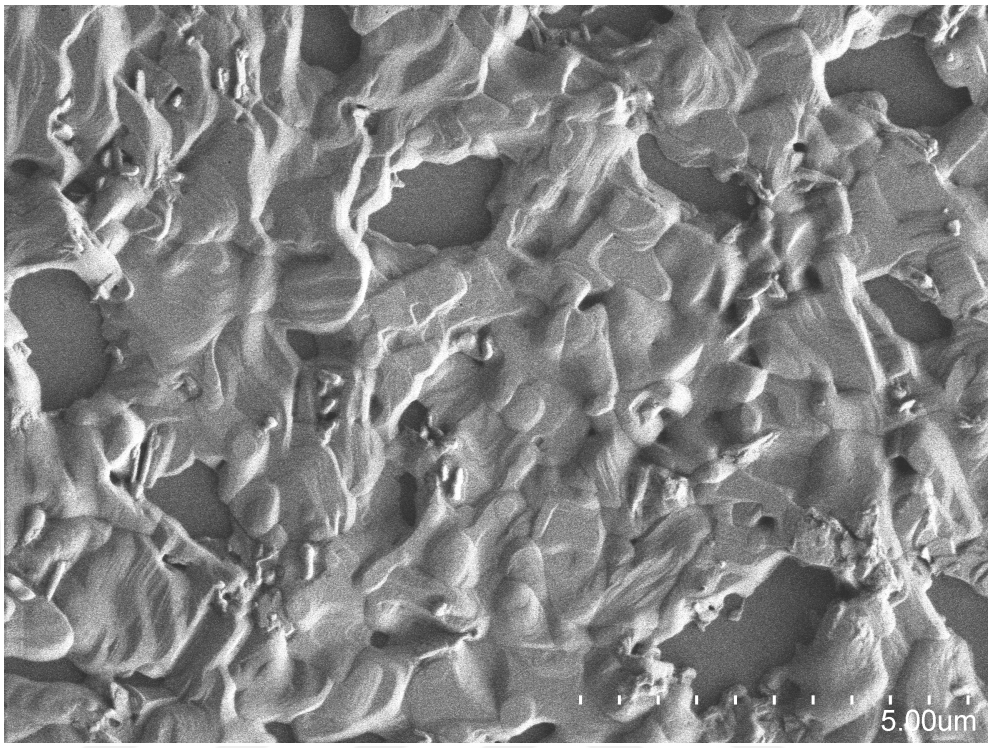

Figure 4.10: SEM image of one-step solution processed perovskite film.

We tried to improve the film morphology by drop casting several solvents (e.g. chlorobenzene, toluene) on the perovskite layer. This process is called solvent engineering. Adding an antisolvent, which should not dissolve the perovskite films, just before spin process of the perovskite is completed, can result in extremely uniform and dense perovskite films [102]. It is found that the introduction of antisolvent extracts DMF from the precursor solution, and this can change the grain growth of the perovskite. There have been other antisolvents that were used to fabricate highly uniform perovskite films [103], such as diethhyl ether [104], benzene, and xylene.

In addition to antisolvents, we tried to change the spin rate of the perovskite

ink to optimize the surface coverage of the perovskite, and to find the best spin rate for our devices. The absorption spectrum of four different spin rates is given in Figure 4.11. All absorption spectrum data throughout this chapter have the units of optical density (OD) which is related to the transmittance. The relationship between transmittance and OD is given as: $T = 10^{-OD}$.

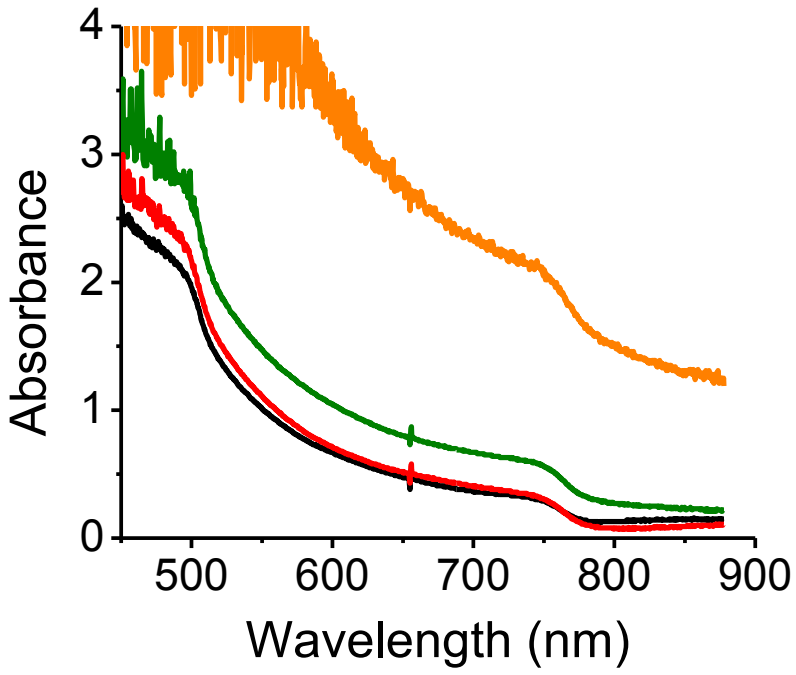

Figure 4.11: Absorption spectrum of perovskite films fabricated using one-step solution deposition at different spin rates : 750 rpm (orange), 1500 rpm (green), 3000 rpm (red), 6000 rpm (black). The units for absorbance and wavelength data are optical density (OD) and nanometer, respectively.

It was observed that the films fabricated at a spin rate of 750 rpm were very thick (240 nm) and highly nonuniform. The thickness measurement of perovskite films versus spin rate is given in Table 4.1.

Table 4.1: Thickness measurement of different spin rates for perovskite films fabricated using single-step solution deposition.

Spin rate (rpm)	Perovskite layer thickness (nm)
750	240
1500	195
3000	170
6000	120

We could not achieve a working solar cell even after optimizing the films that were fabricated using single-step solution technique. As a result, we decided to try another deposition technique to prepare the perovskite layer, which is two-step solution deposition.

4.3.3 Two-Step Solution Deposition

The two-step solution deposition technique was first introduced by Mitzi et al. in 1998 [105]. They demonstrated a two-step dipping technique that can be considered a hybrid between solution and vacuum deposition techniques. Gratzel et al. used a sequential deposition method to fabricate perovskite solar cells by first depositing PbI_2 from solution into a nanoporous titanium dioxide film [95]. Perovskite film is created by exposing this film to a solution of MAI (CH_3NH_3I), and a power conversion efficiency of approximately 15% was achieved. MAI can be deposited onto PbI_2 film by either spin-coating [101] or dipping [95]. When one-step solution process and two-step sequential deposition processes are compared, more uniform and denser perovskite films were observed using the latter technique [98]. This technique has been

used by many other groups and high-efficiency devices were fabricated [88,95,102,106].

High-quality perovskite films can be fabricated by using the two-step solution method. There are two parameters we changed and evaluated the resulting films' absorption spectrum as well as SEM images. It is found that varying MAI solution concentration changes the perovskite grain size [101].

We first prepared 1 M solution of PbI_2 (Sigma Aldrich) in DMF (460 mg of PbI_2 in 1 ml DMF) and kept it overnight stirring at 70^oC. During the spin-coating procedure the lead solution was kept at 70^oC while the PEDOT:PSS coated ITO films were at 90^oC. PbI_2 solution was spin coated at 2000 rpm for 30 s. Then the lead iodide films was placed on a hot plate at 70^oC for a few minutes to get rid of the DMF solvent. PbI_2 films were then dipped into MAI (Sigma Aldrich) solution of different concentrations inside a Petri dish (10 mg, 20 mg, 30 mg, 40 mg, and 50 mg in 1 ml isopropanol) for only one minute. For the two-step solution method PbI_2 films were kept in air while they were in MAI solution [Figure 4.8 b)]. However, we had to keep the Petri dish on the hot plate to fully convert the thermally evaporated PbI_2 films into perovskite films. This will be explained in the next section.

SEM images of the perovskite films fabricated with different five different concentration of MAI are given in Figure 4.12.

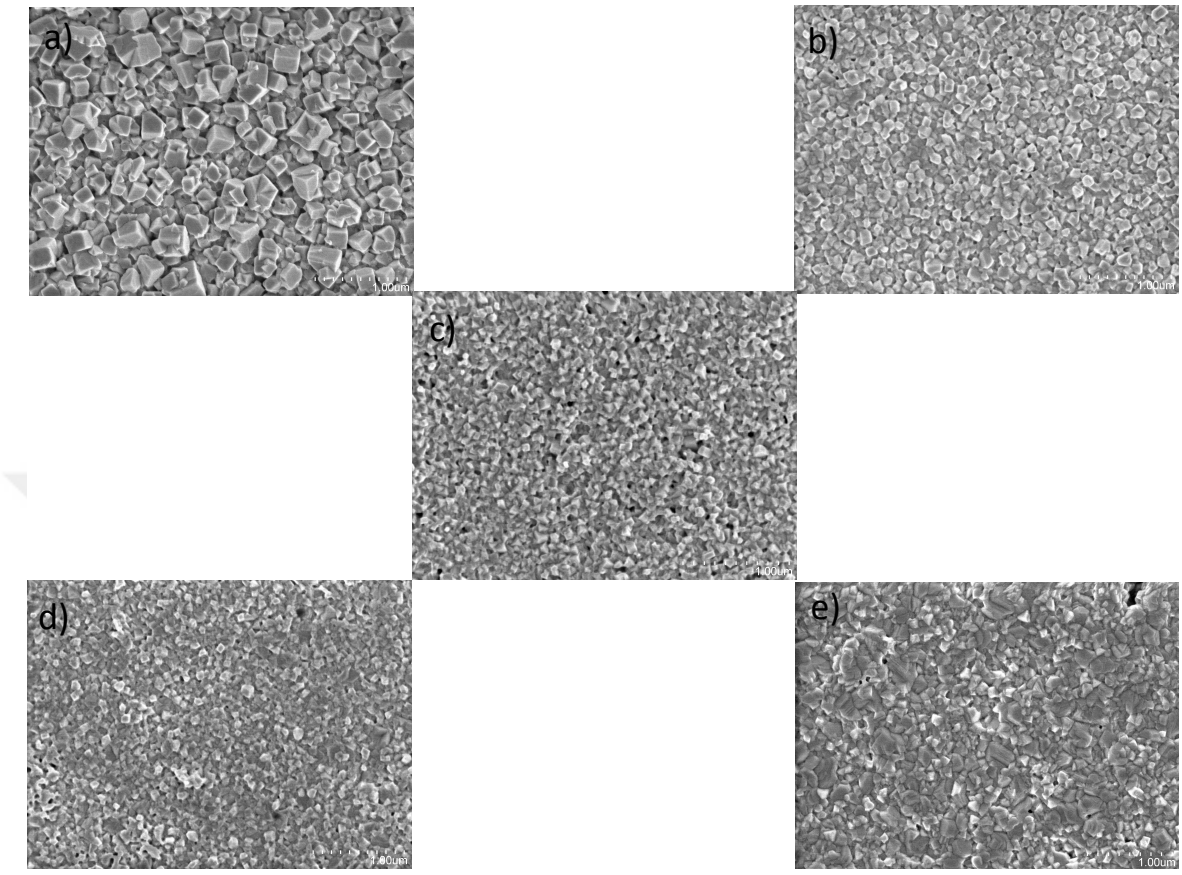

Figure 4.12: SEM images of films made with five different concentration of MAI in two step process ; a) 10mg/ml, b) 20mg/ml, c) 30mg/ml, d) 40mg/ml, e) 50mg/ml.

These SEM images clearly show that the perovskite grain size varies as the concentration of the MAI solution differs. Compared with films made from 50mg/ml MAI solution, films made from 10 mg/ml MAI solution show larger perovskite grain size. There is a trade-off between perovskite grain size and surface smoothness, and this is one the major drawbacks of the two-step solution deposition method [101]. Larger perovskite grains result in poor surface coverage, and this limits the device performance. Figure 4.13 shows the absorption spectrum of these films.

We also tried to vary the spin rate for the PbI_2 deposition. The results of the thickness measurements of perovskite films versus spin rate of PbI_2 is given in Table 4.2.

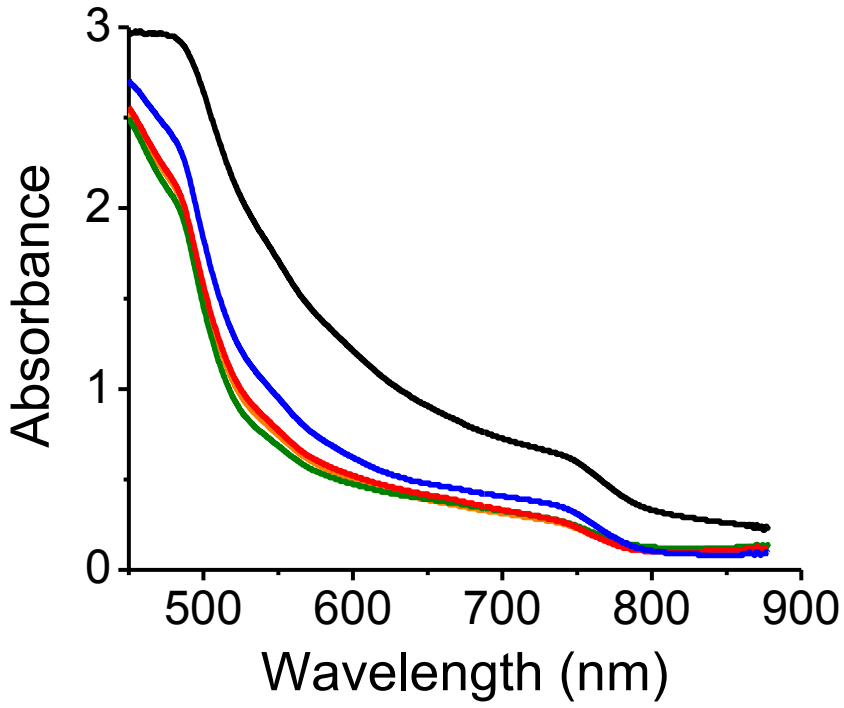

Figure 4.13: Absorption spectrum of perovskite films made with different MAI solution concentration : 10 mg/ml (black), 20 mg/ml (orange), 30mg/ml (green), 40 mg/ml (red), 50 mg/ml (blue).

Another drawback of this method is that the conversion of PbI_2 to $MAPbI_3$ is incomplete because of the capping layer formed on the surface of PbI_2. Since the heavy metal halide layer easily interacts with small molecules, this forms the capping layer when the PbI_2 films are dipped into the MAI solution [107]. This capping layer prevents MAI diffusion to the underlying layer, and it results in incompletely

Table 4.2: Thickness measurement of different spin rates for perovskite films fabricated using two-step solution deposition.

Spin rate (rpm)	Perovskite layer thickness (nm)
1000	200
1500	195
2000	180
2500	176
3000	170

converted perovskite films. The absorption spectrum of perovskite films made with different thickness of the PbI_2 layer is given in Figure 4.14.

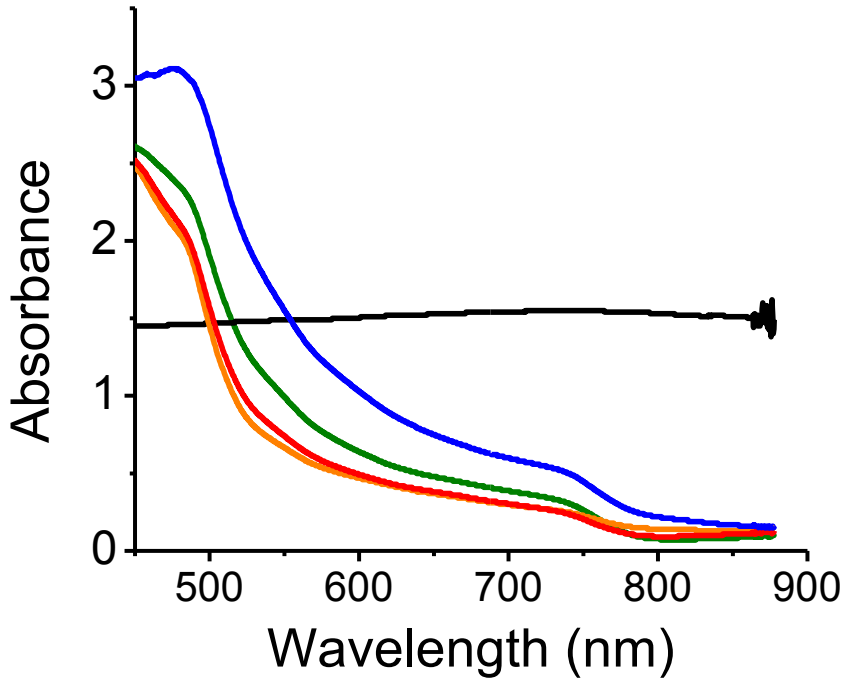

Figure 4.14: Absorption spectrum of perovskite films prepared at different thickness of PbI_2 layer : a) 1000 rpm(black), b) 1500 rpm (blue), c) 2000 rpm (red), d) 2500 rpm (green), e) 3000 rpm (orange).

The experimental procedure is the same as that previously described for films made from different MAI concentrations. Here, five different spin rates were used to spin coat the PbI_2 films: 1000 rpm, 1500 rpm, 2000 rpm, 2500 rpm, and 3000 rpm. Then the lead iodide films were annealed at 70^{o}C for a few minutes. PbI_2 films were then dipped into the MAI (Sigma Aldrich) solution inside a Petri dish (30mg in 1 ml isopropanol) for only one minute. SEM images of perovskite films at different thicknesses are shown in Figure 4.15.

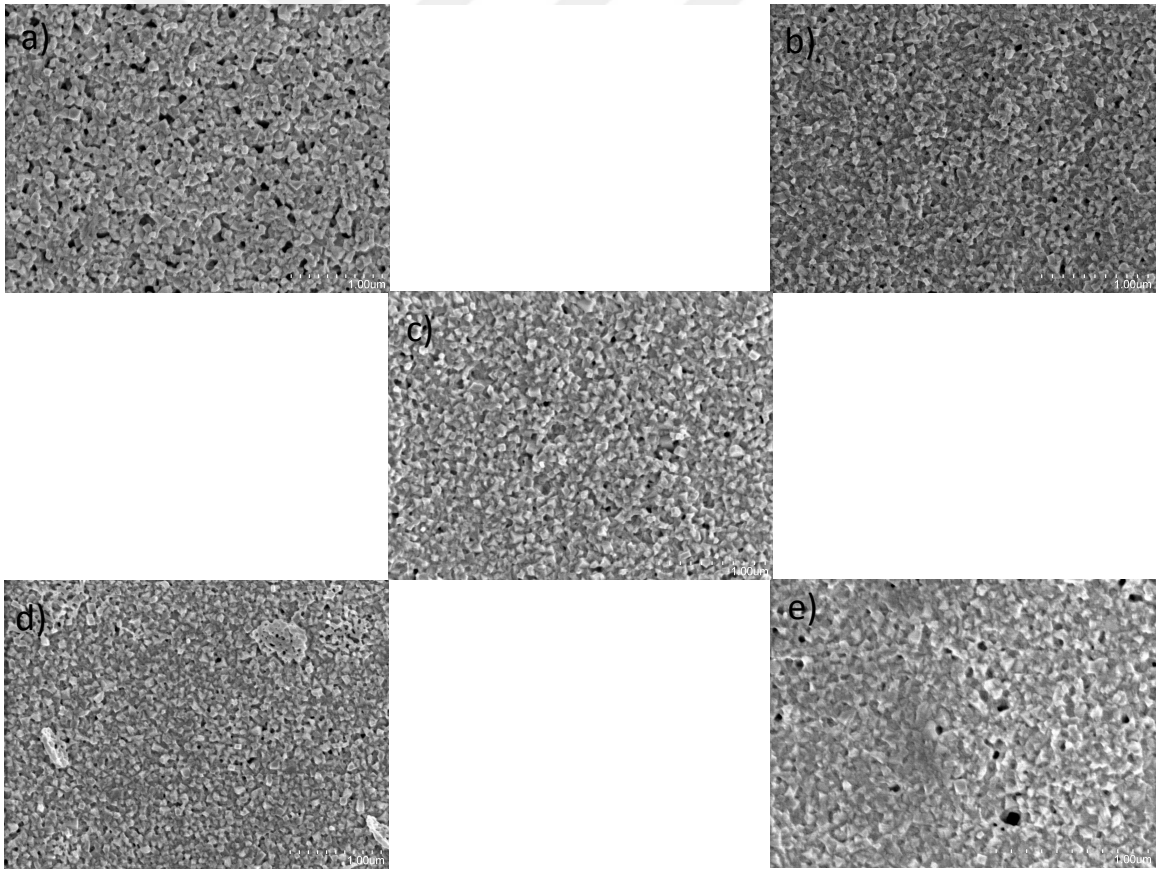

Figure 4.15: SEM images of films made with five different thickness of PbI_2 in two-step solution process ; a) 1000 rpm, b) 1500 rpm, c) 2000 rpm, d) 2500 rpm, e) 3000 rpm.

There have been some relatively recent techniques to overcome the issues we described, and up to 20.2% cell efficiency was achieved by using two-step solution method [88].

We fabricated perovskite solar cells using the two-step solution deposition method. PCBM solution was prepared by dissolving Phenyl-C61-butyric acid methyl ester (PCBM, 1 g, Nano-C) into chlorobenzene with a concentration of 20 mg/mL, and stirring in a glove box overnight. Then, the solution was purified by a 300 nm filter to remove any contaminating particles from the PCBM solution. PCBM solution was spin-coated onto the perovskite films (180 nm perovskite using 50 mg/mL MAI solution) at 1000 rpm for 30 s (results in thickness of 90 nm), then the films were left under high vacuum at 10^{-7} mbar overnight. The PCBM layer acts as the electron trnasportineg layer of the solar cell. The top electrode was deposited using thermal evaporation of Ca (50 nm)/ Al (100 nm) to complete the devices. The active device area was 0.1 cm^2. The structure of the solar cell is shown in Figure 4.16.

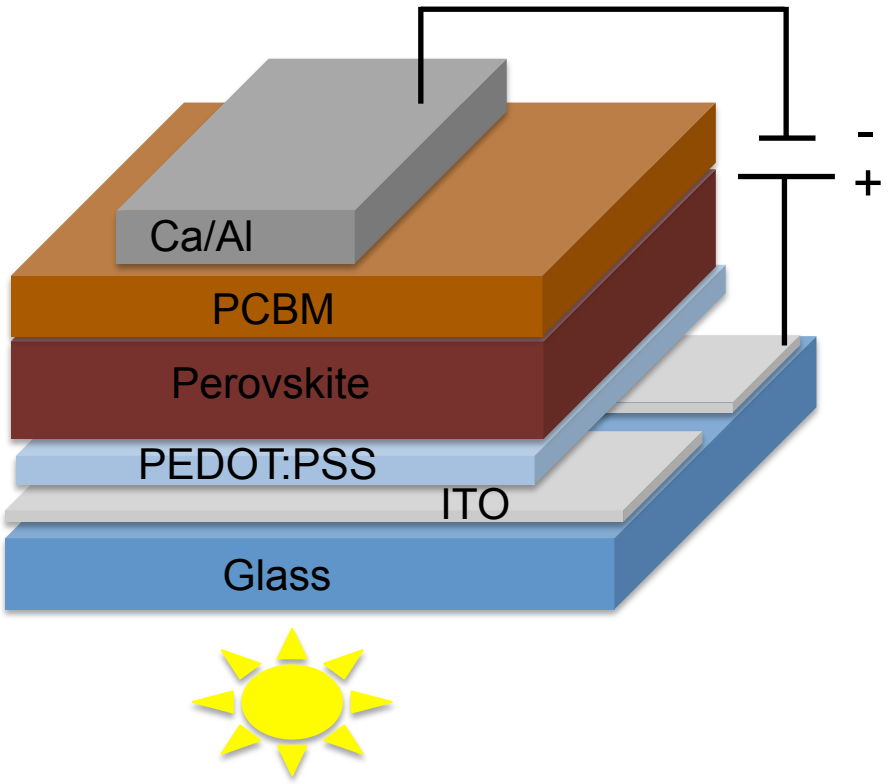

Figure 4.16: Device structure of perovskite solar cell prepared using two-step solution deposition method.

The solar cells were tested by using a PV Measurements solar simulator, and the current density versus voltage is shown in Figure 4.17 (right). The absorption spectrum of the PbI_2 film and the perovskite film for this cell is shown in Figure 4.17 (left). The power conversion efficiency was 7.21% with 0.94 V of V_{OC} and 44.6% of fill factor.

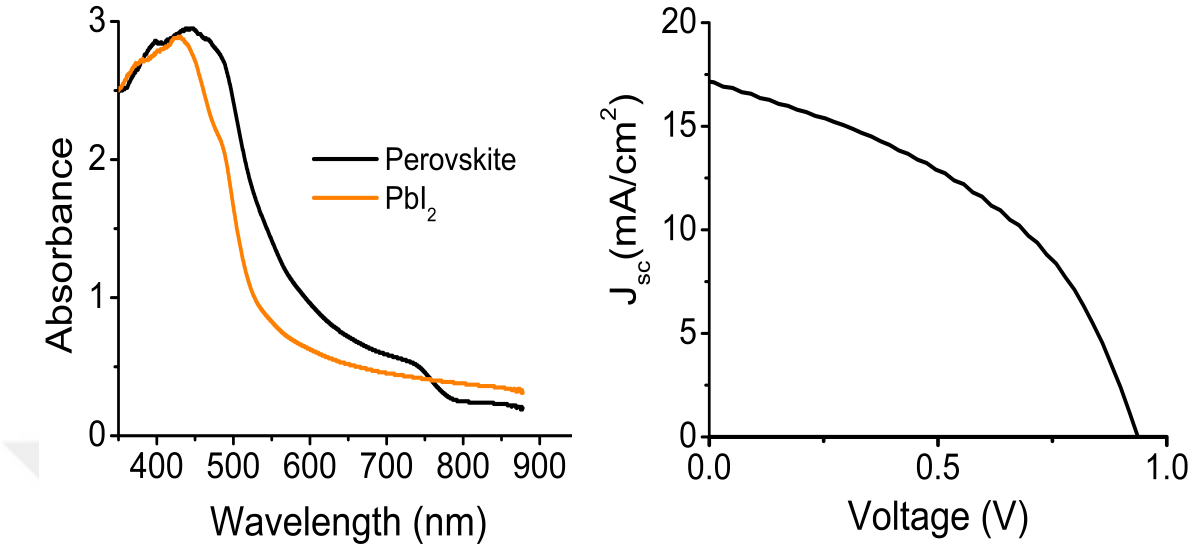

Figure 4.17: Absorption spectrum of spin-coated lead (II) iodide and perovskite films (left). Current density vs. voltage curve of the solar cell made with this film (right).

We fabricated another set of devices using the same technique described above except we varied the MAI concentration from 50mg/mL to 30 mg/mL. There were four working devices on one substrate, and the best efficiency achieved on this device was 6%. All other parameters of all the cells are given in Table 4.3. The current density versus voltage is given in Figure 4.18 (left) and SEM image of the perovskite film for this device is given in Figure 4.18 (right).

Table 4.3: Summary of the parameters for a perovskite solar cell prepared using 30 mg/mL of MAI and 180 nm of perovskite layer in two-step solution deposition method.

Device	V_{OC} (V)	J_{SC}(mA/cm^2)	FF (%)	Efficiency (%)
1	0.934	13.67	46.93	6.0
2	0.916	8.19	41.16	3.09
3	1.0	9.08	41.95	3.81
4	0.94	12.41	42.06	4.9

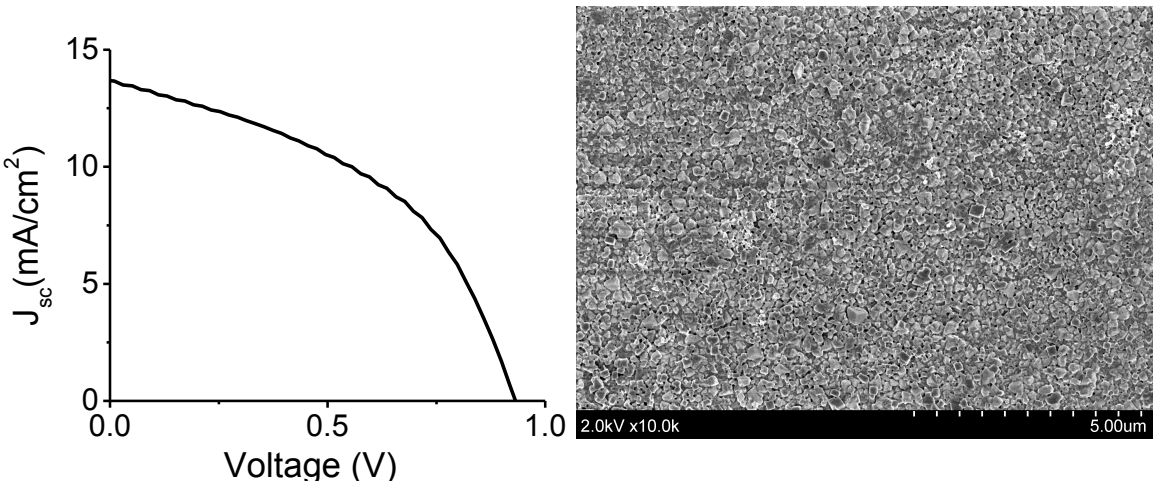

Figure 4.18: Current density vs. voltage curve of the solar cell made using 30 mg/mL MAI and 180 nm perovskite layer (left). SEM image of the perovskite layer of this device (right).

4.3.4 Solution-Assisted Vapor Deposition

We modified the two-step solution deposition method, and PbI_2 is introduced through a vapor deposition technique rather than through solution processing [Figure 4.8 c)]. Xi et al. used this technique to fabricate perovskite solar cells and achieve

11.77% power conversion efficiency. [96]. Chen et al. first spin coated PbI_2, then they vapor-deposited MAI on top of PbI_2 to fabricate perovskite films [108]. This deposition method allows us to prepare perovskite films with better control of morphology, grain size and film conversion. The devices prepared by this method showed 10 to 12% power conversion efficiency [108, 109]. We compared the images of PbI_2 and perovskite films prepared using two-step solution deposition and solution-assisted vapor deposition methods in Figure 4.19. Films made with vapor deposition were more uniform than those made by solution deposition. We also compared the SEM images of the films made using both methods in Figure 4.20.

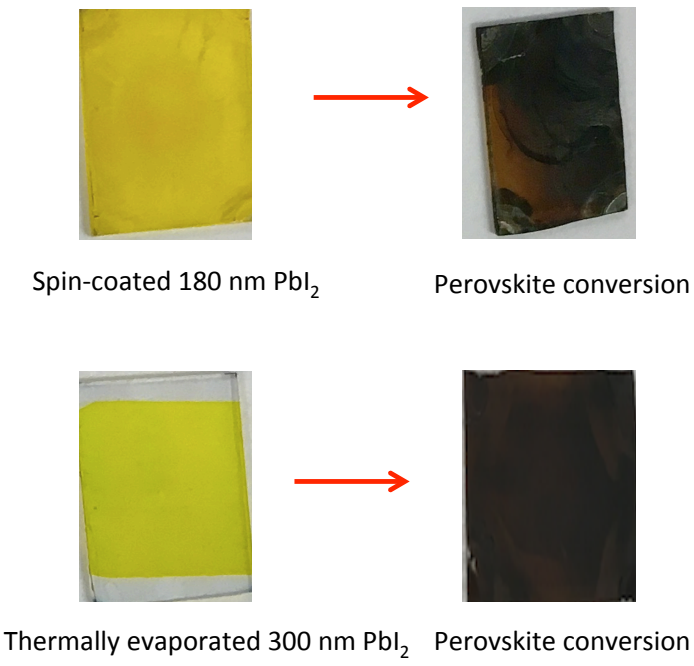

Figure 4.19: PbI_2 and perovskite films prepared using two-step solution deposition and solution-assisted vapor deposition methods.

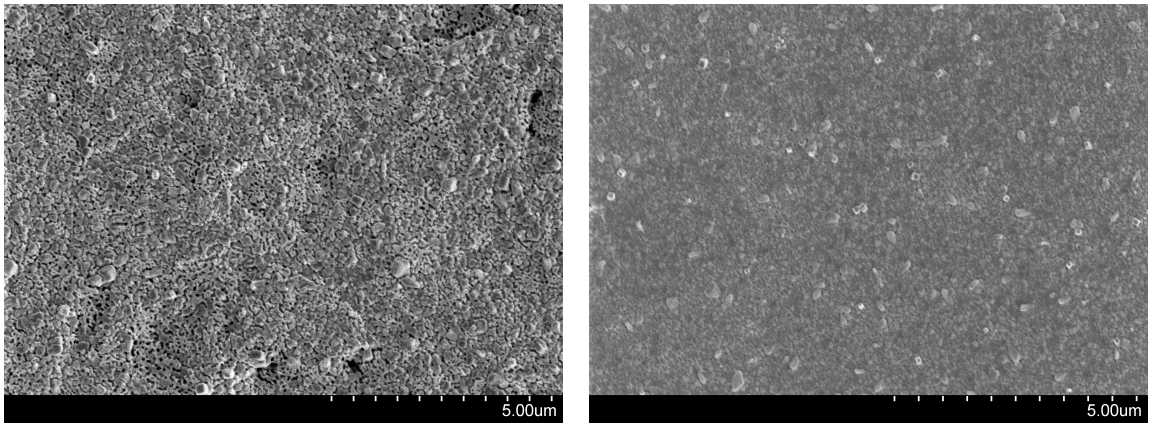

Figure 4.20: SEM images of perovskite films prepared using two-step solution deposition (left) and solution-assisted vapor deposition (right) methods.

PEDOT:PSS coated ITO substrates were transferred to the evaporation chamber to thermally evaporate the PbI_2 material. The evaporation rate was 0.1 nm/s. After reached the desired thickness for the PbI_2 layer, the films were taken to the ambient air for the perovskite conversion. First, the films were kept on the hot plate at 80^oC for 2 minutes, then they were dipped into MAI solution kept on the hot plate at 80^oC for 1 minute. The perovskite film was formed and the films were annealed at 90^oC for at least 1 hour. Figure 4.21 shows the absorption spectrum for two different thicknesses of the thermally evaporated PbI_2 and perovskite films. PCBM solution with a concentration of 20 mg/mL in chlorobenzene was spin-coated onto perovskite films at 1000 rpm for 30 s (resulting 90 nm thickness), then the films were left under high vacuum at 10^{-7} mbar overnight. Fabricating the top electrode using thermal evaporation of Ca (50 nm)/ Al (100 nm) resulted in the completed devices.

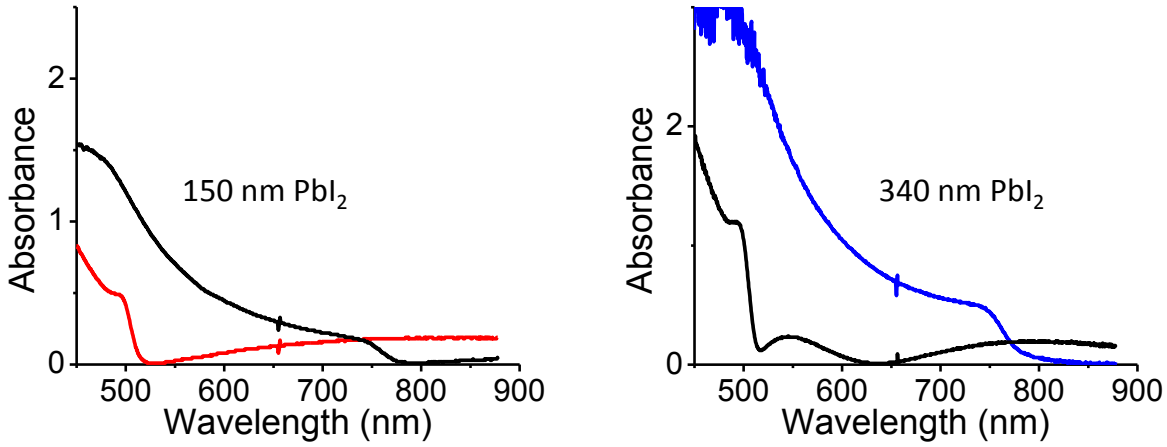

Figure 4.21: Absorption spectrum for PbI_2 and perovskite films at two different thicknesses (left-150 nm and right-340 nm).

Current-voltage characteristics and absorption spectrum of 150 nm thick perovskite films made from three different MAI solution concentrations (30 mg/mL, 40 mg/mL and 50 mg/mL) are shown in Figure 4.22. The power conversion efficiency of these devices were smaller than 0.2%. We observed decomposition of top electrode as the device were taken out to the air. Since perovskite is soluble in water the humidity level of the environment greatly affected our cells.

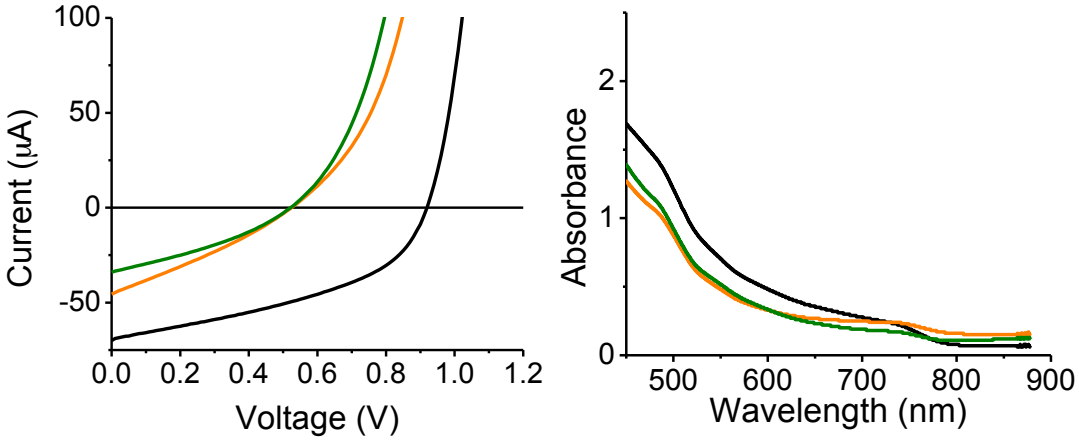

Figure 4.22: Current-voltage (left) and absorption spectrum (right) of 150 nm thick perovskite films made with three different MAI solution concentration : 30 mg/mL (orange), 40 mg/mL (green) and 50 mg/mL (black).

To evaluate how the morphology changes if we use different MAI solution concentrations (10 mg/mL, 30 mg/mL, 50 mg/mL) to prepare perovskite films, SEM images of these films are shown in Figure 4.23.

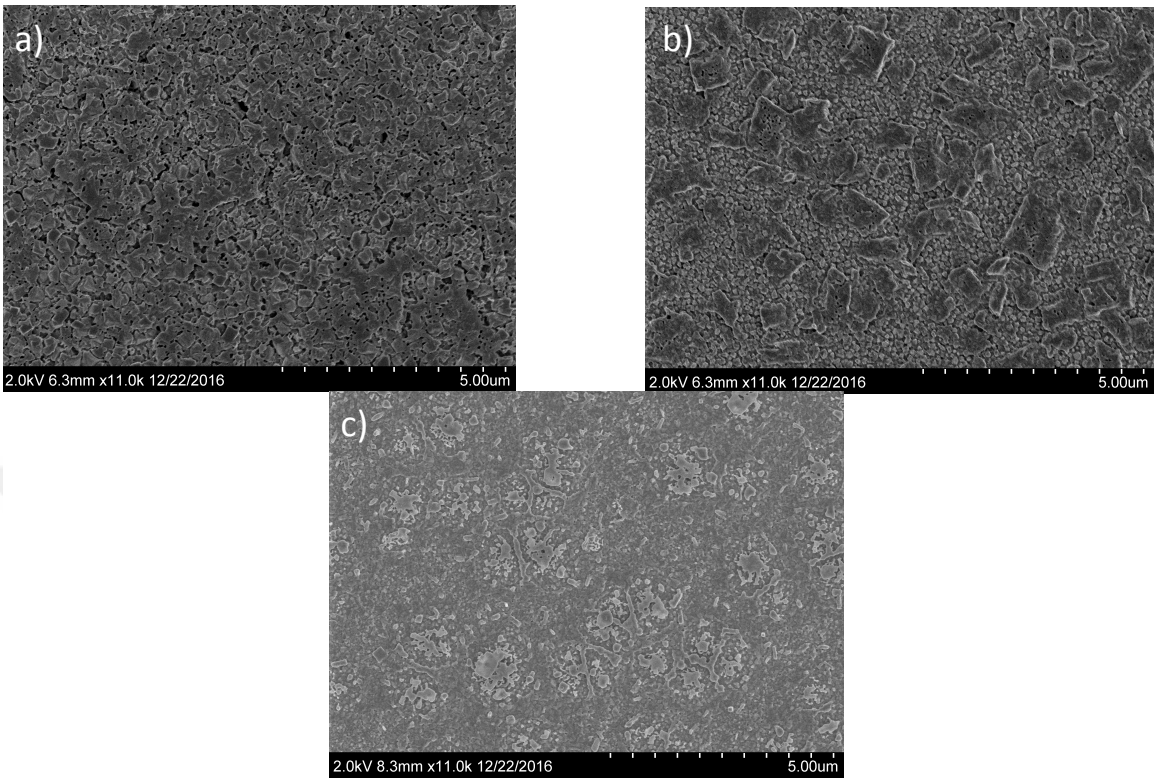

Figure 4.23: SEM images of 150 nm perovskite films prepared with different MAI solution concentration : a) 10 mg/mL, b) 30 mg/mL, and c) 50 mg/mL.

4.3.5 Thermal Vapor Deposition

High-quality semiconductor thin films with better control of thickness and composition have been fabricated using thermal vapor deposition. Mitzi et al. demonstrated the first thermal vapor-deposited perovskite thin films in 1999 [110]. The first planar heterojunction $MAPbI_{3-x}Cl_x$ perovskite solar cell using a dual-source thermal evaporation [Figure 4.8 d)] was fabricated with 15% efficiency [97]. There are other vapor-based deposition techniques used to fabricate perovskite solar cells such as chemical vapor deposition [111] and layer-by-layer vacuum sublimation [112].

Highly uniform and pin-hole free perovskite films were prepared using thermal vapor deposition. Better surface coverage can be achieved by this technique compared to solution processing [97,113,114]. However, the temperature of the deposition needs be controlled very carefully since the precursor sources and products have low thermal stability. High-efficiency devices made using this method were reported by a few groups [97, 112–115].

4.4 Advanced Device Engineering

Optoelectronic properties of the perovskite films and the device performance have been improved with the advancement of several device engineering strategies [95, 108, 116–118]. Some of these strategies can be listed as: modifying precursor solution [95, 119, 120], processing condition [102, 121], interface properties [122, 123] and perovskite composition [92, 124]. The main goal for device engineering is to have uniform and pin-hole free perovskite films with good crystallinity.

4.4.1 Process Engineering

It has been demonstarated that adding an antisolvent that does not dissolve perovskite films during the spin process can result in highly uniform and dense perovskite films [102]. The role of the antisolvent in this process is that it extracts the DMF from the precursor solution, and this makes a denser, more uniform, and smaller grain sized perovskite films. There are other solvents used to form highly uniform perovskite films, such as diethyl ether [104], xylene, benzene, and chlorobenzene [103]. We also used toluene, chlorobenzene, and chloroform onto perovskite films

and measured the absorption spectrum (Figure 4.24) of these films.

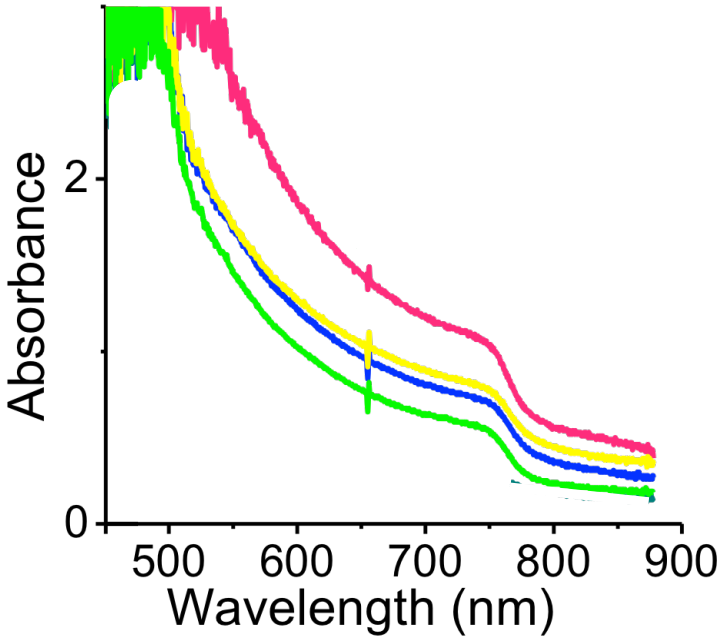

Figure 4.24: Absorption spectrum of toluene (pink), chlorobenzene (blue), and chloroform (yellow) added perovskite films compared with regular perovskite films (green).

Increase of the grain size and control of the crystallinity can be achieved with thermal annealing of the perovskite films. However, it can also decompose the film and reduce the surface coverage [87, 98]. High-efficiency devices were fabricated by controlling the solvent annealing process, resulting in improved electronic properties and crystallinity of the perovskite films [125–128].

We fabricated perovskite films using the two-step solution deposition method with (at 74^{o}C for 2 minutes) and without annealing of the PbI_2 films. We investigated how this would affect the absorption spectrum of the perovskite films (Figure 4.25).

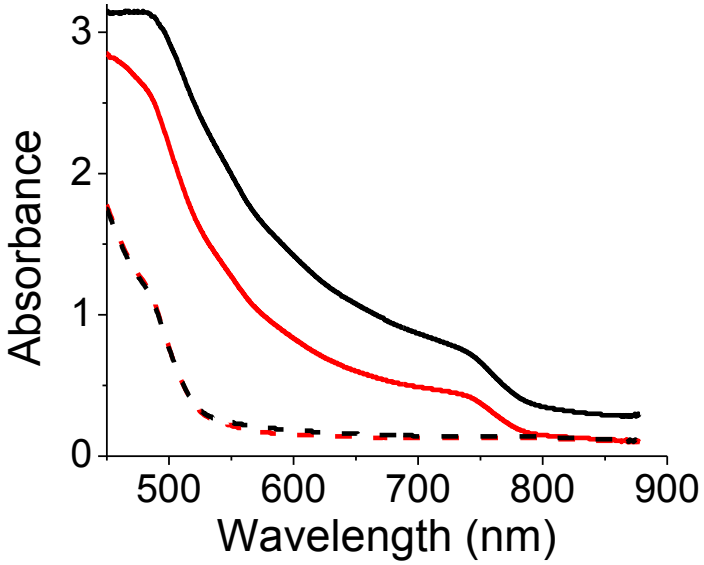

Figure 4.25: Absorption spectrum of perovskite films made with (red) and without (black) annealing of the PbI_2 films. Solid lines represent perovskite films, and dashed lines represent PbI_2 films.

As is well-known, high efficiency and good reproducibility of the cell performance depend on the crystalline morphology of the perovskite films [129, 130]. Herein, we used two-step solution deposition method to spin coat a mixture of $Pb(SCN)_2$ and PbI_2 solution for the first layer, followed by MAI deposition to form $CH_3NH_3PbI_{3-x}(SCN)_x$ perovskite film. Thiocyanic (SCN) is a stable pseudohalogen, it has similar ionic radii to I^-. The SCN group in the dye structure improves the optical absorption and charge transport [131]. Compared to CH_3NH_3I we can achieve larger-sized crystals and fewer traps with the addition of $Pb(SCN)_2$ [92]. The absorption spectrum of the perovskite films with and without $Pb(SCN)_2$ additive is shown in Figure 4.26.

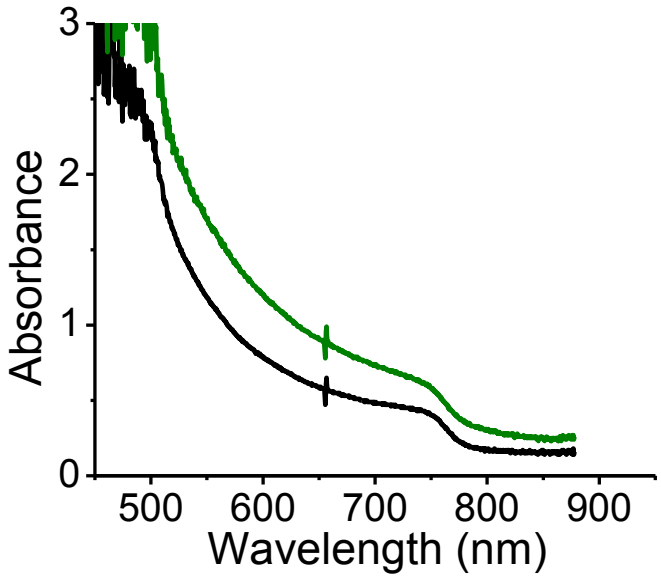

Figure 4.26: Absorption spectrum of perovskite films made with (black) land without (green) $Pb(SCN)_2$ additive.

4.4.2 Contact Engineering

It has been shown that efficient charge separation and collection occur at the interfaces between the perovskite and charge-selective layers [122]. This was revealed by electron-beam-induced current investigations. The electron and hole collecting electrodes and their interfaces are critical to achieve highly charge selectivity and low surface recombination. A summary of commonly used cathode, ETM, absorber, HTM and anode materials is given in Table 4.4.

C_{60} layer is used as a selective electron extraction layer in solar cells [142]. Compared to PCBM , which is usually at a thickness of around 100 nm [143], C_{60} conducts electrons better [140]. We thermally evaporated C_{60} directly onto either onto perovskite to act as an ETM layer, and we finished the devices with thermal

Table 4.4: Commonly used cathode, n-type (ETM), absorber, p-type (HTM), and anode materials.

Anode	HTM	Absorber	ETM	Cathode
ITO	P3HT	$MAIPbBr_3$	PCBM	Al
C	PTAA [88]	$MAISnI_3$	ZnO [132]	FTO
Ag	PEDOT:PSS	$MAIPbI_3$	CdS [133]	AZO
Au	Spiro-MeOTAD	$FAPbI_3$ TiO_2	CdSe [134]	
	CuI [135]		SnO_2 [136, 137]	
	CuSCN [138, 139]		C_{60} [140]	
	NiO [141]			

Table 4.5: Summary of the parameters for a perovskite solar cell prepared using 30 mg/mL of MAI and either with 180 nm of perovskite or 5% $Pb(SCN)_2$ added perovskite layers in two-step solution deposition method. All of the devices are built on ITO/PEDOT:PSS substrates with active device area of 0.5 cm^2. With PCBM, Ca/Al used as cathode. With C_{60} only Al used as cathode.

ETM	PCE(%)	FF(%)	V_{OC}(mV)	J_{SC}(mA/cm^2)
with additive/PCBM	0.12	27.0	211	2.09
PCBM	0.17	32.3	167	3.15
with additive/C_{60} (80 nm)	0.16	57.0	487	0.58
C_{60} (80 nm)	0.09	29.6	171	1.73
C_{60} (60 nm)	1.2	23.0	814	6.42
C_{60} (90 nm)	1.9	27.8	769	9.21

evaporation of the cathode (Al). The summary of the parameters of the devices we fabricated is given in Table 4.5.

4.5 Issues and Challenges

Although perovskite solar cells have demonstrated high efficiencies, the commercialization of perovskite solar cells is limited by crucial issues and challenges that

remaon. We can summarize these issues as device stability, the existence of J-V hysteresis, and environmental impact during manufacturing, testing and disposal phases.

4.5.1 Device Stability

Commercial solar cells are often stable for 30 years, so long-term stability is expected for perovskite-based solar cells. However, stability data of perovskite solar cells show a few hundred hours [77, 144, 145]. The decomposition of perovskite crystal happens upon exposure to light, elevated temperature, and humidity [146]. It has been reported that perovskite PV modules can be stable with appropriate composition and encapsulation methods. Some of these methods are employing a moisture resistant layer to prevent water ingress [144, 147–149], using glass sealing or laminate plastic films to encapsulate perovskite films [145], and incorparating (FA^+ and Br^-) ions into perovskite [150–152].

4.5.2 J-V Hysteresis

J-V hysteresis is observed when the direction and rate of voltage sweep is varied, and it is one of the major problems that sets back the device performance [153]. The efficiency measurements become inaccurate with the presence of J-V hysteresis [154]. When the origin of the J-V hysteresis was investigated, three reasons were proposed: ferro-electricity [155, 156], ion migration [157, 158] and unbalanced charge collection rates [159, 160].

4.5.3 Toxicity and Pollution

Since most of the perovskite solar cells are lead-based, this creates environmental concerns. The potential lead pollution from a 1-GW perovskite PV plant is very small compared to other lead emission sources [161]. Actually, perovskite solar cells may reduce the amount of lead contamination by using lead sources such as from used car batteries [162].

CHAPTER 5
CONCLUSION

In our first study reported here, we have shown that thermally activated delayed fluorescence (TADF)-based OLEDs are immensely sensitive to an applied magnetic field. This reveals that magnetic field effects (MFEs) are an important tool to investigate the spin-dependent exciplex physics in TADF materials. In addition, it has been observed that an applied magnetic field can increase the electoluminescence power efficiency, providing a possible avenue for future industrial application of our technique for use in efficient OLEDs. It has been found that devices that were fabricated using thermal evaporation for the top electrode deposition showed larger MFEs when compared with e-beam fabricated devices, but only after an electrical stress (device conditioning) was applied to the devices. E-beam evaporation of the top electrode exposes the organic layer to X-rays, which in turn causes the formation of traps. A comparison between the electrically stressed device with the e-beam fabricated device allows for a comparison in trap-formation efficiency of the two methods. TADF is a thermally activated process, and this should result in thermally activated behaviour of the MFEs as well. We could confirm this picture by measuring MFEs at different temperatures, and the largest effect was observed at room temperature. We extracted a value for the activation energy consistent with other TADF measurements.

In a second study, we measured MFEs in organic diodes of regioregular polythiophenes (RR-P3HT) made with various anode and cathode materials to determine the importance of bipolarons and electron-hole pairs for magnetoconductance (MC).

P3HT was chosen because we found that these devices exhibit an unusually rich spectrum of MFEs lineshapes. The analysis of the different lineshapes and the conditions under which they occur will lead to valuable insights into the underlying mechanism of MFEs. Near-unipolar, electron-only, devices (Mg/RR-P3HT/Ca) displayed negative MC at all voltages. This was attributed to the bipolaron mechanism which produces spin blocking and only requires a single type of charge carrier. Near-unipolar, hole-only, devices (Au/RR-P3HT/ITO) showed no MC due to the holes' high mobility which does not allow sufficient time for the spin precession needed for the efficient formation of bipolarons. Both a negative (low voltage) and positive (high voltage) MC were measured in bipolar devices. An analysis of the electroluminescence efficiency, η, versus voltage showed that at low voltages the device operated in a unipolar regime. Therefore, as in the electron-only devices, the negative MC could be attributed to the bipolaron mechanism. Above 4.0 V, where the device operates in a bipolar regime and a positive MC was measured, a sizable magnetic field effect on η was measured as well. Therefore, the positive MC was attributed to the electron-hole pair model, which primarily affects η and produces a corollary effect on conductance.

The third study is on hybrid organic-inorganic perovskite devices. We studied single-step solution, two-step solution and solution-assisted vapor deposition techniques to fabricate perovskite films and solar cells. We have fabricated perovskite films using the single-step solution method with different thicknesses and measured the absorption spectrum of these films. We have observed pin-holes on the surface of the films in SEM images of these films. The second deposition method, two-step

solution deposition, was used to fabricate perovskite films and solar cells to achieve pin-hole free perovskite layer. For films made using this method we measured the absorption spectrum and took SEM images of perovskite films for different PbI_2 layer thicknesses and different concentration of MAI solution. Grain size changes of perovskite crystal and surface morphology of the films were evaluated. As a result, we used 50 mg/mL and 30 mg/mL MAI solution concentrations to fabricate perovskite solar cells. 7.21% PCE with 50 mg/mL and 6.0% with 30 mg/mL MAI solutions were achieved. The third deposition technique, solution-assisted vapor deposition, was studied in order to achieve more uniform perovskite films with a better thickness control, and better surface coverage. When compared with the first two techniques, we can have more uniform films by using this technique. The absorption spectrum and SEM images for different thicknesses of the PbI_2 layer were evaluated. Even though the surface morphology and coverage were improved, PCE of perovskite solar cell made with this technique was around 0.2%. Because the films made with thermal evaporation were denser than solution deposited films, it is expected to have difficulties with perovskite conversion. In addition to varying the deposition technique to improve the cell performance, we also tried several well-known device engineering methods such as, solvent dripping, annealing of the PbI_2 layer, additives to the PbI_2 solution and using C_{60} instead of PCBM electron extraction layer. We noticed that we can use Al as the cathode contact when C_{60} is used.

REFERENCES

[1] Alan J Heeger, S Kivelson, JR Schrieffer, and W-P Su. Solitons in conducting polymers. *Reviews of Modern Physics*, 60(3):781, 1988.

[2] Jean Luc Bredas and G Bryan Street. Polarons, bipolarons, and solitons in conducting polymers. *Accounts of Chemical Research*, 18(10):309–315, 1985.

[3] D K Campbell and a R Bishop. Soliton Excitations in Polyacetylene and Relativistic Field Theory Models. *Nuclear Physics B*, 200:297, 1982.

[4] Lewis J. Rothberg and Andrew J. Lovinger. Status of and prospects for organic electroluminescence. *Journal of Materials Research*, 11(12):3174–3187, 1996.

[5] Kenichi Goushi, Kou Yoshida, Keigo Sato, and Chihaya Adachi. Organic light-emitting diodes employing efficient reverse intersystem crossing for triplet-to-singlet state conversion. *Nature Photonics*, 6(4):253–258, 2012.

[6] Hiroki Uoyama, Kenichi Goushi, Katsuyuki Shizu, Hiroko Nomura, and Chihaya Adachi. Highly efficient organic light-emitting diodes from delayed fluorescence. *Nature*, 492:234–238, 2012.

[7] M. N. Baibich, J. M. Broto, A. Fert, F. Nguyen Van Dau, F. Petroff, P. Etienne, G. Creuzet, A. Friederich, and J. Chazelas. Giant magnetoresistance of (001)fe/(001)cr magnetic superlattices. *Phys. Rev. Lett.*, 61:2472–2475, Nov 1988.

[8] P. Grünberg, R. Schreiber, Y. Pang, M. B. Brodsky, and H. Sowers. Layered magnetic structures: Evidence for antiferromagnetic coupling of fe layers across cr interlayers. *Phys. Rev. Lett.*, 57:2442–2445, Nov 1986.

[9] Michel Julliere. Tunneling between ferromagnetic films. *Physics letters A*, 54(3):225–226, 1975.

[10] Terunobu Miyazaki and N Tezuka. Giant magnetic tunneling effect in fe/al 2 o 3/fe junction. *Journal of Magnetism and Magnetic Materials*, 139(3):L231–L234, 1995.

[11] Jagadeesh Subbaiah Moodera, Lisa R Kinder, Terrilyn M Wong, and R Meservey. Large magnetoresistance at room temperature in ferromagnetic thin film tunnel junctions. *Physical Review Letters*, 74(16):3273, 1995.

[12] ZH Xiong, Di Wu, Z Valy Vardeny, and Jing Shi. Giant magnetoresistance in organic spin-valves. *Nature*, 427(6977):821–824, 2004.

[13] Albert H Davis and Konrad Bussmann. Large magnetic field effects in organic light emitting diodes based on tris(8-hydroxyquinoline aluminum)(Alq_3)/N, N'-Di(naphthalen-1-yl)-N,N' diphenyl-benzidine (NPB) bilayers. *Journal of Vacuum Science & Technology A*, 22(4):1885–1891, 2004.

[14] TL Francis, Ö Mermer, G Veeraraghavan, and M Wohlgenannt. Large magnetoresistance at room temperature in semiconducting polymer sandwich devices. *New Journal of Physics*, 6(1):185, 2004.

[15] TD Nguyen, Y Sheng, M Wohlgenannt, and TD Anthopoulos. On the role of hydrogen in organic magnetoresistance: A study of c 60 devices. *Synthetic Metals*, 157(22):930–934, 2007.

[16] Jan Kalinowski, Massimo Cocchi, Dalia Virgili, Piergiulio Di Marco, and Valeria Fattori. Magnetic field effects on emission and current in Alq_3-based electroluminescent diodes. *Chemical Physics Letters*, 380(5):710–715, 2003.

[17] Sang-Yun Lee, Seo-Young Paik, Dane R McCamey, Justin Yu, Paul L Burn, John M Lupton, and Christoph Boehme. Tuning hyperfine fields in conjugated polymers for coherent organic spintronics. *Journal of the American Chemical Society*, 133(7):2019–2021, 2011.

[18] P. A. Bobbert, T. D. Nguyen, F. W. A. van Oost, B. Koopmans, and M. Wohlgenannt. Bipolaron mechanism for organic magnetoresistance. *Phys. Rev. Lett.*, 99(21):216801, 2007.

[19] VN Prigodin, JD Bergeson, DM Lincoln, and AJ Epstein. Anomalous room temperature magnetoresistance in organic semiconductors. *Synthetic Metals*, 156(9):757–761, 2006.

[20] H. Odaka, Y. Okimoto, T. Yamada, H. Okamoto, M. Kawasaki, and Y. Tokura. Control of magnetic-field effect on electroluminescence in alq(3)-based organic light emitting diodes. *Appl. Phys. Lett.*, 88(12):123501, 2006.

[21] Y. Iwasaki, T. Osasa, M. Asahi, M. Matsumura, Y. Sakaguchi, and T. Suzuki. Fractions of singlet and triplet excitons generated in organic light-emitting devices based on a polyphenylenevinylene derivative. *Phys. Rev. B*, 74(19):195209, 2006.

[22] Yue Wu, Zhihua Xu, Bin Hu, and Jane Howe. Tuning magnetoresistance and magnetic-field-dependent electroluminescence through mixing a strong-spin-orbital-coupling molecule and a weak-spin-orbital-coupling polymer. *Physical Review B*, 75(3):035214, 2007.

[23] J. D. Bergeson, V. N. Prigodin, D. M. Lincoln, and A. J. Epstein. Inversion of magnetoresistance in organic semiconductors. *Phys. Rev. Lett.*, 100(6):067201, 2008.

[24] JS Wilson, AS Dhoot, AJAB Seeley, MS Khan, A Köhler, and RH Friend. Spin-dependent exciton formation in π-conjugated compounds. *Nature*, 413(6858):828–831, 2001.

[25] Pratik Desai, P Shakya, T Kreouzis, WP Gillin, NA Morley, and MRJ Gibbs. Magnetoresistance and efficiency measurements of al q 3-based oleds. *Physical Review B*, 75(9):094423, 2007.

[26] Bin Hu and Yue Wu. Tuning magnetoresistance between positive and negative values in organic semiconductors. *Nature materials*, 6(12):985–991, 2007.

[27] C Zhang, D Sun, CX Sheng, YX Zhai, K Mielczarek, A Zakhidov, and ZV Vardeny. Magnetic field effects in hybrid perovskite devices. *Nature Physics*, 2015.

[28] Ayeleth H Devir-Wolfman, Bagrat Khachatryan, Bhoj R Gautam, Lior Tzabary, Amit Keren, Nir Tessler, Z Valy Vardeny, and Eitan Ehrenfreund. Short-lived charge-transfer excitons in organic photovoltaic cells studied by high-field magneto-photocurrent. *Nature communications*, 5:4529, January 2014.

[29] F. J. Wang, H. Bassler, and Z. V. Vardeny. Magnetic field effects in π-conjugated polymer-fullerene blends: Evidence for multiple components. *Phys. Rev. Lett.*, 101(23):236805, 2008.

[30] O. Mermer, G. Veeraraghavan, T. L. Francis, Y. Sheng, D. T. Nguyen, M. Wohlgenannt, A. Kohler, M. K. Al-Suti, and M. S. Khan. Large magnetoresistance in nonmagnetic π-conjugated semiconductor thin film devices. *Phys. Rev. B*, 72(20):205202, 2005.

[31] Chihaya Adachi, Marc A. Baldo, Mark E. Thompson, and Stephen R. Forrest. Nearly 100% internal phosphorescence efficiency in an organic light-emitting device. *Journal of Applied Physics*, 90(10):5048–5051, 2001.

[32] Ayataka Endo, Mai Ogasawara, Atsushi Takahashi, Daisuke Yokoyama, Yoshimine Kato, and Chihaya Adachi. Thermally activated delayed fluorescence from Sn^{4+}–Porphyrin complexes and their application to organic light emitting diodes — a novel mechanism for electroluminescence. *Advanced Materials*, 21(47):4802–4806, 2009.

[33] Ö Mermer, G Veeraraghavan, TL Francis, Y Sheng, DT Nguyen, M Wohlgenannt, A Köhler, MK Al-Suti, and MS Khan. Large magnetoresistance in nonmagnetic π-conjugated semiconductor thin film devices. *Physical Review B*, 72(20):205202, 2005.

[34] P Desai, P Shakya, T Kreouzis, and WP Gillin. Magnetoresistance in organic light-emitting diode structures under illumination. *Physical Review B*, 76(23):235202, 2007.

[35] Bin Hu and Yue Wu. Tuning magnetoresistance between positive and negative values in organic semiconductors. *Nature materials*, 6(12):985–991, 2007.

[36] Fujian Wang, Ferran Macia, Markus Wohlgenannt, Andrew D Kent, and Michael E Flatté. Magnetic fringe-field control of electronic transport in an organic film. *Physical Review X*, 2(2):021013, 2012.

[37] F. Maciá, F. Wang, N. J. Harmon, M. Wohlgenannt, A. D. Kent, and M. E. Flatté. Organic magnetoelectroluminescence for room temperature transduction between magnetic and optical information. *Nature Communications*, 5:3069, 2014.

[38] S. A. Crooker, F. Liu, M. R. Kelley, N. J. D. Martinez, W. Nie, A. Mohite, I. H. Nayyar, S. Tretiak, D. L. Smith, and P. P. Ruden. Spectrally resolved hyperfine interactions between polaron and nuclear spins in organic light emitting diodes: Magneto-electroluminescence studies. *Applied Physics Letters*, 105(15):153304, October 2014.

[39] J. Rybicki, R. Lin, F. Wang, M. Wohlgenannt, C. He, T. Sanders, and Y. Suzuki. Tuning the performance of organic spintronic devices using x-ray generated traps. *Phys. Rev. Lett.*, 109:076603, Aug 2012.

[40] U. Niedermeier, M. Vieth, R. Patzold, W. Sarfert, and H. von Seggern. Enhancement of organic magnetoresistance by electrical conditioning. *Applied Physics Letters*, 92(19):193309, 2008.

[41] G. Schmidt, D. Ferrand, L. W. Molenkamp, A. T. Filip, and B. J. van Wees. Fundamental obstacle for electrical spin injection from a ferromagnetic metal into a diffusive semiconductor. *Phys. Rev. B*, 62(8):R4790, 2000.

[42] S. A. Wolf, D. D. Awschalom, R. A. Buhrman, J. M. Daughton, S. von Molnar, M. L. Roukes, A. Y. Chtchelkanova, and D. M. Treger. Spintronics: A spin-based electronics vision for the future. *Science*, 294(5546):1488, 2001.

[43] D. D. Awschalom and M. E. Flatté. Challenges for semiconductor spintronics. *Nature Physics*, 3(3):153, 2007.

[44] J. Kalinowski, M. Cocchi, D. Virgili, P. Di Marco, and V. Fattori. Magnetic field effects on emission and current in Alq(3)-based electroluminescent diodes. *Chem. Phys. Lett.*, 380(5-6):710, 2003.

[45] T. L. Francis, O. Mermer, G. Veeraraghavan, and M. Wohlgenannt. Large magnetoresistance at room temperature in semiconducting polymer sandwich devices. *New Journal of Physics*, 6:185, 2004.

[46] V. N. Prigodin, J. D. Bergeson, D. M. Lincoln, and A. J. Epstein. Anomalous room temperature magnetoresistance in organic semiconductors. *Synth. Met.*, 156(9-10):757, 2006.

[47] B. Hu and Y. Wu. Tuning magnetoresistance between positive and negative values in organic semiconductors. *Nat. Mater.*, 6(12):985, 2007.

[48] F. L. Bloom, W. Wagemans, M. Kemerink, and B. Koopmans. Separating positive and negative magnetoresistance in organic semiconductor devices. *Phys. Rev. Lett.*, 99(25):257201, 2007.

[49] Yifei Wang, Kevser Sahin-Tiras, Nicholas J. Harmon, Markus Wohlgenannt, and Michael E. Flatté. Immense magnetic response of exciplex light emission due to correlated spin-charge dynamics. *Phys. Rev. X*, 6:011011, Feb 2016.

[50] T. D. Nguyen, Y. Sheng, M. Wohlgenannt, and T. D. Anthopoulos. On the role of hydrogen in organic magnetoresistance: A study of c-60 devices. *Synth. Met.*, 157(22-23):930, 2007.

[51] T. D. Nguyen, G. Hukic-Markosian, F. J. Wang, L. Wojcik, X. G. Li, E. Ehrenfreund, and Z. V. Vardeny. Isotope effect in spin response of pi-conjugated polymer films and devices. *Nat. Mater.*, 9(4):345, 2010.

[52] Yongzhou Ling, Yanlian Lei, Qiaoming Zhang, Lixiang Chen, Qunliang Song, and Zuhong Xiong. Large magneto-conductance and magneto-electroluminescence in exciplex-based organic light-emitting diodes at room temperature. *Applied Physics Letters*, 107(21), NOV 23 2015.

[53] Tek Basel, Dali Sun, Sangita Baniya, Ryan McLaughlin, Hyeonho Choi, Ohyun Kwon, and Z. Valy Vardeny. Magnetic Field Enhancement of Organic Light-Emitting Diodes Based on Electron Donor-Acceptor Exciplex. *Advanced Electronic Materials*, 2(2), FEB 2016.

[54] W. Wagemans, P. Janssen, A. J. Schellekens, F. L. Bloom, P. A. Bobbert, and B. Koopmans. The many faces of organic magnetoresistance. *Spin*, 01(01):93–108, 2011.

[55] V. Shrotriya, Y. Yao, G. Li, and Y. Yang. Effect of self-organization in polymer/fullerene bulk heterojunctions on solar cell performance. *Applied Physics Letters*, 89(6):3, 2006.

[56] P. Janssen, M. Cox, S. H. W. Wouters, M. Kemerink, M. M. Wienk, and B. Koopmans. Tuning organic magnetoresistance in polymer-fullerene blends by controlling spin reaction pathways. *Nature Communications*, 4, AUG 2013.

[57] Tho Duc Nguyen, Yugang Sheng, James Rybicki, Govindarajan Veeraraghavan, and Markus Wohlgenannt. Magnetoresistance in π-conjugated organic sandwich devices with varying hyperfine and spin–orbit coupling strengths, and varying dopant concentrations. *Journal of Materials Chemistry*, 17(19):1995–2001, 2007.

[58] K. Schulten and P. G. Wolynes. Semi-classical description of electron-spin motion in radicals including effect of electron hopping. *J. Chem. Phys.*, 68(7):3292, 1978.

[59] P. A. Bobbert, W. Wagemans, F. W. A. van Oost, B. Koopmans, and M. Wohlgenannt. Theory for spin diffusion in disordered organic semiconductors. *Phys. Rev. Lett.*, 102(15):156604, 2009.

[60] JS Wilson, AS Dhoot, AJAB Seeley, MS Khan, A Kohler, and RH Friend. Spin-dependent exciton formation in pi-conjugated compounds. *Nature*, 413(6858):828–831, OCT 25 2001.

[61] SP Kersten, AJ Schellekens, Bert Koopmans, and PA Bobbert. Magnetic-field dependence of the electroluminescence of organic light-emitting diodes: a competition between exciton formation and spin mixing. *Phys. Rev. Lett.*, 106(19):197402, 2011.

[62] Y. Sheng, T. D. Nguyen, G. Veeraraghavan, O. Mermer, M. Wohlgenannt, S. Qiu, and U. Scherf. Hyperfine interaction and magnetoresistance in organic semiconductors. *Phys. Rev. B*, 74(4):045213, 2006.

[63] Kevser Sahin-Tiras, Austin D Riedl, Markus Wohlgenannt, and James Rybicki. Identification of both bipolaron and electron-hole pair contributions to organic magnetoresistance in a regioregular polythiophene device. *Organic Electronics*, 2017.

[64] Gang Li, Vishal Shrotriya, Yan Yao, Jinsong Huang, and Yang Yang. Manipulating regioregular poly(3-hexylthiophene): [6,6]-phenyl-C-61-butyric acid methyl ester blends - route towards high efficiency polymer solar cells. *Journal of Materials Chemistry*, 17(30):3126–3140, 2007.

[65] H. Sirringhaus, P. J. Brown, R. H. Friend, M. M. Nielsen, K. Bechgaard, B. M. W. Langeveld-Voss, A. J. H. Spiering, R. A. J. Janssen, E. W. Meijer, P. Herwig, and D. M. de Leeuw. Two-dimensional charge transport in self-organized, high-mobility conjugated polymers. *Nature*, 401:685–688, 1999.

[66] JS Kim, M Granstrom, RH Friend, N Johansson, WR Salaneck, R Daik, WJ Feast, and F Cacialli. Indium-tin oxide treatments for single- and double-layer polymeric light-emitting diodes: The relation between the anode physical, chemical, and morphological properties and the device performance. *Journal of Applied Physics*, 84(12):6859–6870, DEC 15 1998.

[67] T. D. Nguyen, Y. Sheng, J. Rybicki, and M. Wohlgenannt. Magnetic field-effects in bipolar, almost hole-only and almost electron-only tris-(8-hydroxyquinoline) aluminum devices. *Phys. Rev. B*, 77(23):235209, 2008.

[68] T. D. Nguyen, B. R. Gautam, E. Ehrenfreund, and Z. V. Vardeny. Magnetoconductance Response in Unipolar and Bipolar Organic Diodes at Ultrasmall Fields. *Physical Review Letters*, 105(16), OCT 14 2010.

[69] A Salleo, TW Chen, AR Volkel, Y Wu, P Liu, BS Ong, and RA Street. Intrinsic hole mobility and trapping in a regioregular poly(thiophene). *Physical Review B*, 70(11), SEP 2004.

[70] C. Tanase, E. J. Meijer, P. W. M. Blom, and D. M. de Leeuw. Unification of the hole transport in polymeric field-effect transistors and light-emitting diodes. *Phys. Rev. Lett.*, 91:216601, Nov 2003.

[71] P. Desai, P. Shakya, T. Kreouzis, W. P. Gillin, N. A. Morley, and M. R. J. Gibbs. Magnetoresistance and efficiency measurements of alq(3)-based oleds. *Phys. Rev. B*, 75(9):094423, 2007.

[72] Martin A Green, Keith Emery, Yoshihiro Hishikawa, Wilhelm Warta, and Ewan D Dunlop. Solar cell efficiency tables (version 45). *Progress in photovoltaics: research and applications*, 23(1):1–9, 2015.

[73] Ivo Borriello, Giovanni Cantele, and Domenico Ninno. Ab initio investigation of hybrid organic-inorganic perovskites based on tin halides. *Physical Review B*, 77(23):235214, 2008.

[74] DB Mitzi, CA Feild, WTA Harrison, AM Guloy, et al. Conducting tin halides with a layered organic-based perovskite structure. *Nature*, 369(6480):467–469, 1994.

[75] Akihiro Kojima, Kenjiro Teshima, Yasuo Shirai, and Tsutomu Miyasaka. Organometal halide perovskites as visible-light sensitizers for photovoltaic cells. *Journal of the American Chemical Society*, 131(17):6050–6051, 2009.

[76] Jeong-Hyeok Im, Chang-Ryul Lee, Jin-Wook Lee, Sang-Won Park, and Nam-Gyu Park. 6.5% efficient perovskite quantum-dot-sensitized solar cell. *Nanoscale*, 3(10):4088–4093, 2011.

[77] Hui-Seon Kim, Chang-Ryul Lee, Jeong-Hyeok Im, Ki-Beom Lee, Thomas Moehl, Arianna Marchioro, Soo-Jin Moon, Robin Humphry-Baker, Jun-Ho Yum, Jacques E Moser, et al. Lead iodide perovskite sensitized all-solid-state submicron thin film mesoscopic solar cell with efficiency exceeding 9%. *Scientific reports*, 2:591, 2012.

[78] Michael M Lee, Joël Teuscher, Tsutomu Miyasaka, Takurou N Murakami, and Henry J Snaith. Efficient hybrid solar cells based on meso-superstructured organometal halide perovskites. *Science*, 338(6107):643–647, 2012.

[79] Seong Sik Shin, Eun Joo Yeom, Woon Seok Yang, Seyoon Hur, Min Gyu Kim, Jino Im, Jangwon Seo, Jun Hong Noh, and Sang Il Seok. Colloidally prepared la-doped basno3 electrodes for efficient, photostable perovskite solar cells. *Science*, 356(6334):167–171, 2017.

[80] Brian O'regan and Michael Grätzel. A low-cost, high-efficiency solar cell based on dye-sensitized colloidal tio 2 films. *nature*, 353(6346):737–740, 1991.

[81] Wei Chen, Yongzhen Wu, Jian Liu, Chuanjiang Qin, Xudong Yang, Ashraful Islam, Yi-Bing Cheng, and Liyuan Han. Hybrid interfacial layer leads to solid performance improvement of inverted perovskite solar cells. *Energy & Environmental Science*, 8(2):629–640, 2015.

[82] Kuo-Chin Wang, Jun-Yuan Jeng, Po-Shen Shen, Yu-Cheng Chang, Eric Wei-Guang Diau, Cheng-Hung Tsai, Tzu-Yang Chao, Hsu-Cheng Hsu, Pei-Ying Lin, Peter Chen, et al. P-type mesoscopic nickel oxide/organometallic perovskite heterojunction solar cells. *Scientific reports*, 4, 2014.

[83] Jin Hyuck Heo, Sang Hyuk Im, Jun Hong Noh, Tarak N Mandal, Choong-Sun Lim, Jeong Ah Chang, Yong Hui Lee, Hi-jung Kim, Arpita Sarkar, Md K Nazeeruddin, et al. Efficient inorganic-organic hybrid heterojunction solar cells containing perovskite compound and polymeric hole conductors. *Nature photonics*, 7(6):486–491, 2013.

[84] Joshua J Choi, Xiaohao Yang, Zachariah M Norman, Simon JL Billinge, and Jonathan S Owen. Structure of methylammonium lead iodide within mesoporous titanium dioxide: active material in high-performance perovskite solar cells. *Nano letters*, 14(1):127–133, 2013.

[85] Tomas Leijtens, Giles E Eperon, Sandeep Pathak, Antonio Abate, Michael M Lee, and Henry J Snaith. Overcoming ultraviolet light instability of sensitized tio2 with meso-superstructured organometal tri-halide perovskite solar cells. *Nature communications*, 4:2885, 2013.

[86] Tomas Leijtens, Beat Lauber, Giles E Eperon, Samuel D Stranks, and Henry J Snaith. The importance of perovskite pore filling in organometal mixed halide sensitized tio2-based solar cells. *The journal of physical chemistry letters*, 5(7):1096–1102, 2014.

[87] Giles E Eperon, Victor M Burlakov, Pablo Docampo, Alain Goriely, and Henry J Snaith. Morphological control for high performance, solution-processed planar heterojunction perovskite solar cells. *Advanced Functional Materials*, 24(1):151–157, 2014.

[88] Woon Seok Yang, Jun Hong Noh, Nam Joong Jeon, Young Chan Kim, Seungchan Ryu, Jangwon Seo, and Sang Il Seok. High-performance photovoltaic perovskite layers fabricated through intramolecular exchange. *Science*, 348(6240):1234–1237, 2015.

[89] Eran Edri, Saar Kirmayer, Alex Henning, Sabyasachi Mukhopadhyay, Konstantin Gartsman, Yossi Rosenwaks, Gary Hodes, and David Cahen. Why lead methylammonium tri-iodide perovskite-based solar cells require a mesoporous electron transporting scaffold (but not necessarily a hole conductor). *Nano letters*, 14(2):1000–1004, 2014.

[90] Huanping Zhou, Qi Chen, Gang Li, Song Luo, Tze-bing Song, Hsin-Sheng Duan, Ziruo Hong, Jingbi You, Yongsheng Liu, and Yang Yang. Interface engineering of highly efficient perovskite solar cells. *Science*, 345(6196):542–546, 2014.

[91] Qingfeng Dong, Yongbo Yuan, Yuchuan Shao, Yanjun Fang, Qi Wang, and Jinsong Huang. Abnormal crystal growth in ch 3 nh 3 pbi 3- x cl x using a multi-cycle solution coating process. *Energy & Environmental Science*, 8(8):2464–2470, 2015.

[92] Yani Chen, Bobo Li, Wei Huang, Deqing Gao, and Ziqi Liang. Efficient and reproducible ch 3 nh 3 pbi 3- x (scn) x perovskite based planar solar cells. *Chemical Communications*, 51(60):11997–11999, 2015.

[93] Jingbi You, Lei Meng, Tze-Bin Song, Tzung-Fang Guo, Wei-hsuan Chang, Ziruo Hong, Huajun Chen, Huanping Zhou, Qi Chen, Yongsheng Liu, et al. Improved air stability of perovskite solar cells via solution-processed metal oxide transport layers. *Nature nanotechnology*, 11(1):75, 2016.

[94] Jong Hoon Park, Jangwon Seo, Sangman Park, Seong Sik Shin, Young Chan Kim, Nam Joong Jeon, Hee-Won Shin, Tae Kyu Ahn, Jun Hong Noh, Sung Cheol Yoon, et al. Efficient ch3nh3pbi3 perovskite solar cells employing nanostructured p-type nio electrode formed by a pulsed laser deposition. *Advanced Materials*, 27(27):4013–4019, 2015.

[95] Julian Burschka, Norman Pellet, Soo-Jin Moon, Robin Humphry-Baker, Peng Gao, Mohammad K Nazeeruddin, and Michael Grätzel. Sequential deposition as a route to high-performance perovskite-sensitized solar cells. *Nature*, 499(7458):316, 2013.

[96] Jun Xi, Zhaoxin Wu, Hua Dong, Bin Xia, Fang Yuan, Bo Jiao, Lixin Xiao, Qihang Gong, and Xun Hou. Controlled thickness and morphology for highly efficient inverted planar heterojunction perovskite solar cells. *Nanoscale*, 7(24):10699–10707, 2015.

[97] Mingzhen Liu, Michael B Johnston, and Henry J Snaith. Efficient planar heterojunction perovskite solar cells by vapour deposition. *Nature*, 501(7467):395, 2013.

[98] Zhaoning Song, Suneth C Watthage, Adam B Phillips, Brandon L Tompkins, Randy J Ellingson, and Michael J Heben. Impact of processing temperature and composition on the formation of methylammonium lead iodide perovskites. *Chemistry of Materials*, 27(13):4612–4619, 2015.

[99] C Roldan-Carmona, P Gratia, I Zimmermann, G Grancini, P Gao, Michael Graetzel, and Mohammad Khaja Nazeeruddin. High efficiency methylammonium lead triiodide perovskite solar cells: the relevance of non-stoichiometric precursors. *Energy & Environmental Science*, 8(12):3550–3556, 2015.

[100] Qi Wang, Yuchuan Shao, Qingfeng Dong, Zhengguo Xiao, Yongbo Yuan, and Jinsong Huang. Large fill-factor bilayer iodine perovskite solar cells fabricated by a low-temperature solution-process. *Energy & Environmental Science*, 7(7):2359–2365, 2014.

[101] Jeong-Hyeok Im, In-Hyuk Jang, Norman Pellet, Michael Grätzel, and Nam-Gyu Park. Growth of ch3nh3pbi3 cuboids with controlled size for high-efficiency perovskite solar cells. *Nature nanotechnology*, 9(11):927–932, 2014.

[102] Nam Joong Jeon, Jun Hong Noh, Young Chan Kim, Woon Seok Yang, Seungchan Ryu, and Sang Il Seok. Solvent engineering for high-performance inorganic–organic hybrid perovskite solar cells. *Nature materials*, 13(9):897–903, 2014.

[103] Manda Xiao, Fuzhi Huang, Wenchao Huang, Yasmina Dkhissi, Ye Zhu, Joanne Etheridge, Angus Gray-Weale, Udo Bach, Yi-Bing Cheng, and Leone Spiccia. A fast deposition-crystallization procedure for highly efficient lead iodide perovskite thin-film solar cells. *Angewandte Chemie*, 126(37):10056–10061, 2014.

[104] Namyoung Ahn, Dae-Yong Son, In-Hyuk Jang, Seong Min Kang, Mansoo Choi, and Nam-Gyu Park. Highly reproducible perovskite solar cells with average efficiency of 18.3% and best efficiency of 19.7% fabricated via lewis base adduct of lead (ii) iodide. *Journal of the American Chemical Society*, 137(27):8696–8699, 2015.

[105] Kangning Liang, David B Mitzi, and Michael T Prikas. Synthesis and characterization of organic- inorganic perovskite thin films prepared using a versatile two-step dipping technique. *Chemistry of materials*, 10(1):403–411, 1998.

[106] Taiyang Zhang, Mengjin Yang, Yixin Zhao, and Kai Zhu. Controllable sequential deposition of planar ch3nh3pbi3 perovskite films via adjustable volume expansion. *Nano letters*, 15(6):3959–3963, 2015.

[107] Valeria Nicolosi, Manish Chhowalla, Mercouri G Kanatzidis, Michael S Strano, and Jonathan N Coleman. Liquid exfoliation of layered materials. *Science*, 340(6139):1226419, 2013.

[108] Qi Chen, Huanping Zhou, Ziruo Hong, Song Luo, Hsin-Sheng Duan, Hsin-Hua Wang, Yongsheng Liu, Gang Li, and Yang Yang. Planar heterojunction perovskite solar cells via vapor-assisted solution process. *Journal of the American Chemical Society*, 136(2):622–625, 2013.

[109] Feng Hao, Constantinos C Stoumpos, Zhao Liu, Robert PH Chang, and Mercouri G Kanatzidis. Controllable perovskite crystallization at a gas–solid interface for hole conductor-free solar cells with steady power conversion efficiency over 10%. *Journal of the American Chemical Society*, 136(46):16411–16419, 2014.

[110] David B Mitzi, MT Prikas, and K Chondroudis. Thin film deposition of organic-inorganic hybrid materials using a single source thermal ablation technique. *Chemistry of materials*, 11(3):542–544, 1999.

[111] Mohammad Mahdi Tavakoli, Leilei Gu, Yuan Gao, Claas Reckmeier, Jin He, Andrey L Rogach, Yan Yao, and Zhiyong Fan. Fabrication of efficient planar perovskite solar cells using a one-step chemical vapor deposition method. *Scientific reports*, 5, 2015.

[112] Chang-Wen Chen, Hao-Wei Kang, Sheng-Yi Hsiao, Po-Fan Yang, Kai-Ming Chiang, and Hao-Wu Lin. Efficient and uniform planar-type perovskite solar cells by simple sequential vacuum deposition. *Advanced Materials*, 26(38):6647–6652, 2014.

[113] Olga Malinkiewicz, Aswani Yella, Yong Hui Lee, Guillermo Mínguez Espallargas, Michael Graetzel, Mohammad K Nazeeruddin, and Henk J Bolink. Perovskite solar cells employing organic charge-transport layers. *Nature Photonics*, 8(2):128–132, 2014.

[114] Qianqian Lin, Ardalan Armin, Ravi Chandra Raju Nagiri, Paul L Burn, and Paul Meredith. Electro-optics of perovskite solar cells. *Nature Photonics*, 9(2):106–112, 2015.

[115] Dewei Zhao, Weijun Ke, Corey R Grice, Alexander J Cimaroli, Xinxuan Tan, Mengjin Yang, Robert W Collins, Hongmei Zhang, Kai Zhu, and Yanfa Yan. Annealing-free efficient vacuum-deposited planar perovskite solar cells with evaporated fullerenes as electron-selective layers. *Nano Energy*, 19:88–97, 2016.

[116] Samuel D Stranks and Henry J Snaith. Metal-halide perovskites for photovoltaic and light-emitting devices. *Nature nanotechnology*, 10(5):391–402, 2015.

[117] Teddy Salim, Shuangyong Sun, Yuichiro Abe, Anurag Krishna, Andrew C Grimsdale, and Yeng Ming Lam. Perovskite-based solar cells: impact of morphology and device architecture on device performance. *Journal of Materials Chemistry A*, 3(17):8943–8969, 2015.

[118] Yixin Zhao and Kai Zhu. Solution chemistry engineering toward high-efficiency perovskite solar cells. *The journal of physical chemistry letters*, 5(23):4175–4186, 2014.

[119] Keyou Yan, Mingzhu Long, Tiankai Zhang, Zhanhua Wei, Haining Chen, Shihe Yang, and Jianbin Xu. Hybrid halide perovskite solar cell precursors: colloidal chemistry and coordination engineering behind device processing for high efficiency. *Journal of the American Chemical Society*, 137(13):4460–4468, 2015.

[120] Wenzhe Li, Jiandong Fan, Jiangwei Li, Yaohua Mai, and Liduo Wang. Controllable grain morphology of perovskite absorber film by molecular self-assembly toward efficient solar cell exceeding 17%. *Journal of the American Chemical Society*, 137(32):10399–10405, 2015.

[121] Wanyi Nie, Hsinhan Tsai, Reza Asadpour, Jean-Christophe Blancon, Amanda J Neukirch, Gautam Gupta, Jared J Crochet, Manish Chhowalla, Sergei Tretiak, Muhammad A Alam, et al. High-efficiency solution-processed perovskite solar cells with millimeter-scale grains. *Science*, 347(6221):522–525, 2015.

[122] Hui-Seon Kim, Ivan Mora-Sero, Victoria Gonzalez-Pedro, Francisco Fabregat-Santiago, Emilio J Juarez-Perez, Nam-Gyu Park, and Juan Bisquert. Mechanism of carrier accumulation in perovskite thin-absorber solar cells. *Nature communications*, 4:2242, 2013.

[123] Ze Yu and Licheng Sun. Recent progress on hole-transporting materials for emerging organometal halide perovskite solar cells. *Advanced Energy Materials*, 5(12), 2015.

[124] Yuzhuan Xu, Lifeng Zhu, Jiangjian Shi, Songtao Lv, Xin Xu, Junyan Xiao, Juan Dong, Huijue Wu, Yanhong Luo, Dongmei Li, et al. Efficient hybrid mesoscopic solar cells with morphology-controlled ch3nh3pbi3-xcl x derived from two-step spin coating method. *ACS applied materials & interfaces*, 7(4):2242–2248, 2015.

[125] Zhengguo Xiao, Qingfeng Dong, Cheng Bi, Yuchuan Shao, Yongbo Yuan, and Jinsong Huang. Solvent annealing of perovskite-induced crystal growth for photovoltaic-device efficiency enhancement. *Advanced Materials*, 26(37):6503–6509, 2014.

[126] Sarah M Vorpahl, Samuel D Stranks, Hirokazu Nagaoka, Giles E Eperon, Mark E Ziffer, Henry J Snaith, David S Ginger, et al. Impact of microstructure on local carrier lifetime in perovskite solar cells. *Science*, page aaa5333, 2015.

[127] B Selin Tosun and Hugh W Hillhouse. Enhanced carrier lifetimes of pure iodide hybrid perovskite via vapor-equilibrated re-growth (verg). *The journal of physical chemistry letters*, 6(13):2503–2508, 2015.

[128] Dong Liu, Lili Wu, Chunxiu Li, Shengqiang Ren, Jingquan Zhang, Wei Li, and Lianghuan Feng. Controlling ch3nh3pbi3–x cl x film morphology with two-step annealing method for efficient hybrid perovskite solar cells. *ACS applied materials & interfaces*, 7(30):16330–16337, 2015.

[129] Amalie Dualeh, Nicolas Tétreault, Thomas Moehl, Peng Gao, Mohammad Khaja Nazeeruddin, and Michael Grätzel. Effect of annealing temperature on film morphology of organic–inorganic hybrid pervoskite solid-state solar cells. *Advanced Functional Materials*, 24(21):3250–3258, 2014.

[130] Lingling Zheng, Yingzhuang Ma, Saisai Chu, Shufeng Wang, Bo Qu, Lixin Xiao, Zhijian Chen, Qihuang Gong, Zhaoxin Wu, and Xun Hou. Improved light absorption and charge transport for perovskite solar cells with rough interfaces by sequential deposition. *Nanoscale*, 6(14):8171–8176, 2014.

[131] Xunshan Liu, Zhencai Cao, Hongli Huang, Xuxu Liu, Yingzi Tan, Huajie Chen, Yong Pei, and Songting Tan. Novel d–d–π-a organic dyes based on triphenylamine and indole-derivatives for high performance dye-sensitized solar cells. *Journal of Power Sources*, 248:400–406, 2014.

[132] Dae-Yong Son, Jeong-Hyeok Im, Hui-Seon Kim, and Nam-Gyu Park. 11% efficient perovskite solar cell based on zno nanorods: an effective charge collection system. *The Journal of Physical Chemistry C*, 118(30):16567–16573, 2014.

[133] Jiang Liu, Cheng Gao, Lizhu Luo, Qinyan Ye, Xulin He, Liangqi Ouyang, Xiaowei Guo, Daming Zhuang, Cheng Liao, Jun Mei, et al. Low-temperature, solution processed metal sulfide as an electron transport layer for efficient planar perovskite solar cells. *Journal of Materials Chemistry A*, 3(22):11750–11755, 2015.

[134] Ling Wang, Weifei Fu, Zhuowei Gu, Congcheng Fan, Xi Yang, Hanying Li, and Hongzheng Chen. Low temperature solution processed planar heterojunction perovskite solar cells with a cdse nanocrystal as an electron transport/extraction layer. *Journal of Materials Chemistry C*, 2(43):9087–9090, 2014.

[135] Jeffrey A Christians, Raymond CM Fung, and Prashant V Kamat. An inorganic hole conductor for organo-lead halide perovskite solar cells. improved hole conductivity with copper iodide. *Journal of the American Chemical Society*, 136(2):758–764, 2013.

[136] Juan Pablo Correa Baena, Ludmilla Steier, Wolfgang Tress, Michael Saliba, Stefanie Neutzner, Taisuke Matsui, Fabrizio Giordano, T Jesper Jacobsson, Ajay Ram Srimath Kandada, Shaik M Zakeeruddin, et al. Highly efficient planar perovskite solar cells through band alignment engineering. *Energy & Environmental Science*, 8(10):2928–2934, 2015.

[137] Weijun Ke, Guojia Fang, Qin Liu, Liangbin Xiong, Pingli Qin, Hong Tao, Jing Wang, Hongwei Lei, Borui Li, Jiawei Wan, et al. Low-temperature solution-processed tin oxide as an alternative electron transporting layer for efficient perovskite solar cells. *Journal of the American Chemical Society*, 137(21):6730–6733, 2015.

[138] Peng Qin, Soichiro Tanaka, Seigo Ito, Nicolas Tetreault, Kyohei Manabe, Hitoshi Nishino, Mohammad Khaja Nazeeruddin, and Michael Grätzel. Inorganic hole conductor-based lead halide perovskite solar cells with 12.4% conversion efficiency. *Nature communications*, 5:3834, 2014.

[139] Senyun Ye, Weihai Sun, Yunlong Li, Weibo Yan, Haitao Peng, Zuqiang Bian, Zhiwei Liu, and Chunhui Huang. Cuscn-based inverted planar perovskite solar cell with an average pce of 15.6%. *Nano letters*, 15(6):3723–3728, 2015.

[140] Po-Wei Liang, Chu-Chen Chueh, Spencer T Williams, and Alex K-Y Jen. Roles of fullerene-based interlayers in enhancing the performance of organometal perovskite thin-film solar cells. *Advanced Energy Materials*, 5(10), 2015.

[141] Xiaobao Xu, Zonghao Liu, Zhixiang Zuo, Meng Zhang, Zhixin Zhao, Yan Shen, Huanping Zhou, Qi Chen, Yang Yang, and Mingkui Wang. Hole selective nio contact for efficient perovskite solar cells with carbon electrode. *Nano letters*, 15(4):2402–2408, 2015.

[142] Hao Hu, Ka Kan Wong, Tom Kollek, Fabian Hanusch, Sebastian Polarz, Pablo Docampo, and Lukas Schmidt-Mende. Highly efficient reproducible perovskite solar cells prepared by low-temperature processing. *Molecules*, 21(4):542, 2016.

[143] Chien-Hung Chiang, Zong-Liang Tseng, and Chun-Guey Wu. Planar heterojunction perovskite/pc 71 bm solar cells with enhanced open-circuit voltage via a (2/1)-step spin-coating process. *Journal of Materials Chemistry A*, 2(38):15897–15903, 2014.

[144] Anyi Mei, Xiong Li, Linfeng Liu, Zhiliang Ku, Tongfa Liu, Yaoguang Rong, Mi Xu, Min Hu, Jiangzhao Chen, Ying Yang, et al. A hole-conductor–free, fully printable mesoscopic perovskite solar cell with high stability. *Science*, 345(6194):295–298, 2014.

[145] Tomas Leijtens, Giles E Eperon, Nakita K Noel, Severin N Habisreutinger, Annamaria Petrozza, and Henry J Snaith. Stability of metal halide perovskite solar cells. *Advanced Energy Materials*, 5(20), 2015.

[146] Jarvist M Frost, Keith T Butler, Federico Brivio, Christopher H Hendon, Mark Van Schilfgaarde, and Aron Walsh. Atomistic origins of high-performance in hybrid halide perovskite solar cells. *Nano letters*, 14(5):2584–2590, 2014.

[147] Severin N Habisreutinger, Tomas Leijtens, Giles E Eperon, Samuel D Stranks, Robin J Nicholas, and Henry J Snaith. Carbon nanotube/polymer composites as a highly stable hole collection layer in perovskite solar cells. *Nano letters*, 14(10):5561–5568, 2014.

[148] Zhaoning Song, Suneth C Watthage, Adam B Phillips, Geethika K Liyanage, Rajendra R Khanal, Brandon L Tompkins, Randy J Ellingson, and Michael J Heben. Investigation of degradation mechanisms of perovskite-based photovoltaic devices using laser beam induced current mapping. In *Proc. SPIE*, volume 9561, page 956107, 2015.

[149] Xiong Li, Manuel Tschumi, Hongwei Han, Saeed Salem Babkair, Raysah Ali Alzubaydi, Azhar Ahmad Ansari, Sami S Habib, Mohammad Khaja Nazeeruddin, Shaik M Zakeeruddin, and Michael Grätzel. Outdoor performance and stability under elevated temperatures and long-term light soaking of triple-layer mesoporous perovskite photovoltaics. *Energy Technology*, 3(6):551–555, 2015.

[150] Jun Hong Noh, Sang Hyuk Im, Jin Hyuck Heo, Tarak N Mandal, and Sang Il Seok. Chemical management for colorful, efficient, and stable inorganic–organic hybrid nanostructured solar cells. *Nano letters*, 13(4):1764–1769, 2013.

[151] Giles E Eperon, Samuel D Stranks, Christopher Menelaou, Michael B Johnston, Laura M Herz, and Henry J Snaith. Formamidinium lead trihalide: a broadly tunable perovskite for efficient planar heterojunction solar cells. *Energy & Environmental Science*, 7(3):982–988, 2014.

[152] Nam Joong Jeon, Jun Hong Noh, Woon Seok Yang, Young Chan Kim, Seungchan Ryu, Jangwon Seo, and Sang Il Seok. Compositional engineering of perovskite materials for high-performance solar cells. *Nature*, 517(7535):476, 2015.

[153] Henry J Snaith, Antonio Abate, James M Ball, Giles E Eperon, Tomas Leijtens, Nakita K Noel, Samuel D Stranks, Jacob Tse-Wei Wang, Konrad Wojciechowski, and Wei Zhang. Anomalous hysteresis in perovskite solar cells. *The journal of physical chemistry letters*, 5(9):1511–1515, 2014.

[154] EL Unger, ET Hoke, CD Bailie, WH Nguyen, AR Bowring, T Heumüller, MG Christoforo, and MD McGehee. Hysteresis and transient behavior in current–voltage measurements of hybrid-perovskite absorber solar cells. *Energy & Environmental Science*, 7(11):3690–3698, 2014.

[155] Jing Wei, Yicheng Zhao, Heng Li, Guobao Li, Jinlong Pan, Dongsheng Xu, Qing Zhao, and Dapeng Yu. Hysteresis analysis based on the ferroelectric effect in hybrid perovskite solar cells. *The journal of physical chemistry letters*, 5(21):3937–3945, 2014.

[156] Jarvist M Frost, Keith T Butler, and Aron Walsh. Molecular ferroelectric contributions to anomalous hysteresis in hybrid perovskite solar cells. *Apl Materials*, 2(8):081506, 2014.

[157] W Tress, N Marinova, T Moehl, SM Zakeeruddin, Mohammad Khaja Nazeeruddin, and M Grätzel. Understanding the rate-dependent j–v hysteresis, slow time component, and aging in ch 3 nh 3 pbi 3 perovskite solar cells: the role of a compensated electric field. *Energy & Environmental Science*, 8(3):995–1004, 2015.

[158] Christopher Eames, Jarvist M Frost, Piers RF Barnes, Brian C O?regan, Aron Walsh, and M Saiful Islam. Ionic transport in hybrid lead iodide perovskite solar cells. *Nature communications*, 6:7497, 2015.

[159] Jin Hyuck Heo, Hye Ji Han, Dasom Kim, Tae Kyu Ahn, and Sang Hyuk Im. Hysteresis-less inverted ch 3 nh 3 pbi 3 planar perovskite hybrid solar cells with 18.1% power conversion efficiency. *Energy & Environmental Science*, 8(5):1602–1608, 2015.

[160] Victor W Bergmann, Stefan AL Weber, F Javier Ramos, Mohammad Khaja Nazeeruddin, Michael Grätzel, Dan Li, Anna L Domanski, Ingo Lieberwirth, Shahzada Ahmad, and Rüdiger Berger. Real-space observation of unbalanced charge distribution inside a perovskite-sensitized solar cell. *Nature communications*, 5:5001, 2014.

[161] Bekele Hailegnaw, Saar Kirmayer, Eran Edri, Gary Hodes, and David Cahen. Rain on methylammonium lead iodide based perovskites: possible environmental effects of perovskite solar cells. *The journal of physical chemistry letters*, 6(9):1543–1547, 2015.

[162] Po-Yen Chen, Jifa Qi, Matthew T Klug, Xiangnan Dang, Paula T Hammond, and Angela M Belcher. Environmentally responsible fabrication of efficient perovskite solar cells from recycled car batteries. *Energy & Environmental Science*, 7(11):3659–3665, 2014.